Università degli Studi di Padova

Department of Industrial Engineering

Master Thesis in Aerospace Engineering

Design and development of a regenerative cooling for small liquid engines

Supervisor
Daniele Pavarin
Università di Padova

Co-supervisors
Ing.Phd. Francesco Barato
Ing. Marco Santi
Università di Padova

Master Candidate
Matteo Fagherazzi
n° 1153454

Academic year 2018/2019

"I have learned to use the word *Impossible* with the greatest caution"

Wernher Von Braun

Abstract

The current digital age is characterized by a widespread use of technology devices in which many services are provided by internet and satellite support. The miniaturization of electronic components, the discovery and use of new lightweight and resistant materials, combined with an increase in reliability of the whole system, have allowed access to the space more economically. This has led to a substantial growth in the number of small satellites modifying requirements, design and the development approach. As other, propulsion subsystems have followed this renewal and miniaturization process, highlighting new challenges in active control system and building process. Contextually with this, awareness of a "green philosophy" has spread in the choice of propellants in order to reduce hazards and risks for people and the environment.

This research work has developed fully in agreement with the previous context, focusing on the design and development of a regenerative cooling system for small swirl green bipropellant rocket engine. According to "green philosophy", the couple of propellants selected are hydrogen peroxide (HTP High Test Peroxide) and common diesel for motor vehicles. After a first phase of technical in-depth analysis, a mathematical model has been realized exploring different heat transfer equation. Subsequently a design process has followed and finally a test phase.

All work conducted in this thesis has carried out in fulfilment of the MSc degree in Aerospace Engineering from the Padova's University. Development and tests have done in Voltabarozzo facility with *Technology for innovation and propulsion (T4i)* team.

Sommario

L'attività di ricerca svolta ha avuto come obiettivo il dimensionamento e lo sviluppo di un sistema di raffreddamento rigenerativo per piccoli motori bipropellente a razzo. La scelta di focalizzarsi su motori di ridotte dimensioni è legata principalmente al trend osservato negli ultimi decenni. La miniaturizzazione dei componenti elettronici, la riduzione del fabbisogno energetico e l'impiego di materiali più leggeri e resistenti, hanno concesso di ridurre notevolmente dimensioni, masse e indirettamente i costi consentendo un maggiore e diffuso accesso allo spazio. Si è osservato inoltre un rinnovato interesse nell'impiego di propellenti "green" a ridotta tossicità e impatto ambientale. La ricerca svolta è stata sviluppata tenendo in considerazione le precedenti direzioni commerciali dando la possibilità di rispondere concretamente alle varie esigenze. La taglia propulsiva del motore, $400[N]$ in orbita, risulta essere mediamente adatta per l'*orbital manoeuvring* relativo alla classe dei mini satelliti.
L'attività di ricerca svolta è stata caratterizzata da una prima fase di approfondimento, seguita dalla realizzazione di un modello matematico predittivo del fenomeno di scambio termico. Si è passati quindi alla progettazione-verifica, rispettando i vincoli-requisiti posti ed infine alla realizzazione del prototipo con validazione del modello matematico sviluppato mediante una serie di test. La fase di, assemblaggio e test verrà condotta a Voltabarozzo con la supervisione e l'ausilio del personale di *Technology for innovation and propulsion (T4i)*.

La prima fase di ricerca e approfondimento è stata espletata mediante la lettura di documentazione scientifica tra cui paper inerenti e sezioni di testi di riferimento, alcuni consigliati altri individuati autonomamente.
La modellizzazione matematica, è stata sviluppata in ambiente MATLAB ®e la struttura dell'algoritmo emula i comuni software agli elementi finiti. Il codice proposto è di tipo monodimensionale e trascura i flussi di calore secondari (lungo la coordinata assiale). La modellazione della combustione e la definizione delle proprietà chimico-fisiche T_{cc}, γ, M_m, c_p, μ, λ...) dei gas di scarico, è stata ottenuta mediante il codice CEA NASA assumendo, per semplicità, la condizione operativa sia *frozen*. In ogni caso è bene precisare che l'algoritmo implementato in MATLAB ®ed interfacciato con il CEA, è predisposto per operare anche in condizioni di *equilibrium* qualora venga scelta tale opzione operativa. Per quanto concerne invece le proprietà del fluido refrigerante, queste sono state importate dal database di REFPROP ®NIST e da altri database disponibili online. La geometria dell'ugello è stata realizzata seguendo dei testi specifici e sia per il convergente sia per il divergente sono state previste due formulazioni. Per quanto riguarda il divergente, per piccoli rapporti di espansione è stata implementata una classica configurazione conica, mentre per rapporti di espansione superiori si è preferito impiegare il metodo di "RAO". Per il convergente invece è stata prevista

una geometria per i deflussi assiali (combustione e scarico assiale) ed una per i deflussi swirl (combustione a vortice). Entrambe le configurazioni sono accessibili mediante un'opportuna selezione nell'algoritmo. Il moto del gas nell'ugello è stato simulato con le relazioni della gasdinamica monodimensionale isoentropica assumendo che la forzante del moto sia l'area. Per quanto riguarda lo scambio di calore lungo la coordinata radiale, sono state implementate numerose equazioni empiriche, rispettando i vari campi di validità.
Poiché lo studio ha coinvolto un elevato numero di variabili sono state condotte anche delle analisi di sensibilità o scenari al fine di constatare l'influenza delle varie grandezze. Tutti i risultati sono disponibili nella sezione 2.5.
La fase seguente ha portato alla progettazione dell'ugello e dei vari componenti che consentono la sua operatività. Questo processo è il condensato di una serie di successive iterazioni tra le possibili soluzioni, coniugando requisiti-vincoli, fattibilità, semplicità e costo. In sostanza l'iter di progettazione è stato svolto nella sua pienezza permettendo di entrare in contatto con le varie problematiche che si presentano in questa fase e di risolverle concretamente.
Infine sono stati definiti i test, discutendo le varie configurazioni di misura. Particolare attenzione e stata posta nella descrizione delle procedure e degli accorgimenti necessari per effettuare le misure.
Sfortunatamente non è stato possibile terminare nei tempi previsti le varie misure. Nonostante ciò, nel capitolo conclusivo sono state esaustivamente descritte aspettative e risultati attesi, soffermandosi in particolar modo sulle discrepanze attese.

Nomenclature

α	Convective coefficient $[\frac{W}{m^2K}]$
A	Area $[m^2]$
ACS	Attitude Control System
AR	Aspect Ratio
β	Thermal expansion coefficient $[\frac{m}{mK}]$
$c^\star$	Propellant characteristic velocity $[m/s]$
CEA	Chemical Equilibrium and Application
COTS	Commercial Of The Shelves
c_p	Specific heat $[\frac{J}{kgK}]$
dx	Axial step in nozzle [m]
D_h	Hydraulic diameter [m]
E	Elasticity modulus [Pa]
ε	Expansion ratio
FEM	Finite Element Method
γ	Ratio of specific heat
g_0	9.81 $[m/s^2]$
H_2O_2	Hydrogen peroxide
HRM	Hybrid Rocket Motor
HTP	High Test Peroxide
I_ρ	Impulse density $[\frac{kg \cdot s}{m^3}]$
I_s	Specific impulse $[s]$

I_{s_v}	Specific impulse @ vacuum $[s]$
λ	Thermal conductibility $[\frac{W}{mK}]$
LH2	Liquid hydrogen
LOX	Liquid oxygen
LPRE	Liquid Propellant Rocket Engine
M	Mach number
M_m	Molecular mass $[kg/kmol]$
$\dot{m}$	Mass flow rate $[kg/s]$
μ	Dynamic viscosity [Pa s]
NASA	National Aeronautics and Space Administration
ν	Poisson's ratio
NIST	National Institute of Standards and Technology
o/f	Oxidant to fuel ratio
NTO	Dinitrogen tetraoxide
P	Pressure $[Pa]$
Pr	Prandtl number $[\frac{Cp \cdot \mu}{\lambda}]$
$\dot{Q}$	Heat transfer rate $[W]$
$\dot{q}$	Heat flux $[W/m^2]$
R	Universal gas constant 8314.510 $[\frac{J}{kmolK}]$
Re	Reynolds number $[\frac{\rho \cdot v \cdot D}{\mu}]$
ρ	Density $[kg/m^3]$
RP-1	Rocket propellant 1
SRM	Solid Rocket Motor
σ_{UTS}	Ultimate stress [Pa]

t_b	Total burn duration $[s]$
T	Temperature $[K]$
v	Fluid velocity $[m/s]$
w	Width [m].

Some subscript and apices used:

0	Total state
a	Adiabatic
b	Boiling
c	Convergent
cc	Combustion chamber
ch	Channel
col	Coolant domain
conv	Convective transfer
cond	Conductive transfer
e	Exit
f	Fuel
fin	Fin
g	Gas domain
in	Inlet
out	Outlet
ox	Oxidant
rad	Radiative transfer
t	Throat
W	Wall

Contents

Listing of figures

Listing of tables

1 Introduction

Why still chemical propulsion? Starting from the end of the Second World War, the access to space has become the key tool for the demonstration of the supremacy of skills, technology and ideas indirectly. The Cold War has seen an exceptional boost in development of space industry spending considerable financial resources. During this period great efforts have been made for developing suitable structures and subsystems. In particular, rocket propulsion has seen a progressive improvement in engine class passing from the German liquid-fuelled *A4* ,known as *V2*, to powerful NASA *F1* and finally to today's sophisticated and optimized engines. Although development was primarily warlike, mankind understood the potential of this technology, not only for scientific research, often misunderstood, but also to revolutionize life by improving it, like the wheel many centuries before. As all technologies, for promoting the spread, it has been necessary to upset the trend of previous years by means of a consistent spending review to reduce costs and production times defining substantially two types of approach: protoflight and prototype. Neglecting space research sector in which, due to high value of mission and technical equipment installed, is required an high number of test for qualifying all components and for ensuring high reliability, the trend is to move towards a protoflight approach. The idea is to simplify subsystems, if possible miniaturize the spacecraft and use off the shelves component COTS exploiting flight heritage and the flight qualification approach.

In this evolution process, other propulsion technologies have been developed and tested suc-

cessfully including the electric one and among all, this responds with fullness to the "green philosophy". Electric propulsion has deeply revolutionized the concept of space mission reducing propellent masses, but in the other hand, increasing the burn time, modifying requirements on attitude control systems ACS and the thrust profile. Unlike chemical propulsion, the energy source is independent from the propellant and its choice takes place differently [1]. For understanding key benefits of electric propulsion and why chemical one is still fundamental, it's necessary to introduce a simplified thrust equation obtained for adapted pressure conditions*:

$$F = \dot{m} \cdot v_e \tag{1.1}$$

where v_e is the exhaust gas speed. Thrust is a requirement and can be satisfied by high mass flow rate and low exhaust velocity or vice versa. In order to reduce the amount of propellant to be stowed, that means weight and costs, we are interested in reducing the mass flow rate so it's clear that only high exhaust velocity are admitted. It's important to point out that v_e depends essentially on the propulsion technology so once chosen, minimal adjustments are allowed. A useful parameter for comparing different propulsive technologies, in terms of discharge speed, is the specific impulse:

$$I_s = v_e/g0 \tag{1.2}$$

As we can read in literature, the range of I_s for chemical propulsion is in the hundreds, while the electric one is between hundreds and thousands of seconds, i.e. is able to develop higher discharge speed. From this point of view the last technology seems to be the optimal choice and chemical propulsion should be abandoned. However, as previously mentioned, for electric propulsion the energy doesn't come from the propellent but is provided by an electric source. The propellant is only an operative fluid. For understanding the field of use of this technology is important to introduce the relationship between the power of the jet emitted and the electric power required in input:

$$P_{el} = \frac{1/2\dot{m} \cdot v_e}{\eta_{int}} \tag{1.3}$$

*The previous simplification does not affect the validity of the result that will be highlighted, only makes it more immediate

where η_{int} is an internal conversion efficiency factor. Now, by substituting (1.2) and (1.1) into the last (1.3) we obtain:

$$P_{el} = \frac{1/2 \cdot F \cdot I_s \cdot g_0}{\eta_{int}} \tag{1.4}$$

Immediately it's possible to see that already with small level of thrust high electric power are required (order of many [kW]). In the follow figure is possible to understand the various fields of application of the technologies available today.

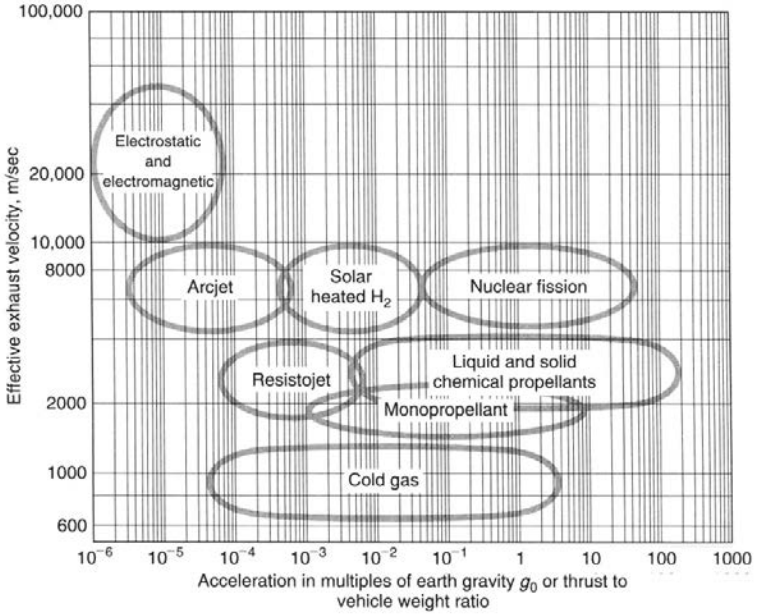

Figure 1.1: Exhaust velocities as a function of typical vehicle accelerations [1]

After this it's more clear why chemical propulsion remains and will still remain a fundamental technology to access space and in all those applications where high thrust authority is required, such as orbital maneuvers with tighter constraints on maneuver time.

1.1 Chemical rocket engine

The class of chemical rockets brings together different technologies, in particular solid rocket motor (SRM), liquid rocket engine (LPRE) and hybrid rocket motor (HRM) are included. The first to be developed was certainly the solid one due to its simplicity even if it presents some particular critical issues. Some written testimonies place the invention and the construction of the first solid propellant rockets around 970 AD by Feng Jishen, in what is now

China [8]. The first LPRE is placed in the twentieth century, in 1926, and is attributed to Robert Goddard. Finally, the last one was developed starting from 1933 and the first prototype is attributed to the Russian Mikhail Tikhonravov [9].
For understanding better why and where these technologies are used, it is necessary to briefly introduce merits and defects that characterize them.

1.1.1 Solid rocket motor

A SRM is characterized by the following parts depicted in the figure: As illustrated, the pro-

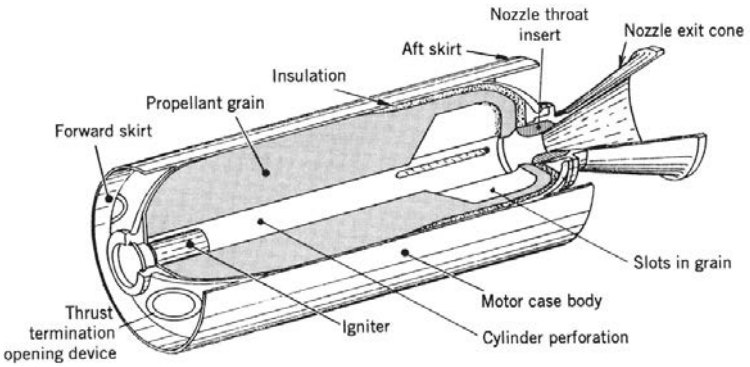

Figure 1.2: Simplified perspective three-quarter section of a typical solid propellant rocket motor [1]

pellant, called *grain*, is bonded to the case and the insulation layer. All the case is the combustion chamber so it's a pressure vessel that has to withstand the Pcc and naked parts, exposed to high thermal flux, have to be protected by an insulation layer or other thermal control techniques.
The ignition it's quite simple and occurs by the activation of the igniter which is essentially a gas generator. Once ignited, the SRM can't turned off, therefore there is only one shoot. This is one of the biggest drawbacks of this technology. Another big drawback is the reliability. SRMs are particularly sensitive to the quality of propellant grain because cracks or imperfections modify the burning area and therefore the pressure in the combustion chamber. If the pressure growth is excessive leads to the explosion. Only many checks and tests, during the whole production process, guarantee high reliability. Nevertheless SRMs are compact, with the highest I_ρ, self pressurizing and storable for years / decades. Generally SRMs aren't reusable except for the Space Shuttle Solid Rocket Booster (SRB) that are also the only man-

qualified SRMs. Nowadays commitment is mainly military even if in the past they have been widely used.

1.1.2 Liquid rocket motor

Despite their complexity, LPREs are today the most widespread motors because of their high performance and reliability. Many configurations have been studied and successfully implemented, each one with specific pro and cons. In this category both mono-propellant and bi-propellant are included. Due to high configuration numbers, it's not easy to generalize, however some components are always present: nozzle, combustion chamber with ignition, injection and cooling system, feed system, pressurization system and tanks. The main advantages of this technology are throttleability (inside a range), reusability, restrike, scalability, redundancy, they can be tested (also single components separately) and are suitable for manned system. In the other hand, as said before, they are very complex, require maintenance, pressurization system and propellant storability is limited in time. While a SRM is considered ready to fly, liquid rocket require specific procedures for flight preparation.
This technology is widely used for accessing space (sometimes supported by solid boosters), for orbital manoeuvring, landers, station keeping and ACS.

1.1.3 Hybrid rocket motor

This class of motors combines in a single solution solid and liquid technology. The therm *hybrid* refers to the phase of propellants, i.e. one is generally solid, the other liquid or gaseous (for saving volume and increasing I_ρ, liquid phase is preferred). Unlike SRMs propellants aren't premixed and the flame occurs exactly where oxidant and fuel meet. Even if there aren't limitation, the widespread configuration involves the fuel in solid phase while the oxidant in gaseous o liquid phase. Also for this class many configurations have been studied and built by mixing and inheriting solutions from both technologies. Even if the affinities are marked, the resulting engine is completely distinct and the combustion process is rather different from that of the SRM. The following figure is useful for understanding the scheme and a possible integration in a prototype. This technology offer appreciable benefits including throttleability, restrike, intrinsic safety (oxidant and fuel are separated) and allows to reduce cost respect a LPREs. In contrast, due to the complex combustion process that distinguish this motor, scalability and shape are strongly constrained.
Nevertheless these motors are suitable for small satellite to achieve orbit, for spatial tourism

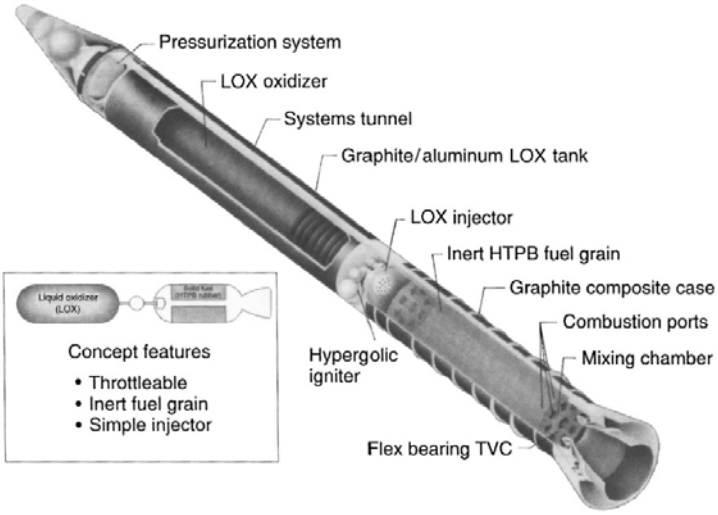

Figure 1.3: Large hybrid rocket booster concept [1]

and they are a good competitor for landers.

1.2 Cooling technologies

In chemical rockets, energy is stored in propellant/s and by means a combustion, a huge amount of chemical energy is turned into thermal. Finally, for obtaining thrust, these hot gasses are guided towards the nozzle through the chamber's geometry and expanded. Due to the high temperatures and gas velocity, internal surfaces are subject to intense thermal fluxes and for preventing the perforation of the engine wall, it is essential to implement a suitable thermal control.

It's important to point out that for both SRMs and HRMs, this intense thermal flux over the grain surfaces, is fundamental for maintaining the combustion process. The problem arise only on bare surfaces. Now, depending on the engine type, several cooling philosophies have been developed including: heat sink, ablative, radiative, film cooling and regenerative.

The first one is the simplest and exploits the fact that the thermal transient is slower than the fluid dynamics. For this reason it's suitable for small motor with high thermal capacity and for small t_b.

The second one is based on the sublimation layer of insulating material. The intense heat flux heats the superficial layer that in turn sublimates shielding the lower layers. This technology is widely used both in SRMs and HRMs.

Radiative cooling works on the thermal radiation. Due to the limits of this mechanism of heat transfer, it's used only with high temperatures where the process is more effective. It's widely used in orbit for LPRE, in the last section of the divergent where the heat fluxes are less severe. Generally it requires nozzle made up uf precious metals-alloys for withstanding high temperatures.
Film cooling is another technique for thermal control similar to the ablative. There are 2 configuration, in the first a fluid is drawn from the supply line and injected tangentially to the chamber's wall, in the second the fluid transpires from the porous wall. For both cases this film shields the wall and finally is ejected from the nozzle without takes part to the combustion process, i.e. the final I_s is just a bit lower. Also this technology is widely used with LPRE and often combined with radiative cooling.
Finally regenerative cooling, the more complicated and effective technology. The therm re-

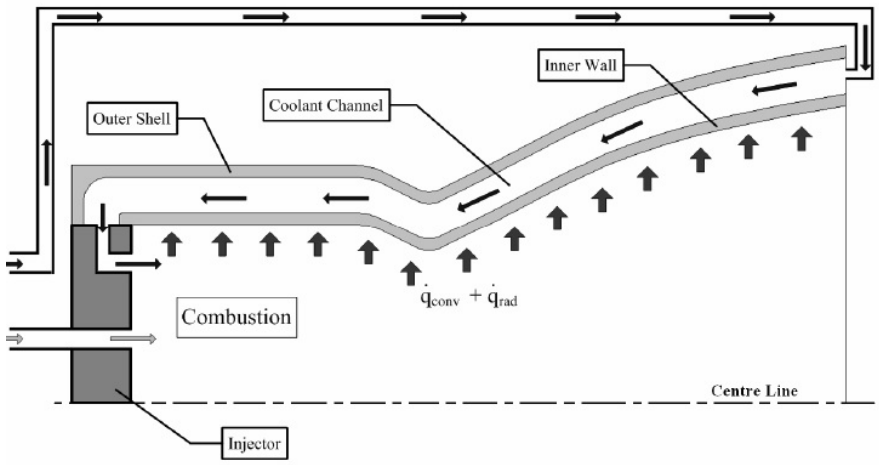

Figure 1.4: Cross-sectional view of a thrust chamber along axial direction with regenerative cooling [2]

generative means that one of propellants, before being injected in the combustion chamber where it will burn, flows through cooling passages. The relevant aspect that makes this technology attractive is that the heat absorbed by the propellant during cooling isn't wasted but increases its initial temperature. This raise in enthalpy allows to increase performance slightly, generally about 1% even if for small motor, in which the surface-to-volume ratio is higher and specific heat fluxes are stronger, is possible to reach more than 1% [1].

1.3 Propellants

1.3.1 Properties and choice of a propellant

In a chemical engine, the correct choice of propellants is fundamental for achieving great performance. It's important to point out that there isn't a single criterion of choice, it's the mission, with its requirements that suggest the best compromises each time. For example some typical main design drivers are material compatibility, admissible temperature range, I_ρ, toxicity, cost, storability and many other that depend specifically on the application (SRM,HRM,LPRE). As introduced before, it's fundamental know all propellant properties. The easiest information to obtain about chemical propellants are their physical and chemical properties. Fortunately all common propellant have been well studied and all data are available in many books and technical reviews.
From an engineering standpoint, the propellant selection involves an iteration process that satisfies all mission requirements and only at the end performance calculations are done [10].
To no surprise many propellants are hazardous and often toxic material able to explode. In particular *hydrazine* family is among the most toxic to breathe and handle and the chemical nature of propellant often requires particular technical measures both in storage and in use (pipes, tankage, gaskets).
Another well known property is the vapour pressure because gives both benefits and disadvantages. For liquid motors and hybrid too, an high vapour pressure allows a self pressurization of the tank but in the other hand can cause some combustion instabilities and cavitation in pumps. For solid motor an high vapour pressure brings to shrinking and cracking of the grain.
Also heat transfer properties are very important for all kind of motors and in particular way for all those in which there is regenerative cooling where, high specific heat are required.
Viscosity can be another relevant property even if principally for liquid or hybrid motors because affect pressure losses in feeding systems.
Density is relevant for all engines and has a significant influence on the size of the tanks.
About chemical reactivity, both propellants must be compatible during storage, especially for SRM as they are bonded togheter.
As regard *hypergolicity*, it's sometimes exploited for the ignition of the main engine, for driving turbines or for small motors.
Finally another important chemical parameter is the heat of formation that gives an idea of the final heat released in the combustion that depends on the difference of product and

reagent heat of formation.

1.3.2 Hydrogen Peroxide as a "green propellant"

According the introduction, it is noted that the trend of recent years is affirming the use of "green propellants" in order to reduce health and handling risks. The definition "green" is referred to the low toxicity of chemicals and exhaust gases compared to hydrazine, derivatives and similar compounds. Obviously the exhaust gases are however polluting substances, even if, much less dangerous. Actually not all green propellant are polluting, for example the couple LOX/LH2 or H2O2, used as monopropellant, produce only water steam as exhaust gas that is normally present in the atmosphere.
After an initial abandonment due to the complexity and reduced performance compared to other propellants, it is observed that the hydrogen peroxide is once again becoming an excellent candidate for space propulsion and many research centres are developing new prototypes. In particular, hydrogen peroxide is attractive because of its numerous advantages.

Advantages	Disadvantages
No toxic and non-carcinogenic	Careful handling required
Cheap, commercially available	Significant self-decomposition
Cold start capable (with catalyst)	Limited material compatibility
Low decomposition temperature	Low performance in monoprop mode
High Density	
Oxidizer in biprops and pure as monoprop	

Table 1.1: Pro and cons of hydrogen peroxide

To notice that a low decomposition temperature (depending on the grade but less than 1000°C), is particularly relevant especially when H2O2 is used in a gas generator for driving turbines because allows to use common metal alloy for the blades.

History and application

The discover of hydrogen peroxide dates back to 1818 to Louis Jacques Thenard. The first time he obtained this compound by reacting barium peroxide with nitric acid. He improved also the process, at first by adding hydrochloric acid ad later by the addition of some sulphuric acid to precipitate the by-product barium sulfate. Only after the 1894 pure hydrogen

peroxide was obtained by Richard Wolffenstein by means of vacuum distillation. During the twentieth century other processes have been developed and today it is possible to obtain different grade of H2O2, control the purity and the amount of stabilizers.
Initially the main use was only for bleaching but the first person to recognize its potentiality for rocket propulsion was Hellmuth Walter, who in 1935 set up his own company for the purpose at Kiel (Germany). His first application was the *Heinkel He 176*, a rocket-aircraft flown in 1938 [11]. Was a success but he understood some complications in igniting the mixture at low temperatures, so he developed a support ignitor with hydrazine hydrate and methanol that later was used in the *Walter 109-509* engine, mounted onboard of the *Komet-Messershmidt 163B*. During the Second World War other applications of this propellant were experimented in torpedoes, submarine and some derivatives in the most notable *V2*. After this success other nations were also interested in this new technology focusing also on different catalyst. Between the 50s and 70s the United Kingdom developed two launchers: *Black knight* and *Black Arrow*. The first one was a ballistic missile developed also for testing the design of the re-entry vehicle, the second was a satellite launcher. They used both different size of the same *Gamma*'s motor family and the couple of propellant was RP-1/HTP[12]. Both projects were abandoned due to excessive development and maintenance costs. As for USA, super-performance motors were studied and developed. Well known is the engine *LR-40* for the tragic accident in which, due to unexpected decomposition, two mechanics died. After this the program was abandoned. Approximately after 1985 all nations abandoned HTP in favour of more performing hydrazine, LOX and NTO. Only the last few decades have seen a consistent return on HTP and the major applications concern ACS, upper stage main propulsion, hypergolic and hybrid research.

Chemical and physical properties

Hydrogen peroxide is a chemical compound with the formula H_2O_2 and at room temperature and pressure it is liquid, transparent tending to blue and slightly more viscous than water. Its chemical structure is the follow in figure 1.5. Hydrogen peroxide is the simplest

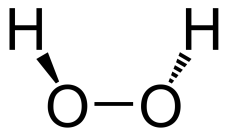

Figure 1.5: H_2O_2 Molecule

among peroxides and this family is characterize by the form $R-O-O-R$, where the group $O-O$ it's called peroxide group. In general, the oxygen oxidation state is (-2) even if some compounds have exceptions. Among these are the peroxides where the oxidation state is (-1), the superoxides $(-1/2)$, the ozonides $(-1/3)$ and the diflorides $(+2)$. This bond is rather unstable and the molecule tends to decompose. Light, pH and especially heat accelerate the process, so much that the rate of the decomposition reaction in homogeneous solution increases 2 to 3 times for every 10°C rise in temperature [13]. In it's pure form hydrogen peroxide presents this physical and chemical properties. As regard as boiling temperature,

$M\ [kg/kmol]$	$\rho\ [kg/m^3]$	Melting point [°C]	Boiling point [°C]
34.0147	1450	-0.43	150.2
μ @ 20°C $[cP]$	C_p (liquid) $[J/(kgK)]$	$\Delta HF^0_{298}[kJ/mol]$	
1.245	2619	-187.80	

Table 1.2: Chemical and physical properties

this has been evaluated at standard condition and by extrapolation at high concentrations due to explosion risks.

H_2O_2 (w/w) %	$\rho[kg/m^3]$	T [°C]
3	1009.5	15
27	1100	20
35	1130	20
50	1200	20
70	1290	20
75	1330	20
96	1420	20
98	1430	20
100	1450	20

Table 1.3: Density and H_2O_2 grade (concentration)[6]

Decomposition

The decomposition process transforms hydrogen peroxide is an exothermic reaction that turns H_2O_2 into water, oxygen and releases a considerable amount of heat. The reaction

is the follow.

$$2 \cdot H_2O_{2(l)} \rightarrow 2 \cdot H_2O_{(l)} + O_{2(g)} - 98.2kJ/mol \tag{1.5}$$

$$2 \cdot H_2O_{2(l)} \rightarrow 2 \cdot H_2O_{(g)} + O_{2(g)} - 54.2kJ/mol \tag{1.6}$$

The temperature of decomposition and the amount of oxygen released depends on the grade of hydrogen peroxide.

H_2O_2 (w/w)%	T_{adb} [°C]	Evaporated water %	Volume of products [l/kg]
10	89	0	44
20	100	12.1	276
30	100	27.9	542
40	100	45.5	808
50	100	65.5	1076
60	100	88.3	1347
70	233	100	1974
80	487	100	2893
85	613	100	3331
90	743	100	3761
95	867	100	4179
100	996	100	4592

Table 1.4: Characteristics of the decomposition [7]

Decomposition is strongly influenced by the presence of catalysts. Catalyst can be present in the aqueous solutions as a impurities or introduced voluntarily for boosting the process. Good catalyst are salts of metals such as iron, copper, chromium, vanadium, tungsten, molybdenum, silver and metals of the platinum group[13]. The most active decomposition catalysts are those giving ions, such as metal ions. To notice that the amount of impurities enough to start catalization is very low, about few parts per million.
Decomposition can be classified into homogeneous and heterogeneous. The first one refers to the case in which contaminants are dissolved in the aqueous phase , while the second one refers to the contact of insoluble solids with hydrogen peroxide. Good metal and metal oxides catalyst are: Ruthenium, Manganese, Iron, Cobalt, Nickel, Copper, Lead, Mercuric, Titanium, Platinum, Iridium, Palladium, Rhodium, Silver, Gold and many others.

Risks, handling and storage

As discussed before, it's clear that this oxidant at high concentration is very hazardous and this means that many precautions must be taken to avoid explosions. As regard the storage, long-term compatible materials must be chosen, generally plastics, glass and pure aluminium. Many precautions must be taken for the transport and handling too. The follow classification[7] is widely used in industrial field and in material datasheet, even if it is possible to find some different limitations on temperatures or contact duration.

- Class 1: materials that are fully compatible with hydrogen peroxide and suitable for long term contact such as storage tanks.
- Class 2: materials that are satisfactory for repeated short term contact with hydrogen peroxide prior to storage or use. Contact time should be quite short prior to storage. Contact time should not exceed four hours at 71°c or one week at 21°c prior to use.
- Class 3: materials that are suitable for short term contact only, prior to prompt use.
- Class 4: materials that are unsuitable or hazardous for any use with hydrogen peroxide.

Again to notice that compatibility may vary according to the concentration of hydrogen peroxide. For long term storage and to make the handling safer some stabilizer can be added. These stabilizer are able to absorb ions reducing the rate of decomposition. Some of these are phosphates, fluorides, cyanides, stannates, glues and proteins.

1.4 Structure of this dissertation

The present dissertation wants to investigate multiple aspects related to the development and realization of a bipropellant liquid rocket engine. The complete and whole design of a LPRE involves in-depth knowledge in different engineering fields such as chemistry, gas dynamic, heat transfer and thermodynamics, structures and materials. Many other have been neglected but in any case indispensable. In this work the nozzle and its regenerative thermal control will be analyzed, studying the different configurations until the final one that will be realized and tested.
The first (Chapter 1) will focus on the preliminary sizing of the nozzle according to requirements and constraints given by the client (supervisor and co-supervisors), material compatibility and the operating conditions during the test. After that, the heat exchange will be analyzed implementing a one-dimensional model, exploiting different empirical equations

found in literature and verifying their influences. Afterwards, starting from the results obtained, different channel geometries will be studied in order to evaluate which of these are more efficient in terms of temperature control and pressure losses. Particular attention will be reserved to the feasibility. The code will be implemented in MATLAB®.
After this mathematical modeling, an iterative process will begin for leading to the final prototype. The final nozzle will be the optimal compromise that will meet not only the previous requests but also all constraints that comes from all machining available. During this process particular attention will be reserved to costs, in order to develop a cheap motor that is in line with current trends and suitable for future application. See Chapter 2.All the cad drawings will be made with *SolidWorks*®.
The test phase, that will be discussed in chapter 3, will study the nozzle behaviour. The test matrix that will be followed is the subsequent.

- Cold static test for verifying hydraulic seals
- Cold test for evaluating true pressure losses in channels
- Hot test for evaluating the regenerative cooling system
- Thrust measurement

The aim is to compare all the data obtained from the tests with the mathematical model in order to validate it.
Finally in the last chapter (Conclusion) will be discussed the goals.

2

Mathematical model of heat transfer

2.1 Requirements and constraints

2.1.1 Problem definition

The first phase that all industrial design projects have in common is the in-depth analysis of the requirements and constraints placed by the customer and the working conditions. This is fundamental because allows you to identify quickly which design choices to undertake and which to discard, considerably reducing the time.
For this project the requirements imposed by the client are the follow:

1. Bipropellant rocket motor powered by HTP 90% grade and automotive diesel according to new "green propellant" space era.
2. Oxidant mass flow rate of about 120 [g/s].
3. Achieve a thrust in vacuum of about 400 [N].
4. Contraction ratio (chamber-to-throat) $A_c/A_t = 6$.
5. o/f=6.5.
6. Pcc=10 [bar].
7. Combustion chamber can work with axial and swirl flow too.
8. The nozzle design must be suitable for $3D$ metal printing.

9. The motor must operate for a long time and depending on orbital maneuvers, multiple ignition are planned.

In addiction it has been required the possibility to test the system on a test bench, located in Voltabarozzo, Padova (Italy), with the nozzle that operates in adapted condition.

2.1.2 Preliminary design considerations

From the previous section and collecting some requirements it is already possible to define approximatively the following design choices. In particular, from the last two requirements, it is deduced that for satisfying long burn times a cooling system is required and the possibility to print the motor case-nozzle by means of $3D$ metal printing, suggest the possibility to implement regenerative cooling without increasing considerably cost, having at the same time the highest propulsive efficiency. Considering the current oxidant-to-fuel ratio, hydrogen peroxide, as it will be the most abundant with an high specific heat, will be the coolant. The first requirement instead provides indications on the choice of materials. Finally, the others are useful for evaluating combustion temperature and nozzle geometry. There are no mass and/or envelope limits, in any case, willing to make a feasible flight model both will be kept content.

2.2 The working hypotheses

2.2.1 Hypotheses

This work has been developed tacking into account some hypotheses that have simplified the analysis. In any case, the work has been structured to allow easy future integration with more complex functions. The working hypotheses are the following.
First of all the code works in steady state with one-dimensional gasdynamics formulation and the nozzle is considered isentropic. The combustion process produces exhausts that are treated as frozen flow. In the heat transfer process secondary flows, or flows other than the radial one, are neglected because of their intensity. In addiction, all the energy transferred across the coolant wall is absorbed by the coolant, at each axial step the heat transfer coefficient along the coolant wall is constant, axial temperature gradients are ignored and the external jacket is considered adiabatic with the surrounding environment. Finally, about coolant properties, they are considered function of pressure and temperature.

2.2.2 The model flow chart

The mathematical model has been structured in different blocks or function. This philosophy has allowed to work easily and efficiently, enabling also quick changes by replacing the desired functions. All the code has been developed in MATLAB® using structured field for storing data. Below, in figure 2.1, is proposed a simplified version of the basic scheme used in the algorithm*. The model has been structured as follows.
First af all the algorithm translates the requirements and the pressure constraint, on the nozzle's exit section, in the nozzle geometry. This process has required to interface MATLAB® with CEA, an application developed by NASA able to calculate the properties of exhaust gases once the type of physical problem has been defined. After this the geometry is discretized in a mesh and the algorithm generates a library containing the coolant data as the temperature and pressure vary. This has been possible by picking data from *REFPROP* database, a NIST app and from other database available online. Subsequently it is implemented the routine for the calculation of the heat exchange. This is the core of the algorithm and it is divided into three levels. The inner one depicted in red, is an internal loop which verifies the convergence of the heat flux in a i-th section, imposed the various boundary conditions. Verified this, the algorithm evaluates all properties at the outlet section of the cooling channel which will become the entry conditions for the next section. This is done inside the green box. Finally the code verifies the compatibility of the material with stresses and temperature calculated at wall. Always inside the orange box, it is verified the equilibrium condition between the current temperature of the coolant leaving the channel and the last recorded. This allow to verify if an hotter coolant makes appreciable differences in combustion process.

2.3 CEA combustion model

CEA is a FORTRAN based app developed by NASA that calculates chemical equilibrium compositions and properties of complex mixtures. In the year CEA has seen subsequent improvements and today, in addition to being interfaced in C language, include calculation of theoretical rocket performance, Chapman-Jouguet detonation parameters, shock tube parameters, and combustion properties. Associated with the program there are independent databases with transport and thermodynamic properties of over 2000 species. Even if a simplified approach was possible taking into account only principal reactions, it has been decided to use the CEA program due to its reliability and robustness.

*A complete scheme would have required many more links and under-blocks precluding comprehension

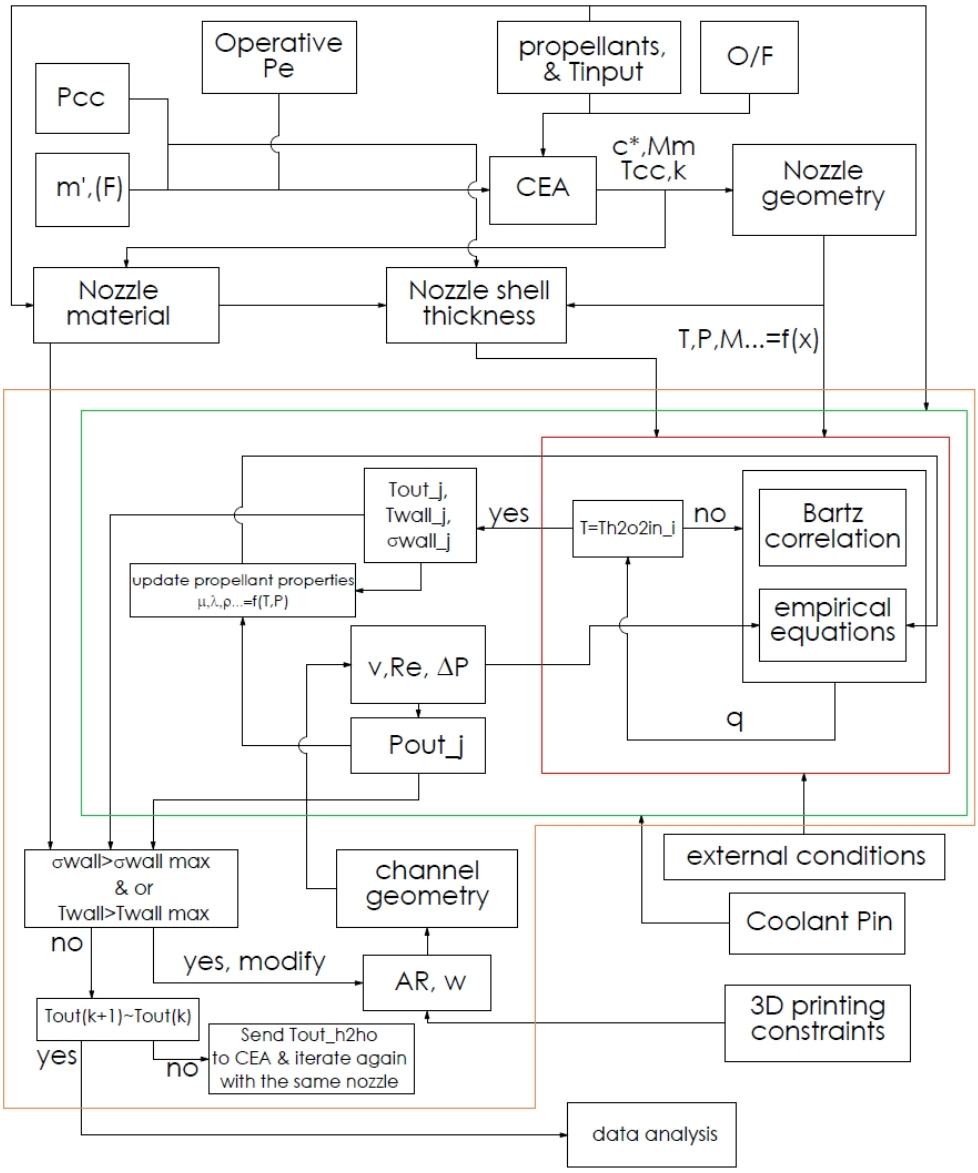

Figure 2.1: The simplified code flow chart

2.3.1 CEA Settings

For this project has been considered the built-in theoretical rocket performance app defined in the program with the abbreviation *rkt*. The rocket problem is treated in two different ways: Infinite Area Combustion *IAC* and Finite Area *FAC*. Both approach consider a one-dimensional flow with a inlet speed in combustion chamber that is approximatively zero, a

complete combustion process, adiabatic, isoentropic expansions, ideal gas formulation, no gradients in flow (that means homogeneous mix) and different phases don't afflict the motion of the gas. As regard the *IAC* model, it can treat the flow as frozen or in equilibrium, while in *FAC* only equilibrium condition is considered with no isoentropic combustion[14]. The first model, the infinite area combustion, require in input chamber pressure and to choose among frozen or equilibrium formulation with the specification, in case of frozen, the point beyond which the flow must be considered frozen. As regard the *FAC* instead, due to the equilibrium flow and the non isoentropic combustion, it is required an extra data for the convergence that can be the contraction ratio or the specific mass flow rate ($\dot{m}/A$). For both models there are also optional inputs, some of these for defining exit condition expressible with pressure ratio or area ratio, both for supersonic and subsonic case, and for accelerating convergence by modifying the initial combustion temperature guess.
Chosen the proper model in relation to the problem to be studied, the app require to specify the o/f and propellant/s. The o/f is defined in the main set up page, while propellants are specified in the following *Reactant* section. In this page all chemical data can be specified defining also unit of measurement for temperature, energy and whether to use as a reference mass or mole. Chemical compounds can be chosen from the database specifying if they are oxidant or fuel. In case the chemical searched is not available, it is possible to define it entirely by supplying all the necessary data. The following sections allow to exclude/include or insert certain compounds in the combustion process and in the last to define the outputs of the problem. Several outputs can be required such as thermodynamic properties, rocket performance parameters, transport parameters and many others. If desired, partial outputs obtained during the convergence process can also be requested.
The whole process, simplified by the graphic user interface, is finally summarized in a text input file which, if necessary, can be also modifiable.
In this work the chemical problem set up is the *IAC* and the initial temperature guess is the default one. According to working hypotheses the flow is treated as frozen and the chosen starting point is the combustor. Optional inputs are given for pressures and areas ratio in order to evaluate nozzle behaviour both in space and in the test facility. The pair of propellants chosen for this project are HTP with 90% grade and diesel for motor vehicles. After a search in the chemical database, they have been found H_2O_2 and *RP-1, Jet-A, JP-4, JP-5, JP-10*. From the guide provided with the program it is understood that the hydrogen peroxide is intended pure and the identified fuels, even if with similar composition, deviate from the diesel fuel[15]. For these reasons the two compounds have been inserted manually provid-

ing all the required data. Only coal $C_{(gr)}$ has been excluded from combustion. Finally, only a few thermodynamic outputs and all rocket performances and transport properties were selected. The requested number of outputs is higher than the actual needs, however, with the aim of generalizing the study for future additions, the algorithm in MATLAB® has also been prepared for the *FAC* model. The required outputs are as follows: pressure (P), temperature (T), density (ρ), molecular mass(M_m), specific heat(c_p), γ, mach number (M), area ratio ($\frac{A_e}{A_t}$), coefficient of thrust (C_f), I_s, I_{s_v}, μ, λ and Pr. Although the working conditions require an o/f ratio of 6.5, a further analysis has been carried out with the aim of verifying the properties of the exhaust gases according to the o/f. The first analysis investigated combustion for o/f ranging from 3 to 9 while the second the specific conditions of the problem. The input file generated for the first analysis is the follow:

```
problem    o/f=3,4,5,6,6.5,7,8,9,
rocket  frozen  nfz=1  tcest,k=3800
p,bar=10.000000,
pi/p=9.8692326671601,5000,
sup,ae/at=2.5,
react
fuel=diesel  wt=1.000000  t,k=290
h,j/mol=-303403.000000  C 12 H 23
oxid=HTP  wt=1.000000  t,k=290
h,j/mol=-203001.924400  H 2 O 1.8508
omit
C(gr)
output
 siunits transport
plot p t rho mw cp gam pip mach aeat cf ivac isp vis cond condfz
pran pranfz
end
```

while for the second analysis:

```
problem    o/f=6.5
rocket  frozen  nfz=1  tcest,k=3800
p,bar=10.000000,
pi/p=9.8692326671601,5000,
```

```
sup,ae/at=2.5,
react
fuel=diesel  wt=1.000000  t,k=290
h,j/mol=-303403.000000  C 12 H 23
oxid=HTP  wt=1.000000  t,k=290
h,j/mol=-203001.924400  H 2 O 1.8508
omit
C(gr)
output
     siunits transport
plot p t rho mw cp gam pip mach aeat cf ivac isp vis cond condfz
pran pranfz
end
```

In all the analyzes it was assumed to have both propellants at 17 [°C]. The expansions have been studied up to atmospheric pressure, to satisfy the test conditions, and up to 200 Pa for the operating case in orbit. The target value of expansion in orbit has been defined qualitatively with the sole purpose of understanding the trends of the quantities. The exact value of expansion to meet the required thrust requirement has been calculated later.

2.3.2 CEA Results

The execution of the program generates two files, the output file, with a complete report, and a matrix containing the main results of the analysis. Sensitivity analysis highlighted the following results depicted in figure 2.2 and 2.3.

The maximum combustion temperature is recorded near an o/f ratio equal to 7.1 while the molecular mass is always increasing with the variation of o/f. As far as exhaust gases are concerned, only the most abundant compounds have been traced and as can be seen from the figures 2.3, for high ratios of o/f, orientatively greater than 6.5, the quantity of water vapour and carbon dioxide stabilizes while for CO and H_2 is reduced. At high o/f ratios, the presence of an excess of O_2 and the increase of the $OH\cdot$ radical is observed. The $O\cdot$ and $HO_2\cdot$ radicals show a maximum at o/f 7, conditioning the chemical kinetics. From the analysis carried out it is possible to obtain the characteristic speed $c^\star$, a fundamental quantity to determine the theoretical performances of the motor. By virtue of the current working

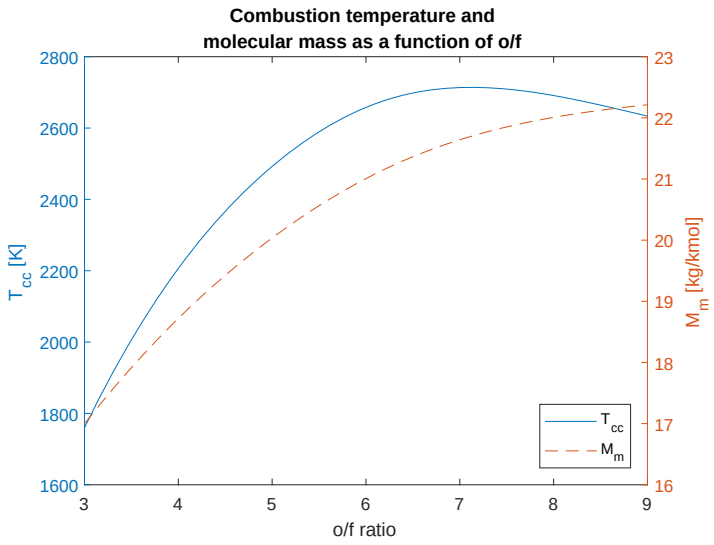

Figure 2.2: Temperature and molecular mass as a function of o/f

hypotheses, the characteristic velocity is defined by the following relation.

$$c^{\star} = \sqrt{\frac{\gamma R T_{cc}}{M_m}} \cdot \frac{\left[\frac{2}{\gamma+1}\right]^{\frac{-(\gamma+1)}{2(\gamma-1)}}}{\gamma} \tag{2.1}$$

Using the results of the analysis it is observed from figure 2.4 that the selected o/f ratio is close to the maximum value of the $c^{\star}$.

The results of the second analysis are summarized in the table 2.1. The exit 1 represents the discharge condition for the nozzle adapted to atmospheric pressure while the exit 2 represents the discharge condition in orbit. Again from table 2.1 it is possible to understand that the theoretical limit of this technology is around an I_{s_v} of 320s.

2.4 Mathematical model

The developed mathematical model has been structured in different sub-functions referred to in a general script called *Main*. In this script all the inputs and the sequence with which the various functions are to be called are defined. Besides the inputs specified in the 2.1.1 section, it is possible to choose different configurations by modifying the type of material, the geometric formulations and whether or not to enable specific correction models in the heat exchange.

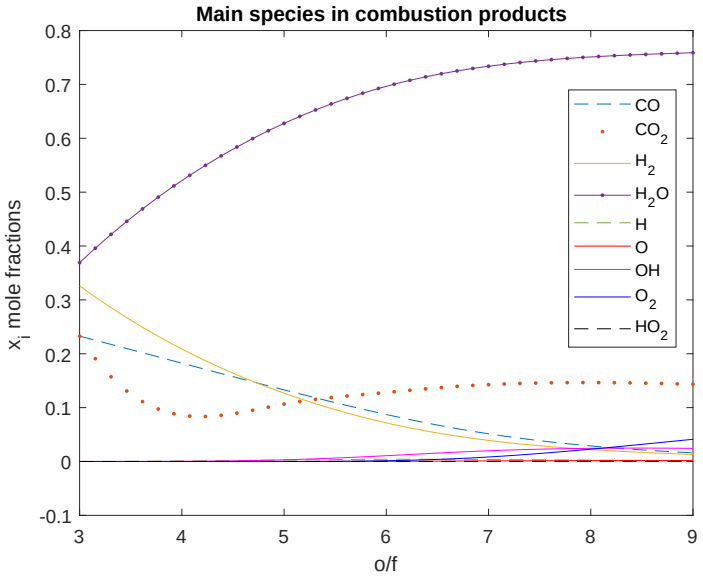

Figure 2.3: Exhausts composition

2.4.1 Geometry

The geometry of the nozzle has been obtained using the gasdynamics formulas applied to a chocked channel. Two cases have been implemented, one considering the exhaust gas at constant c_p and γ and the one in which they are variable. For convenience, the procedure of the first case will be reported, the one related to the second does not introduce particular complexity but requires interpolating the data supplied by the *CEA* and using the corresponding γ value in the various sections. The average γ value assumed is 1.19. To respect the adapted discharge condition the relationship between the pressures must be equal to:

$$\pi_e = P_{cc}/P_e \tag{2.2}$$

The Mach at the exit is:

$$M_e = \left[\frac{2}{\gamma - 1} \cdot \pi_e^{\frac{\gamma-1}{\gamma}-1}\right]^{0.5} \tag{2.3}$$

and the expansion ratio is given by the area rules:

$$\varepsilon = \frac{A_e}{A_t} = \frac{1}{M_e}\left[\frac{2(1 + \frac{\gamma-1}{2}M_e^2)}{\gamma + 1}\right]^{\frac{\gamma+1}{2(\gamma-1)}} \tag{2.4}$$

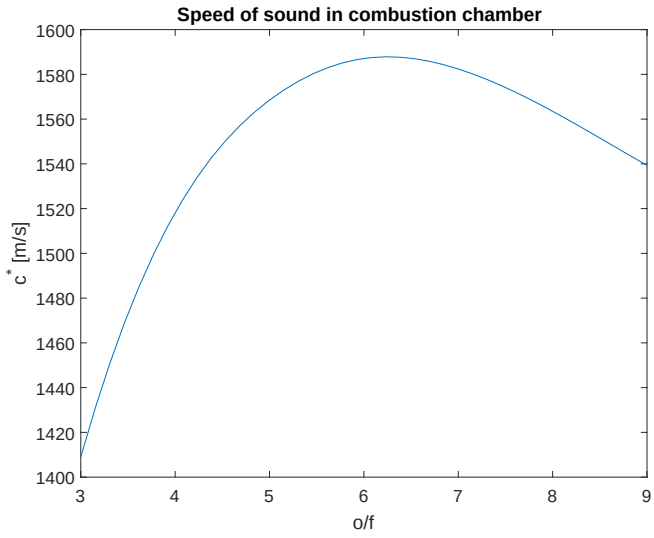

Figure 2.4: $c^\star$ in combustion chamber varying o/f ratio

The discharge coefficient is given by:

$$c_F = \sqrt{\frac{2\gamma^2}{\gamma-1}\frac{2}{\gamma+1}^{\frac{\gamma+1}{\gamma-1}}[1-\pi_e^{\frac{1-\gamma}{\gamma}}]} + \frac{P_e - P_{out}}{P_{cc}}\varepsilon \tag{2.5}$$

where P_{out} is equal to P_e (for the test case). Now, exhaust mass flow rate and thrust are tightly connected as the condition at the exit has been fixed.

$$F = \dot{m}_p c^\star c_F \tag{2.6}$$

$\dot{m}_p$ descends from *o/f* and $\dot{m}_{ox}$:

$$\dot{m}_p = \dot{m}_{ox}\left(1 + \frac{1}{\frac{o}{f}}\right) \tag{2.7}$$

Finally the throat area is:

$$A_t = \frac{F}{c_F P_{cc}} \tag{2.8}$$

and the specific impulse is the follow:

$$I_s = \frac{c^\star c_F}{g0} \tag{2.9}$$

	@ Chamber	@ Throat	@ Exit 1	@ Exit 2
T [K]	2698.45	2469.74	1868.23	547.90
M_m [kg/kmol]	21.365	21.365	21.365	21.365
c_p [J/KgK]	2513.3	2472.8	2324.1	1695.8
γ	1.1832	1.1868	1.2011	1.2978
M	/	1	2.149	5.835
μ [Pa s]	0.95879 1e-4	0.89755 1e-4	0.72472 1e-4	0.23767 1e-4
λ [W/mK]	3.2674 1e-1	2.9874 1e-1	2.2108 1e-1	0.4952 1e-1
A_e/A_t	/	1	2.2511	218.81
c_F	/	0.6729	1.2653	1.9340
I_{s_v} [s]	/	200.60	241.62	320
I_s [s]	/	108.87	204.72	312.92

Table 2.1: Combustion results

The quantities calculated and summarized in the following table 2.2 are to be intended as theoretical. No performance correction has been taken into account, i.e. $\eta = 1$.

π_e	M_e	ε	c_F	$c^\star$ [m/s]	F [N]	A_t $[mm^2]$	I_s [s]
9.8692	2.1553	2.2608	1.2663	1584.9	280	221.1244	204.5751

Table 2.2: Motor parameters

$\dot{m}_{ox}$ [kg/s]	$\dot{m}_f$ [kg/s]	$\dot{m}_p$ [kg/s]
0.1209	0.0186	0.1395

Table 2.3: Oxidant, fuel and exhaust mass flow rate

The nozzle contour has been calculated considering different formulations according to the type of combustion and to the constraint conditions imposed on the discharge pressure. The formulations implemented allow us to choose two different configurations for the divergent and two for the convergent. As for the divergent, the expected models are the conical divergent and the bell configuration calculated with the *RAO's* method which simplifies the application of the *MOC*(Method Of Characteristics)[1][†]. In particular, for small expansion ratios the conical configuration has been implemented with a usual $15\,°$ divergence half-angle,

[†]See chapter 3.4 for further information about RAO's method and for the fitting radii used

the complexity of the bell is not justified for small ratios. For the convergent, the configuration varies depending on the swirl or axial combustion. The contour equation for axial combustion is given by the Vitoshinsky formula[2]:

$$y = \frac{r_t}{\sqrt{1 - \frac{\left(1 - \frac{{r_t}^2}{r_c}\right)\left[1 - \frac{x}{1.5r_c}^2\right]^2}{\left[1 - \frac{1}{3}\frac{x}{1.5r_c}^2\right]^3}}} \tag{2.10}$$

where

$$r_t = \sqrt{\frac{A_t}{\pi}} \tag{2.11}$$

$$r_c = r_t\sqrt{\frac{A_c}{A_t}} \tag{2.12}$$

and x is the axial coordinate. For the swirl case the geometry used is given by two circumferential arcs connected each other. For now, in the literature there are no information on the most suitable shapes for this configuration even if many geometries have been studied. The angle α (see fig 2.5), that locates the tangency, is freely defined by the designer.

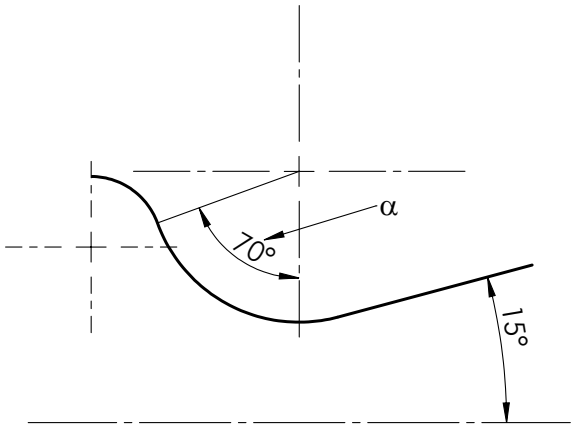

Figure 2.5: Nozzle for swirl combustion with conical divergent

The nozzle configuration used and tested is the follow showed in figure 2.6.
As it can be see in the figure 2.6, the contour is defined by three curves. For the convergent

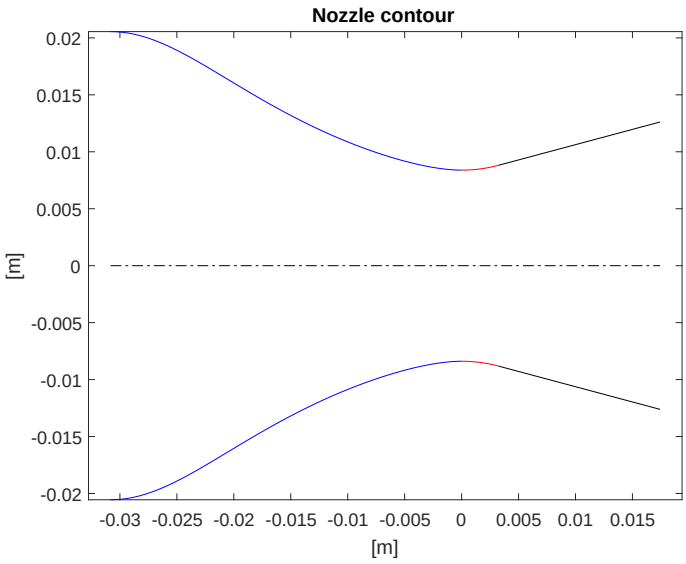

Figure 2.6: Nozzle contour

has been used the equation 2.10, for the divergent a straight line with a 15 ° slope and the two curves have been connected at the throat with a circumference arc having a radius of $1.5R_t$.

2.4.2 Coolant properties

In this model the treatment of the coolant has been the most general possible, considering it as a real fluid in which all properties vary with pressure and temperature. In particular, two different modeling philosophies have been studied to satisfy fundamental safety requirements during the test phase. The reason that has determined the need to create two models is strongly related to the properties of hydrogen peroxide and to its predisposition to decompose with increasing temperature and in hotspots correspondence. Since the analysis model has been studied with empirical equations, accepting a certain degree of uncertainty, to reduce the risk of explosion during the experimental phase the coolant has been replaced with water. In light of the above, the first modeling has been developed assuming to use as hydrogen peroxide water representing the real case of operation, while the second used water. For this project, the temperature and pressure range of interest has been set between 0-150 [°C] for temperatures and between 10-30 [bar] for pressures.
In the first modeling philosophy, the hydrogen peroxide has been treated as a pure fluid

whose properties have been referred to the desired concentration. This has been made possible by using a series of graphs provided by USP technologies[16] and data obtained by NASA[17]from which a database has been subsequently created in MATLAB ®. The creation of the database has required sampling of the curves provided by USP technologies and, where the data were not available, the introduction of the following models described in the NASA technical report[17].

$$\frac{c_p(T)}{R} = \sum_{i=1}^{r} a_i T^{q_i} \qquad r = 5, q_i = 0, 1, 2, 3, 4 \tag{2.13}$$

$$\begin{matrix} ln(\mu) \\ ln(\lambda) \end{matrix} = Aln(T) + \frac{B}{T} + \frac{C}{T^2} + D \tag{2.14}$$

All the coefficients are given in the same report previously mentioned[‡]. For boiling pressure and temperature has been used the follow equation[18]:

$$ln(P_b) = c_1 - \frac{c_2}{T} - \frac{c_3}{T^2} \tag{2.15}$$

Outside the validity range of the previous equations, the calculation of properties at the desired temperature and pressure range has been carried out by interpolation of the database data with splines subsequently evaluated at the desired points.
In the second modeling instead, MATLAB ® has been interfaced with *REFPROP* importing its database for the water compound. Also in this case the identification of the physical and transport properties has been achieved through linear interpolations. The direct use of *REFPROP* to determine the properties of the hydrogen peroxide at the desired concentration has not been possible because only water is currently available in the database. For both models the calculation of the properties has been carried out following the procedures described above using a specific function block which allows to obtain: ρ, μ, λ, c_p and T_b.
A preliminary sensitivity analysis conducted within the field of interest, modifying independently pressure and temperature, highlighted the following trends for previous physical and transport quantities. Once the temperature has been set, considerable increases in pressure result in a marked increase in the boiling temperature, slight increases in density, conductivity and slight reductions in specific heat and viscosity. While the pressure is set, considerable increases in temperature lead to substantial reductions in density, viscosity and equally con-

[‡]see pp.37 for specific heat and pp.86 for transport properties

siderable increases in specific heat and thermal conductivity. Therefore, it can be said that, except for the boiling temperature, the dependence with the pressure is negligible compared to that with the temperature which is orientatively greater than an order of magnitude.
It is important to note that the accuracy of the data used strongly depends on the modalities with which they have been obtained and there is no complete uniformity between the various agencies/suppliers. Moreover, especially for the first model, since there has no been continuity of data within the required temperature and pressure range, it has been necessary to interpolate data provided by different agencies and this could influence the results. The second model, on the other hand, is completely described by the *REFPORP* database, thus guaranteeing greater uniformity and greater reliability.

2.4.3 Mesh and Channels geometry

Mesh

The mesh used in this algorithm is particularly simple as it is one-dimensional. There are different ways in which it is possible to discretize the geometry, among these the most common are the homogeneous one and the one or two bias ones. In this case, considering the simplicity of the geometry and the rapidity of execution of the algorithm, a homogeneous discretization has been used which divided the geometry into 200 elements. This number represents a good compromise between speed and accuracy of the solution, ensuring an element size of about a quarter of a millimeter, substantially an order of magnitude lower than the characteristic unit of measurement of the model, the centimeter. It is worth noting that in the declaration of hypotheses, in section 2.2.1, secondary heat fluxes due to axial temperature gradients have been neglected. The choice of having a high number of elements allows to reduce the temperature gradient between two successive elements allowing to neglect this secondary flux. In any case, the number of elements can be modified by the user.
Other types of mesh, especially for large models, allow to increase the number of elements at the most stressed point (throat) and to reduce them towards the divergent and convergent ends, accelerating convergence and especially reducing computational resources.

Channels

Let's move on to the geometry of the channels. In the literature it's possible to observe channels with numerous geometric configurations, highlighting that the regenerative cooling has long been strongly studied with a theoretical approach combined with the experimental val-

idation due to the complexity and number of physical phenomena involved.
The first prototypes consisted of tubular channels. The nozzle was a natural evolution of tube bundle exchangers in which the suitably deformed and brazed pipes were joined to form the nozzle contour.

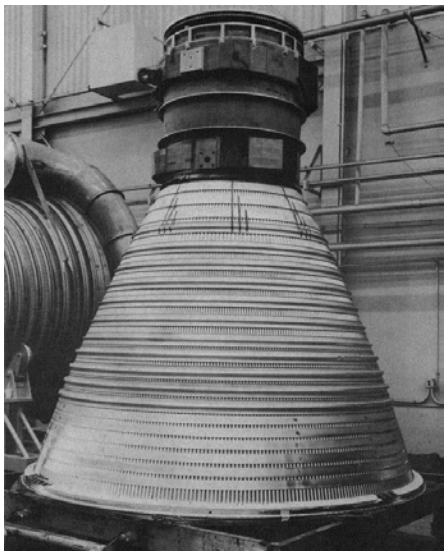

Figure 2.7: *F1* thrust chamber with tubular channels for regenerative cooling system (by heroicrelics.org)

The evolution of mechanical processing and materials has gradually made it possible to improve the cooling techniques, moving from circular-elliptical sections to more and more complex geometries. In particular, the construction of the regenerative nozzle has changed radically following a sequence of operations that first leads to the construction of the liner, then to the excavation of the channel, follows the mechanical junction with the external jacket and finally the installation of the manifold. Of all the operations, the most challenging is the closeout. Some processes typically used for the realization of the channels are end milling, water jet milling and electroerosion. For closeout operations instead, there are pressure assisted braze, standard pressure braze, electroplating, vacuum plasma spray, explosive bonding, laser welding and diffusion bonding[3]. The experimental use of 3D metal printing could introduce considerable revolutionary advantages over the entire process and condensing all the processing steps into one. For now, the main disadvantage is the size limitation. In the figure 2.8 it is possible to see some channels obtained by water jet milling and in 2.9 liner and external jacket bonded together.

(a) Dovetail channel (b) High Aspect Ratio channel

Figure 2.8: Channel machined with water jet milling[3]

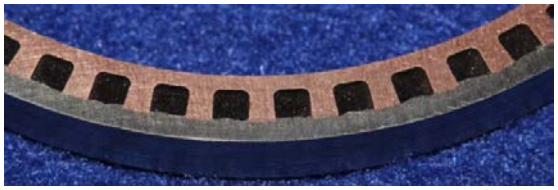

Figure 2.9: Bimetallic closeout[3]

From the literature it is observed that the rectangular section configuration is the most widespread because it results to be the best compromise between effectiveness and cost of realization.
As regards the laying of the channel, it is observed that the arrangement on the nozzle wall is mainly axial even if motors with spiral-arranged channels have been studied. In addition, in some engines, including the *F1*, bifurcation has been also used, in order to divide the channel flow and modify the transport properties.
In this work the geometry of the channel is rectangular, in line with the most widespread technology. The channel geometry has been described by two parameters: the aspect ratio (AR) and the width of the channel (w). Both sizes vary according to the axial coordinate in order to guarantee maximum freedom. This description has been implemented by subdividing the nozzle into n sections, for each of which the AR and w were specified. Subsequently, by means of spline interpolation, the AR and w have been calculated at each desired point. As for the wall thicknesses, these were calculated using pressure vessel relationships. The liner wall has been calculated with the following relation:

$$t_{cs} = \frac{P_{MEOP} r_{max}}{\sigma_{UTS}} = \frac{P_{cc} r_{max} \eta_P}{\sigma_{UTS}} \tag{2.16}$$

where P_{MEOP} is the *maximum expected operating pressure*, σ_{UTS} is the ultimate tensile stress of the case material at max allowed operating temperature and r_{max} is the case maximum

radius. To note that the radius of the case is variable with the axial coordinate, so it would be possible to optimize the mass by defining a variable t_{cs}, however, considering the size of the nozzle this makes no sense. Generally, for small motor $\eta_P = 2[10]$. As regard channels wall has been used an equation for pressurized pipe line supported by UNI 1285 en ISO 7088.

$$t_{pipe} = \left(\frac{Pd_{ext}}{20\sigma_{UTS} + P} + c\right)\frac{100}{100 - tol_{\%}} \tag{2.17}$$

In this equation P is the difference between operating pressure and external pressure, d_{ext} is the external diameter of the pipe, c is an overthickness, in this case assumed 0, and $tol_{\%}$ is a dimensional tolerance due to the production process, cautiously equal to 5%. Finally as regard the external jacket, t_{jck} has been taken the same value for t_{cs}.

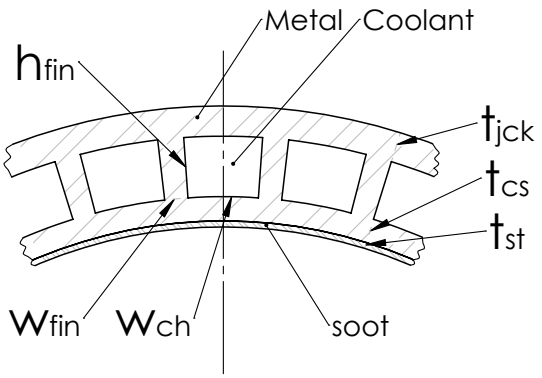

Figure 2.10: Simplified drawing of the canal section

Many materials have been considered including AISI 630 stainless steel and 718 inconel.The following results were obtained for these materials considering that $r_{max} = 20.55\,[\text{mm}]$. To

Material	σ_{UTS} [MPa]	$\sigma_{UTS@T}$ [MPa]	D_h [mm]	t_{cs} [mm]	t_{pipe} [mm]
AISI 630	1170	860	0.7384	0.0478	0.498
Inconel 718	965	758	0.7384	0.0542	0.603

Table 2.4: Estimates of liner and channel's walls thicknesses

note that for t_{pipe} has been considered the worst case in which the hydraulic diameter is max-

imum as well as the pressure difference between the operative and the external one[§]. The purpose of the equation 2.17 is only to provide an indicative value for the thicknesses, in a second moment the structure will be analyzed in detail. From the table 2.4 it is observed that the thickness of the liner sufficient to support the working pressure is on the order of hundredths of a millimeter. Since the tolerances in the realization with the $3D$ printing have to be taken into consideration, it has been decided to fix the value of t_{cs} and consequently t_{jck} to 0.5 [mm].
For controlling all the designing process in the MATLAB® , checks have been added to verify that the dimensional limits allowed by $3D$ metal printing are not exceeded and the average amplitude of the fin has been calculated with the following function once the number of channels has been set.

$$w_{fin} = \frac{2\pi r(x)}{n^{\circ}_{ch}} - w_{ch} \tag{2.18}$$

where *r* is the radius and x the axial coordinate. Finally, all the geometric properties of the channel are monitored by means of a graph (figure 2.11) and the simplified section is displayed at the corresponding axial coordinate (figure 2.12). In the current project the number of channel has been set to 37.

Let's move on to the preliminary evaluation of stress on the walls of the canals. From a structural point of view, circular-section tubular channels are preferred, not only for the simplicity of construction but also because they are subject to less stress. The stress analysis of the tubes is based upon three primary considerations: the hoop stress caused by coolant pressure, the thermal stress caused by temperature gradient across the tube section and the wall, and the bending stress caused by distortion induced by the pressure differential between adjacent tubes (if any) or by other effects such as discontinuities[19].

$$\sigma_{ch} = \frac{(P_{cc} - P_{col})0.5D_h}{t_{pipe}} + \frac{E\beta\dot{Q}t_{pipe}}{2(1-\nu)\lambda} + \frac{6M_A}{t^2_{pipe}} \tag{2.19}$$

To note that for this equation all dimensions must be referenced in the imperial measurement system. In this equation D_h is the hydraulic diameter of the channel, E and ν are the elasticity modulus and Poisson's ratio of tube wall, β is the thermal expansion, $\dot{Q}$ the heat rate and the M_A is the bending moment caused by pressure discontinuity between adjacent tube. Although the 2.19 relation has been obtained for circular tubes, it allows to identify

[§]The difference in pressure is minimal between two adjacent channels, intermediate with the combustion chamber and maximum with the external environment

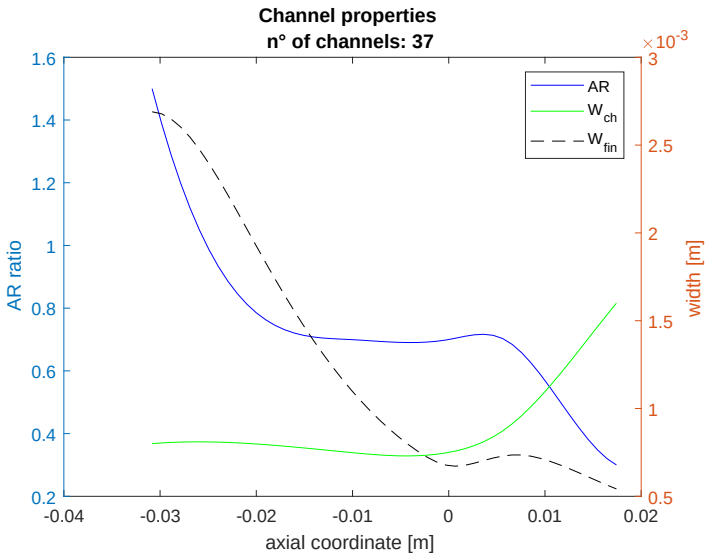

Figure 2.11: AR, w_{ch} and w_{fin} values depending on the axial coordinate

an order of magnitude that is still useful. In the polygonal sections, the presence of the edge concentrates tensions that are not present in the circular sections, for this reason the value obtained can not be taken as a reference but used only as an indicator. For the current project the previous relation can be further simplified by eliminating the term M_A because all the channels are single-pass and direct from the divergent towards the convergent, so there are no discontinuities in the pressures between adjacent channels.
The role of the outer jacket is fundamental under several aspects. In addition to determining the closure of the channel, it allows to absorb part of the stresses and to give greater rigidity to the structure. There are also other equations useful for predicting stress on the liner wall. In particular, in the hypothesis of small deformations and assuming that the nozzle is constrained to maintain its initial shape, the stress in the liner wall, defined by the relation 2.20[1], takes on a butterfly pattern as visible in figure 2.17.

$$\sigma_w = \frac{2\beta E \Delta T}{1-\nu} \tag{2.20}$$

Yield stress is often exceeded.

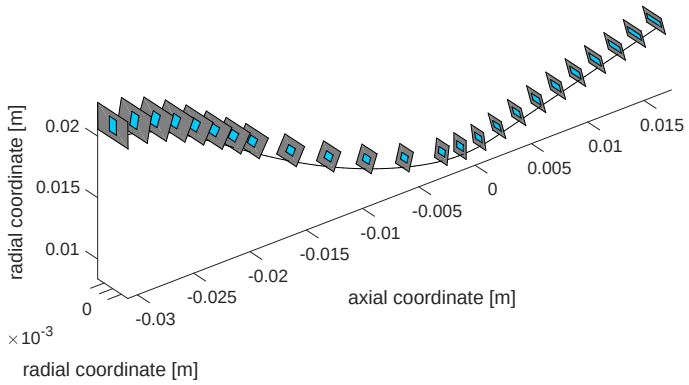

Figure 2.12: Channel geometry

2.4.4 Heat transfer theory

Before proceeding in detail in the analysis of the heat exchange, it is opportune to introduce some basic definitions, notions and mathematical models for the quantification of the convective heat exchange. From the vast literature available on the subject, it is clear that the phenomena of heat transport are among the most complex in nature. In particular, analytical quantification is difficult because a large number of physical quantities is involved and often there is coupling with other physical phenomena. For this reason only a few simple physical problems admit solution in closed form, most of it is experimentally studied and described with empirical equations. The phenomenon of heat transfer by convection has long been studied in the past. Newton was certainly among the first to understand that the exchange depended on numerous physical quantities and a completely general analytic treatment was not possible. He however came to the conclusion that the heat exchange could easily be expressed through the following reported equation.

$$Q = \alpha A \Delta T \tag{2.21}$$

Where α encompasses all geometric dependencies, the physical quantities of the fluid and its motion properties:

$$\alpha = f(D_h, \bar{v}, \rho, \mu, \lambda, c_p) \tag{2.22}$$

Its determination took place experimentally with great expenditure of time, resources and limiting the field of validity to specific configurations and under certain conditions. The evolution of mathematics has subsequently led to refine the mathematical models allowing to investigate specific cases particularly relevant in the industrial field, such as the forced convection in ducts.
In literature there are both dimensional analyzes supported by experimental validations, and analytical treatments limited to certain working conditions as the *Reynolds Analogy*. In any case, although analytical theories are available, the final evaluation of the heat transfer requires that some coefficients are nevertheless evaluated or corrected experimentally. The advantage of the analytical approach allows only to limit the experiments and the necessary validation measures.

Dimensional analysis method

The description of physical phenomena occurs through mathematical relationships that correlate the various physical quantities. This first model, very simple and independent from the studied physical phenomenon, only requires that the correlation used in the description is dimensionally homogeneous, i.e. that all the variables of the relationship have the same units of measurement. It is important to specify that the effective application of the method can't be entirely analytical, it requires in fact a consistent experimental support for validation and correction. The main advantage of this model is that of defining links between groups of physical and non-individual quantities, allowing to manage the experimental data in an efficient way and, even more important, to generalize the results with specific theories.
The mathematical foundation of the model is Buckingham theorem and attests that:

> Considered a physical phenomenon described by *n* quantities, if the between *n* variables *m* are fundamental quantities (i.e. sufficient to define a base of the dimensional space) then the physical problem can be expressed through *n-m* dimensionless groups.

In thermodynamic phenomena the fundamental quantities are: length $\mathcal{L}$, mass $\mathcal{M}$, time $\mathcal{T}$ and temperature θ. Starting from the quantities that describe the coefficient of convective exchange α and expressing them according to the previous four fundamental variables, it is possible to obtain the following dimensionless groups:

$$Nu = \frac{\alpha D_h}{\lambda} \tag{2.23}$$

$$Re = \frac{\rho \bar{v} D_h}{\mu} \tag{2.24}$$

$$Pr = \frac{c_p \mu}{\lambda} \tag{2.25}$$

The previous groups can be interpreted as follows. The Nusselt number relates the convective heat transport compared to the conductive heat, the Reynolds number relates the inertia forces (momentum) over the dissipative forces and the Prandtl number represents the kinematic diffusivity over the thermal one. Starting from the previous dimensionless groups it is now possible to express the equation 2.22 with:

$$Nu = F(Re, Pr) \tag{2.26}$$

From experimental analyzes it emerges that the function F can be described with the following equation:

$$Nu = CRe^m Pr^n \tag{2.27}$$

with *C,m,n*, obtained from the elaboration of experimental measures. Always from the previous dimensionless groups it is possible to obtain the following group:

$$St = \frac{Nu}{Pe} = \frac{Nu}{RePr} = \frac{\alpha}{\rho \bar{v} c_p} \tag{2.28}$$

The last group, i.e. Stanton number, relates the heat flux to an interface with the convective heat flux.
Some further observations on the Prandtl number.
In the convective heat exchange there is the coexistence of a thermal boundary layer and one related to the momentum. Generally the two do not coincide. For simplicity, consider a flow over a flat plate at a temperature different from that of the fluid. On the plate two boundary layers are developed and the thickness depends on the boundary conditions and on the properties of the fluid. It is observed that for fluids with $PR >> 1$ the thickness of the thermal boundary layer is lower than that of the velocity whereas for $Pr << 1$ the thickness of the velocity boundary layer is lower than the thermal one. For $Pr \approx 1$ the thicknesses are comparable. In other words, for $Pr < 1$, the points of the field between the thermal boundary layer and the velocity boundary layer will only feel the influence of the wall temperature while the velocity field remains undisturbed. Considering this, the Prandtl

number can also be understood as the ratio between the thicknesses of the boundary layers $Pr \approx \frac{\delta_{hy}(x)}{\delta_{th}(x)}$.

Entrance effect

The previous dimensionless groups and the equation 2.27 allow to treat most of the convection problems inside conduits in which the temperature and velocity field are fully developed. In reality these conditions are not always satisfied due to variable piping geometries and / or different heating / cooling conditions on the wall. More simply we can also refer to the section at the entrance to the conduit in which the fluid adapts to the new boundary conditions. In these cases heat transfer is more intense and its quantification requires the introduction of further dimensionless groups. In the hypothesis that the temperature profile is fully developed, the following dimensionless group is defined [20].

$$Gz = RePr\frac{D_h}{L} \tag{2.29}$$

where L is the distance from the inlet section. Generally Gz is a value obtained experimentally and provides indications over which length it can be assumed that the transient has become extinct. There is no general reference value, each empirical equation is accompanied by its own values that limit its validity.

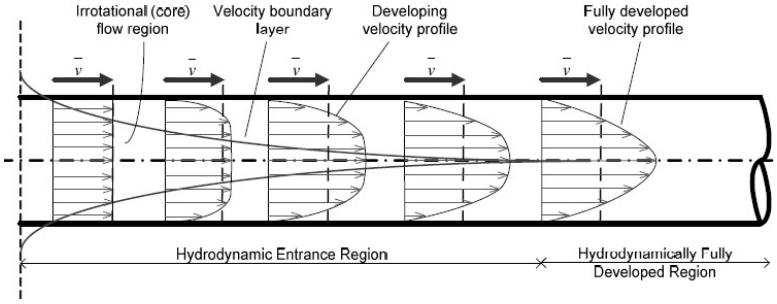

Figure 2.13: Development of the velocity profile[4]

From the figure 2.13 it is observed that in the input section the velocity profile is the undisturbed one, then, due to the dissipative actions of the viscosity, the velocity at the wall progressively reduces to the condition $v_w = 0$. In relation to the boundary conditions, a laminar flow condition, as in the figure, or turbulent can be achieved. In a similar manner, if a fluid at a uniform temperature enters a tube with a different surface temperature, the fluid also

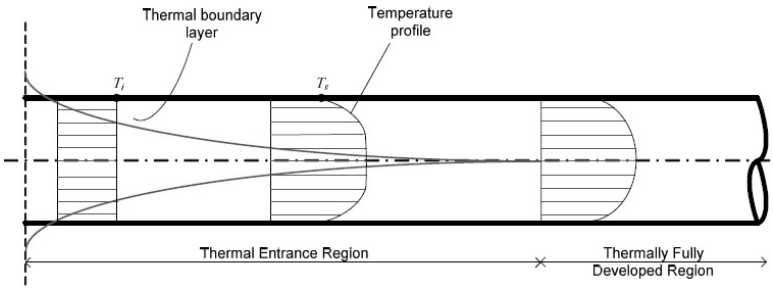

Figure 2.14: Development of the thermal profile[4]

develops a thermal profile. The fluid particles in direct contact with the wall of the tube assume the surface temperature, which initiates convection heat transfer in the tube. The layer of fluid directly adjacent to the tube wall is known as the thermal boundary layer. In the case of laminar flow in a tube, the thermal boundary layer extends to the centre line of the tube, and its thickness is independent of the velocity. Therefore, the temperature gradient at the wall and the heat transfer coefficient is also independent of velocity. In the case of turbulent flow, turbulence improves mixing in the core flow of the tube. This in turn allows for an increase in the heat transfer coefficient and a consequent thinning of the viscous layer adjacent to the wall of the tube[4].
From analogy between the velocity and thermal boundary layer, as the entrance hydraulic length is defined as the distance required for the friction factor to decrease to within 5% of its fully developed value, the thermal entrance length is the distance required for the Nusselt number to decrease to within 5% of its fully developed value. Generally two conditions are observed, the most widespread is that in which both profiles develop simultaneously the second, however, considers that the velocity profile develops before the fluid is cooled/heated. It's observed that for laminar flows the entrance length are evaluated as follow[4]:

$$\begin{aligned} L_{h,lam} &= 0.05 Re D_h \\ L_{th,lam} &= 0.05 Re Pr D_h \end{aligned} \tag{2.30}$$

while for turbulent flows both lengths are assumed equal to 10 times the diameter of the duct. Keeping in mind that the number of Pr gives indications relative to the ratio between the thicknesses of the boundary layers, it is clear from the previous equations that Pr also describes which of the two profiles is developed faster.

Bulk, wall and average temperature

Another particularly relevant problem in the evaluation of the convective heat transfer is the presence of a thermal gradient between the bulk and the wall. The axis temperature is often called bulk and is used in the algorithms even if it is difficult to evaluate experimentally. Bulk temperature is the highest/lowest of the field, according to boundary conditions. As regard the the physical phenomenon, molecules of fluid in contact with the wall are brought to its temperature, while those closer to the axis of the duct are affected less. To complicate the analysis is the strong dependence of the properties of the fluid with the temperature, as for example for the viscosity and in a less significant way for the density and the specific heat. For this reason, to simplify the analysis often refers to the average temperatures that allow to treat the fluid as if it were isothermal. Among the various formulations we mention three average temperature[20].

$$\bar{T}_A = \frac{\int_A T dA}{A} \tag{2.31}$$

$$\bar{T}_{\dot{V}} = \frac{\int_A vT dA}{\int_A v dA} \tag{2.32}$$

$$\bar{T}_{mix} = \frac{\int_A T c_p v \rho dA}{\int_A c_p v \rho dA} \tag{2.33}$$

The first one is a simple average on the section and requires only the knowledge of the temperature profile. The second one is a weighted average on the volumetric flow rate and require to know also a velocity profile. The last equation refers to adiabatic mixing temperature and, among these, represents the most precise approximation but it is also more complicated to evaluate.

Observations on the selection of the reference temperature.

In general, referring to the temperature of the bulk is certainly the fastest and easiest solution to quantify the heat transfer, but it is not always the most suitable choice. This is because the bulk is the highest/lowest temperature of the section's field, depending on whether it cools/warms, it can give rise to temperature differences that in absolute value are maximum compared to the cases where average temperatures are used, with the risk of overestimating the heat exchanged. Referring to average temperatures can be an alternative solution even if they require knowledge of temperature profiles and other quantities, depending on the average used, and these information aren't always available especially for ducts with sections

different from the circular one. In this case the quantification is purely numerical and involves the discretization of the section. In this project, since a one-dimensional model has been implemented, reference has been made to the temperature of the bulk, even if, averages have been evaluated using velocity profiles obtained analytically for laminar motion and experimentally for turbulent motion in order to verify differences. It should be noted that there are no analytical descriptions for each type of section, therefore we referred to those for circular sections having an equivalent hydraulic diameter. The thermal profiles have been described by analogies with the hydraulic ones even if adapted to the different boundary conditions. From this evaluation it emerged that for this case, the differences between the average temperatures are however limited.

Boiling phenomena in coolant

This section briefly discusses the phenomenon that leads to liquids boiling because it strongly conditions the design of the cooling system. The coolant side heat-transfer coefficient α_{col} is influenced by many factors and due to high fluxes and temperature, coolant may become corrosive, may decompose or deposit impurities upon the heated surface, thereby reducing cooling effectiveness[19]. For this reason α_{col} can be estimated exclusively experimentally.
The phenomenon that leads to the formation of nucleation and then of the boiling, described by the image 2.15, is complex and involves numerous phenomena.

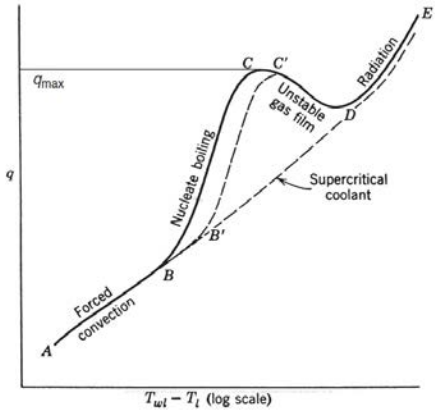

Figure 2.15: Regimes in transferring heat from a hot wall to a flowing liquid[1]

As can be seen from the image, the behavior is strongly influenced by the operating pressure, so that two different curves are used to describe subcritical fluids and supercritical ones. Having fixed an initial condition (pt.A), it is observed that as the heat flux increases, the

	H_2O_2	N_2H_4	Kerosene	N_2O_4	H_2O
P_{cr} [MPa]	22	8	2	10.1	22.064

Table 2.5: Critical pressure for some fluids

difference in temperature between the wall and the fluid increases too. From point B the behavior of the fluids begins to differentiate. For subcritical fluids the phenomenon of nucleation begins, that is the formation of vapor bubbles between the roughness of the wall. These small nuclei-like bubbles, cause local turbulence, that break away from the wall and collapse in the cooler liquid. The turbulence induced by the bubbles movement, mix the fluid as the result the heat transfer rate is increased without a proportional increase in the temperature drop across the film. Finally, a further increase in the flow leads to complete ebbollition. It is observed that for subcritical fluids, in correspondence of the boiling (pt.C) the heat flow is maximum. Finally for further increases of $\dot{q}$ the wall assumes a temperature so high as to generate an initially unstable gaseous film, that at the end, it completely isolates the wall from the fluid (pt.D to E). For supercritical fluids this intermediate phenomenon does not occur.

Taking into consideration the whole phenomenon, it's possible to say that for achieving a good heat-absorbing capacity of the coolant, pressure and flow velocity are selected so that boiling is permitted only locally, but the bulk of the coolant does not reach this boiling condition[1]. However, it should be noted that this working point is not always satisfactory, especially for refrigerants such as hydrocarbons, where the cracking of the molecules can generate deposits that reduce conductivity, and even more dangerous for oxidants such as hydrogen peroxide in which the boiling can determine the decomposition and explosion. In addiction some gas bubbles inside the fluid can interfere with the injection. For all these reasons in this project has been decided to work only between points A and B and avoiding boiling phenomena. As reference some critical pressures of fluid used in rocketry.

2.4.5 Heat transfer model and empirical equations

The core of the algorithm is represented by the following model of heat exchange. From experimental data, it's observed that only 0.5 to 5 % of total energy generated by combustion is transmitted to all internal surfaces of thrust chamber exposed to hot gases[2]. Generally the most stressed point of the nozzle is represented by the throat while the less stressed area is at the outlet. Indicatively, the specific thermal flows reach very high values, about $[MW/m^2]$,

determining the need to thermally protect the wall.
In this work all the phenomena involving heat transport have been considered, as all three manifest and influence the process.
From a global observation stand point, it is possible to state that the presence of the nozzle wall divides the domain into three parts and each is characterized by a dominant heat transport phenomenon. The three sub-domains are represented by the gas side, the wall and the coolant side. Experimental analysis shows that in the gas side, the heat transport is mainly convective, about 80%, the remaining 20% radiative [21]. The conduction on the gas side is totally negligible, while it isn't in the wall where it's the only transport phenomenon. In the coolant side instead there are both conduction and convection.
From a circuit point of view, the heat transfer model applied to the geometry of figure 2.10 can be represented with the follow diagram with concentrated parameters of figure 2.16.

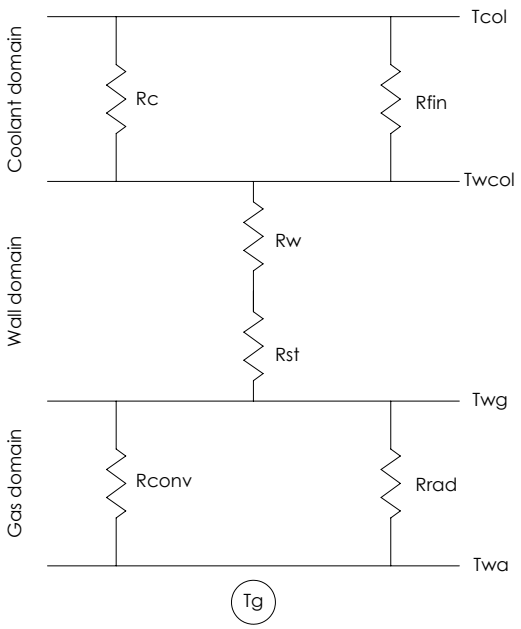

Figure 2.16: Equivalent electric circuit of the heat transfer model

From the literature it emerges that the scheme of figure 2.16 is frequently used and sometimes adapted to the objectives of the study with additions or simplifications [1], [19], [22], [23], [2] and [24]. In this project, as anticipated, the circuit diagram has been subdivided into three domains and in each of them has been shown thermal resistances representative of the transport phenomenon. The interface between the domains has been represented by

a horizontal line to which a temperature is associated. Analyzing the previous circuit, the following observations are made. In order to maximize engine performance, the heat flow through the thermal resistances R_{conv} and R_{rad} must be strongly limited while, to reduce the thermal stress in the wall and to avoid the perforation, it is necessary to maximize that between the wall and the refrigerant.
As regard the temperature profile, it's expected something similar to the one described in the figure 2.17.

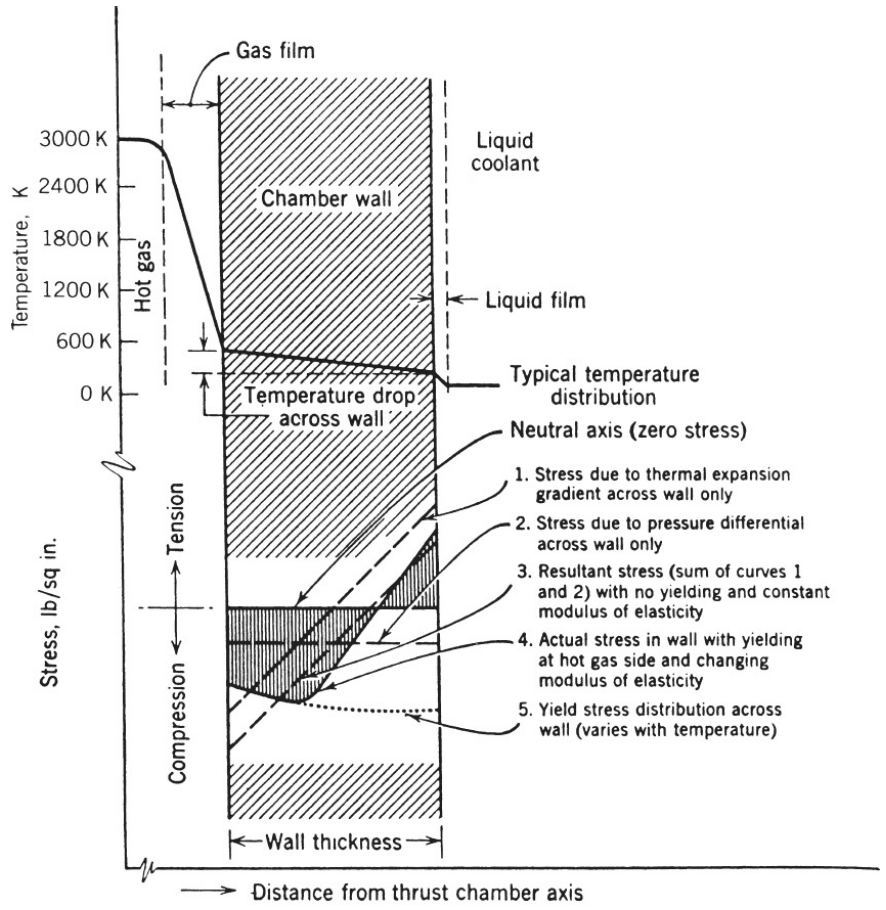

Figure 2.17: Temperature profile and stresses in the wall[1]

As for the boundary conditions, heat transfer problems can be treated in 3 modes: uniform flow (*UHF*), uniform temperature on the wall (*UWT*) and Neither boundary [4]. Conceptually, the nozzle is a heat exchanger in which both the wall temperature and the heat flow vary, however in the numerical analysis conducted it has been assumed to consider the slab with a *UHF* condition and in which the heat flux is calculated in the its midpoint.

Gas domain

The domain of gas is characterized by two thermal flows, the convective and the radiative ones. Both flows are competitors and directed towards the nozzle wall for this reason the total flow is given by:

$$\dot{q}_{tot} = \dot{q}_{conv} + \dot{q}_{rad} \tag{2.34}$$

Now move on to the description of the two components. The convective heat flow was quantified with an empirical equation attributed to *Bartz*. This equation[2] allows to calculate the convection coefficient between the gas and the liner wall.

$$\alpha_g = \frac{0.026}{D_t^{0.2}} \left(\frac{\mu_g^{0.2} c_{p,g}}{Pr_g^{0.6}} \right) \left(\frac{P_{cc}}{c^\star} \right)^{0.8} \left(\frac{A_t}{A} \right)^{0.9} \chi \tag{2.35}$$

$$\chi = \left[0.6 \frac{T_{wg}}{T_{cc}} \left(1 + \frac{\gamma - 1}{2} M^2 \right) + 0.5 \right]^{-0.68} \left(1 + \frac{\gamma - 1}{2} M^2 \right)^{-0.12} \tag{2.36}$$

It is fundamental to note that the previous relationship has been obtained for axial outflows in the combustion chamber, to date, no empirical relations which quantify the convective coefficient are available for swirl combustions. All quantities referred to the combustion chamber are considered as total quantities for this reason $T_{cc} = T^0$ and $P_{cc} = P^0$. In particular, it has been observed that the previous equation, to better describe the phenomenon, requires a correction of the temperature of the gas near the wall. We therefore refer to the recovery temperature frequently defined with the following relation.

$$\begin{gathered} T_g = T_{cc} \left[\frac{1 + r_F (\frac{\gamma-1}{2}) M^2}{1 + (\frac{\gamma-1}{2}) M^2} \right] \\ r_F = Pr_g^{0.33} \end{gathered} \tag{2.37}$$

And finally convective heat transfer can be described with:

$$\dot{q}_{conv} = \alpha_g (T_g - T_{wg}) \tag{2.38}$$

The radiative component is also difficult to evaluate analytically because it is the sum of the flux from the hot gas and the energy re-radiated back from the wall. This means that for a careful evaluation a model with all the reflections should be implemented, which takes into account the variable properties of the gas with the temperature and the scattering in

the nozzle [23]. Since the approach used in this project is one-dimensional, it is more appropriate to refer again to empirical equations. It has been observed that gases with symmetrical molecules, such as hydrogen, oxygen, and nitrogen, don't show many strong emission bands[¶]. For this reason they do not absorb or increase radiation and in turn heat transfer is not affected. Heteropolar gases, such as water vapour, carbon monoxide and carbon dioxide instead, have strong emission bands. For this reason the evaluation has been limited to these[2].

$$\dot{q}_{rad} \approx \dot{q}_{rad,H_2O} + \dot{q}_{rad,CO_2} \tag{2.39}$$

$$\dot{q}_{rad,H_2O} = 3.5 P_{H_2O}^{0.8} L_e^{0.6} \left[\frac{T_g}{100}^{3} - \frac{T_{wg}}{100}^{3} \right] \tag{2.40}$$

$$\dot{q}_{rad,CO_2} = 3.5 (P_{CO_2} L_e)^{\frac{1}{3}} \left[\frac{T_g}{100}^{3.5} - \frac{T_{wg}}{100}^{3.5} \right] \tag{2.41}$$

were $L_e = 0.6D$. It should be noted that the partial pressures of carbon dioxide and water can be easily obtained from the results of the CEA.

Wall domain

Now pass to the wall domain. In this project it has been assumed that the wall was made not only by the motor case but also by a thin layer of soot typical of combustion with hydrocarbons. For this type of transport phenomenon it is possible to use an analytical treatment described by the conduction equation (or Fourier equation).

$$\dot{q}_{cond} = \sum_{i=1}^{n} \frac{\lambda_i}{t_i} A (T_{wg} - T_{wcol}) \tag{2.42}$$

As regard the thickness of soot again has been used empirical equations that come from experimental observation for $P_{cc} < 100$ [bar]. For the convergent section:

$$\begin{aligned} t_{soot} &= 0.00412113 \tfrac{A_t}{A} + 0.0041023 \quad && 1 < \tfrac{A_t}{A} < 2 \\ t_{soot} &= 0.01234 && \tfrac{A_t}{A} > 2 \end{aligned} \tag{2.43}$$

[¶]Emission and radiation in infrared field is directly connected to the vibrational state of molecule

while for the divergent:

$$\begin{aligned} t_{soot} &= -0.0000442\frac{A_t}{A}^2 + 0.0011448\frac{A_t}{A} + 0.007092 \quad & 1 < \frac{A_t}{A} < 12 \\ t_{soot} &= 0.01445 & \frac{A_t}{A} > 12 \end{aligned} \tag{2.44}$$

In these equations thickness is given in [in].

Coolant domain

The domain of the coolant, like that of gas, is characterized by different phenomena of heat transport. Observing the figure 2.10, it is clear that the transmission phenomena involved concern conduction, in thermal fin and convection towards the coolant. According to literature [23], [22], [24] the total heat flux transferred is given by the following.

$$\dot{Q} = \alpha_{col} A_{ch} (T_{wcol} - T_{col}) + \dot{q}_{fin} A_{fin} \tag{2.45}$$

where can be expressed as $\dot{q}_{fin} = \alpha_{col}(T_{wcol} - T_{col})\eta_{fin}$. Now assuming that the tip of the fin, connected with the external jacket is also adiabatic, the following equations are obtained from the fin theory[20].

$$m = \sqrt{\frac{\alpha_{col}}{\lambda \delta}} \tag{2.46}$$

$$\eta_{fin} = \frac{\tanh(m h_{fin})}{m h_{fin}} \tag{2.47}$$

where $\delta = \frac{w_{fin}}{2}$. As regard the elementary slab areas, if dx is an axial step defined by the norm between two mesh points as follow $dx = |x(j) - x(i)|$, $A_{ch} = w_{ch} dx$ and the fin's area in contact with the coolant $A_{fin} = 2h_{fin} dx$.
The model for heat transfer in the coolant is basically terminated.
Now consider the convective exchange coefficient and its quantification. Once again from the extensive literature on the subject, a series of empirical relations that describe the coefficient α_{col} by means of the dimensionless group Nu have been identified. In particular, it is noted that all the reports describe correlations only for circular pipes, in steady state and any other conditions are specified in each case. The fact that in this project channels have sections different from the circular does not introduce further difficulties because it can be easily referred to the hydraulic diameter $D_h = 4A/l$. To guarantee greater flexibility, both the laminar and the turbulent equations were used, making appropriate interpolations in

the transition regime. It is good to specify that from the thermodynamic point of view it would be better to work in the turbulent regime as the exchange coefficient is on average higher even if, at the expense of the pressure drops. The equations for forced convection in ducts used in this work are listed below.
For laminar flows we have the Sieder and Tate equation and the validity field is for $100 < Re < 2100$, $0.48 < Pr < 16700$, $Gz \geq 10$ and $\mu \geq 1e^{-4}$[Pa s].

$$\mathrm{N}_{col} = 1.86\left(\frac{Re_{col}Pr_{col}D_h}{l_{ij}}\right)\left(\frac{\mu_{bulk}}{\mu_w}\right)^{0.14} \tag{2.48}$$

For the transitional flow has been followed a procedure described in Melissa's master thesis[4].

$$\begin{gathered} Nu_{col} = \varphi Nu_{laminar} + (1-\varphi)Nu_{turbulent} \\ \varphi = 1.33 - \frac{Re_{col}}{6000} \end{gathered} \tag{2.49}$$

Finally for the turbulent:
The Sieder and Tate equation valid in the field $Re_{col} > 10000$, $0.7 < Pr_{col} < 17600$ [4] and $\frac{l}{D_h} > 10$. This equation is valid for UWT condition however the size of the slab is very small for this reason and by accepting a small error, it is possible to refer to a average temperature. It is observed that there is no uniformity in the field of validity for this equation, sometimes is required $\frac{l}{D_h} > 60$, with a Prandtl limitation $0.7 < Pr < 16700$ and a restriction for a certain class of fluid[20].

$$Nu_{col} = 0.027Re_{col}^{0.8}Pr_{col}^{\frac{1}{3}}\left(\frac{\mu_{bulk}}{\mu_w}\right)^{0.14} \tag{2.50}$$

The Gnielinski correlation[4] valid in the field $3000 < Re_{col} < 5e^6$, $0.5 < Pr_{col} < 2000$ and the friction factor can be obtained both by Moody chart or from Petukhov equation.

$$Nu_{col} = \left(\frac{\frac{f}{8}(Re_{col}-1000)Pr_{col}}{1+12.7(\frac{f}{8})^{0.5}(Pr_{col}^{\frac{2}{3}}-1)}\right) \tag{2.51}$$

$$f = (0.79\ln(Re_{col}) - 1.64)^{-2} \tag{2.52}$$

For taking into account also entrance effect, other empirical equation have been considered both for laminar and turbulent. For laminar flow with $Re_{col} < 2300$ and simultaneous

development of both boundary layer:

$$Nu_{col} = 0.664\left(\frac{D_h}{l}\right)^{0.5} Re_{col}^{0.5} Pr_{col}^{0.33} \tag{2.53}$$

For transition to turbulent with $2700 < Re_{col} < 7000$ and always a simultaneous development condition:

$$Nu_{col} = 0.01\left(\frac{D_h}{l}\right)^{0.37} Re_{col}^{1} Pr_{col}^{0.37} \tag{2.54}$$

Finally for $Re_{col} > 10000$ and the same condition for boundary layers as before:

$$Nu_{col} = 0.036\left(\frac{D_h}{l}\right)^{\frac{1}{18}} Re_{col}^{0.8} Pr_{col}^{0.33} \tag{2.55}$$

Convergence and temperature evaluation

The search for the thermal flow takes place through an iterative process on the one-dimensional element. The known quantities are the geometry, that is also constant for the single element, the temperature of the incoming coolant and the recovery temperature on the gas side. Therefore, taking into consideration that the boundary conditions are known as also the mathematical model represented by the circuit of figure 2.16, it is possible to identify a solution that satisfies the various conditions. Now, since within the equations appear coefficients that depend in turn on the various unknown temperatures it is understood that it is not possible to proceed analytically, but only numerically. In addiction, although the size of the element is deliberately small to reduce the magnitude of the axial temperature gradients, they can never be completely eliminated. For this reason it was decided to consider the average flow exchanged considering as the gas recovery temperature that it is in the middle point of the element.

The numerical method used to search for the solution is the bisection. Once the convergence has been completed, it is possible to calculate the temperature in output to the channel by the following equation.

$$T_{col_j} = \frac{Q}{\dot{m}_{ch} c_p(T, P)} + T_{col_i} \tag{2.56}$$

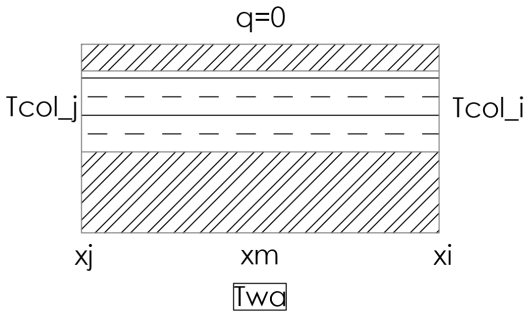

Figure 2.18: Scheme of the mono-dimensional element

2.4.6 Pressure losses calculation

The assessment of load losses has been made by distinguishing between continuous and localized ones. For the former, the following equation has been used according to the whole literature.

$$\Delta P_x = f \frac{l}{D_h} \rho \frac{\bar{v}^2}{2} \tag{2.57}$$

Regarding the determination of the friction factor has been used the well known Colebrook-White equation.

$$\frac{1}{\sqrt{f}} = -2 \log \left(\frac{\xi}{D_h 3.71} + \frac{2.51}{Re\sqrt{f}} \right) \tag{2.58}$$

where ξ is the roughness.

The analysis of the particle size of the metal powder used in the $3D$ printing process pro-

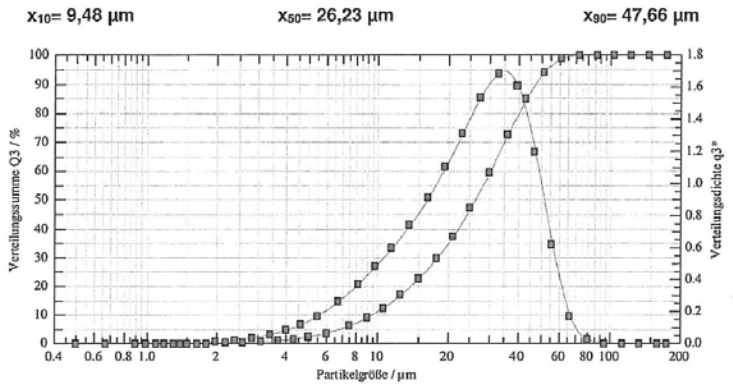

Figure 2.19: Granulometry of the metal powder

vided by the company showed that roughness distribution is around $35[\mu m]$. If you want

to have 99.83% confidence, the roughness value is around $70[\mu m]$. Any support evaluations can be made by measuring the surface with a touch probe.
As regards the concentrated pressure losses, an empirical formulation has been used which assigns a representative coefficient to the inlet and outlet geometry.

$$\Delta P_{loc} = \kappa \rho \frac{\bar{v}^2}{2} \tag{2.59}$$

From literature it is observed that for abrupt contraction, as inlet κ is 0.5, while for abrupt expansions that is to exit, κ is 1.

2.5 Results

In this section will be treated all the result obtained from analysis and critically discussed.
The code require in input all designs data, starting from requisites and the properties of the coolant and of the material. Some optional inputs are also available as the inclusion or not of the radiative model of the gas, the presence or absence of the soot layer and whether to graph the results. Channel geometry is defined iteratively by the user progressively adapting the AR and w_{ch} in relation to the results obtained. As regards material,for simplify the use, a script has been already prepared containing all data taken from commercial datasheet and the only input required is to choose it among listed.
The results are provided both graphically and numerically on video. As for the graphs, they are generated automatically and summarize the geometry of the nozzle and the size of the channels. Instead, for the fluid-dynamic and thermodynamic quantities, a single figure is generated containing 6 subplots in order to easily monitor the whole phenomenon (see figure 2.20). In this section, for the sake of analysis, they will be treated separately.

In order to better understand the dependencies between the various physical quantities different scenarios have been studied, in each of which specific parameters have been modified to highlight the influences.

2.5.1 Scenario for different mass flow rates and inlet pressures

In this first analysis the behavior of the engine has been studied by varying the coolant flow rate and its inlet pressure. The study has been conducted assuming to maintain unaltered all the geometries (nozzle and channels) and to progressively vary the input pressure and the coolant flow. The motor supply conditions ($\dot{m}_p = cost$) has been kept constant for all

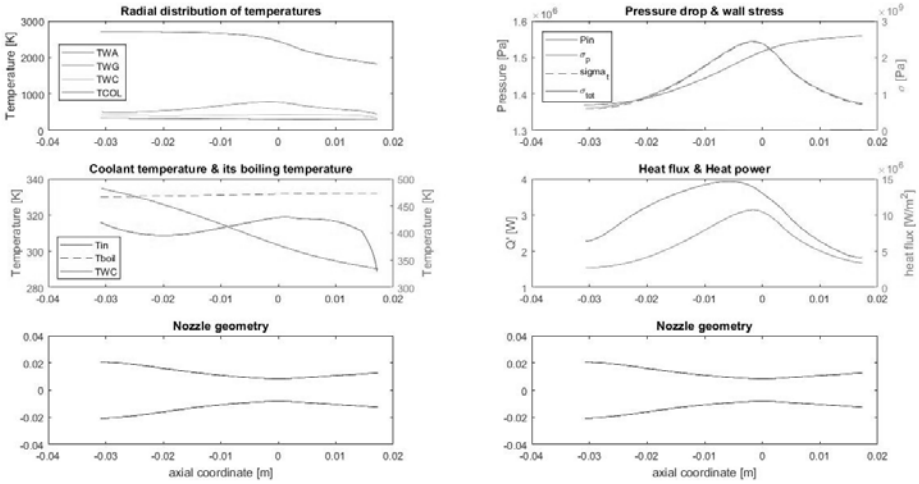

Figure 2.20: Example of result supplement

the tests by imagining to decouple the regenerative system output with the catalyst input ($\dot{m}_{ox} \neq \dot{m}_{col}$ and $P_{ch,out} \neq P_{in,cat}$). The analysis highlighted the following trends (figures 2.21).

From the subfigures in 2.21, it is possible to immediately observe the strong dependence of the performances of the regenerative cooling with the mass flow rate of the coolant. Less evident is the link with the inlet pressure, despite the range of variation extending between 15-29 [bar]. Since the flow rate of the coolant is fixed, pressure variations affect only the properties of the fluid and, as noted above, the dependence of ρ, μ, λ, c_p is minimal depending on the pressure, except for the boiling temperature T_b. The high pressure working condition results to be more suitable in high mass flow rate configurations where high flow rates entail high coolant speeds, higher pressure losses and a greater boiling temperature reduction. Working at higher pressures therefore allows for a larger margin to lie between T_{wcol} and T_b. For increasing pressures, a slight increase in total absorbed heat and wall thermal stress has been observed. While a slight reduction in pressure losses and maximum wall temperature has been observed.
Further checks highlighted the following observations. Increased mass flow rates raise the speed of the coolant and the Reynolds number, increasing also the convective transport coefficient and reducing the temperature T_{wcol}. It is observed that with the raise of Re the temperature difference between T_{col} and T_{wcol} is reduced (because they improve the transport properties between wall and fluid) but increases also that between T_{wg} and T_{wcol} rising

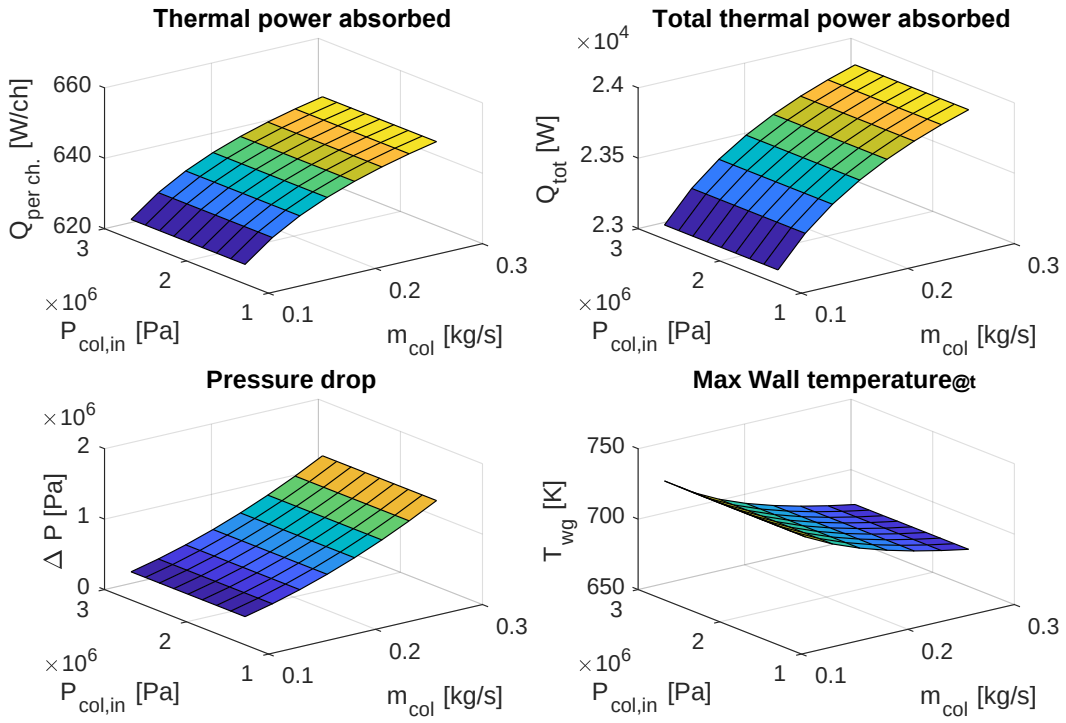

Figure 2.21: Global result for mass flow rate & pressures scenario

thermal stress(to note thatλ_w remains unchanged). Finally, it is noted that higher mass flow rates result in lower $T_{col,out}$ even if the total thermal power transferred to the fluid is greater. Recalling that $\dot{Q} = \alpha_{col} A \Delta T$, we deduce that the mass flow rate increases the α_{col} more than it reduces the ΔT.

2.5.2 Scenario for different materials

This second study wanted to quantify the influence of the nozzle material in its cooling. Different metals have been tested, in the awareness that not all are compatible with the H_2O_2. The study has been conducted maintaining unaltered geometry (nozzle and channels) and operating conditions ($P_{cc}, \dot{m}_p, F...$). The materials considered are the following: AISI630, Inconel718, Al5005, Al8008, Cu-GRCop$_{84}$.
Principal results are highlighted in figure 2.22.

The decision to analyze these metals depended on concrete implementation possibilities and academic interest. In particular, the Inconel718 has properties very similar to the AISI630 but allows to reach higher operating temperatures also presenting good possibilities of com-

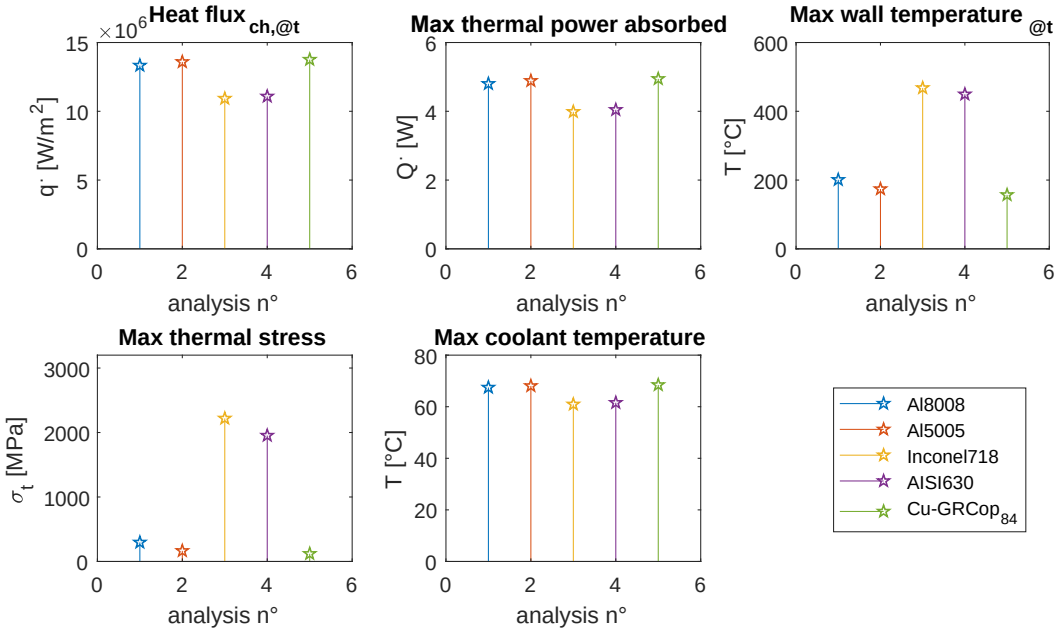

Figure 2.22: Global results for different materials

patibility with hydrogen peroxide. As far as aluminum is concerned, it has average thermal properties much better than the previous metals even if its mechanical properties are relatively scarce for this application. Two types of aluminum have been considered, one in the 5000 series and one in the 8000 series. From the point of view of properties, the 5005 and 8008 are quite similar, even though the 8008 is more suitable for temperature applications. In any case, being alloys, full compatibility is not guaranteed. Finally, a copper alloy studied and considered particularly suitable for regenerative cooling applications by NASA, has been analyzed. This alloy is certainly incompatible with hydrogen peroxide (Class 4).
It should be noted once again that the properties of the metals used in these analyzes derive from technical datasheets provided from suppliers and a complete temperature characterization, in the desired field and for all properties, is not always available. For this reason extrapolations have been made with consequent uncertainties on the truthfulness of the values.
From the figure 2.22 it is possible to deduce that the best conduction properties of aluminum and copper make it possible to considerably lower the maximum wall temperature (T_{wg}) and the thermal gradient developed in it, minimizing markedly the thermal stress. The best performances, from the point of view of regenerative cooling, are certainly those of copper while the worst ones are those of the Inconel718. As far as pressure losses are concerned, since the

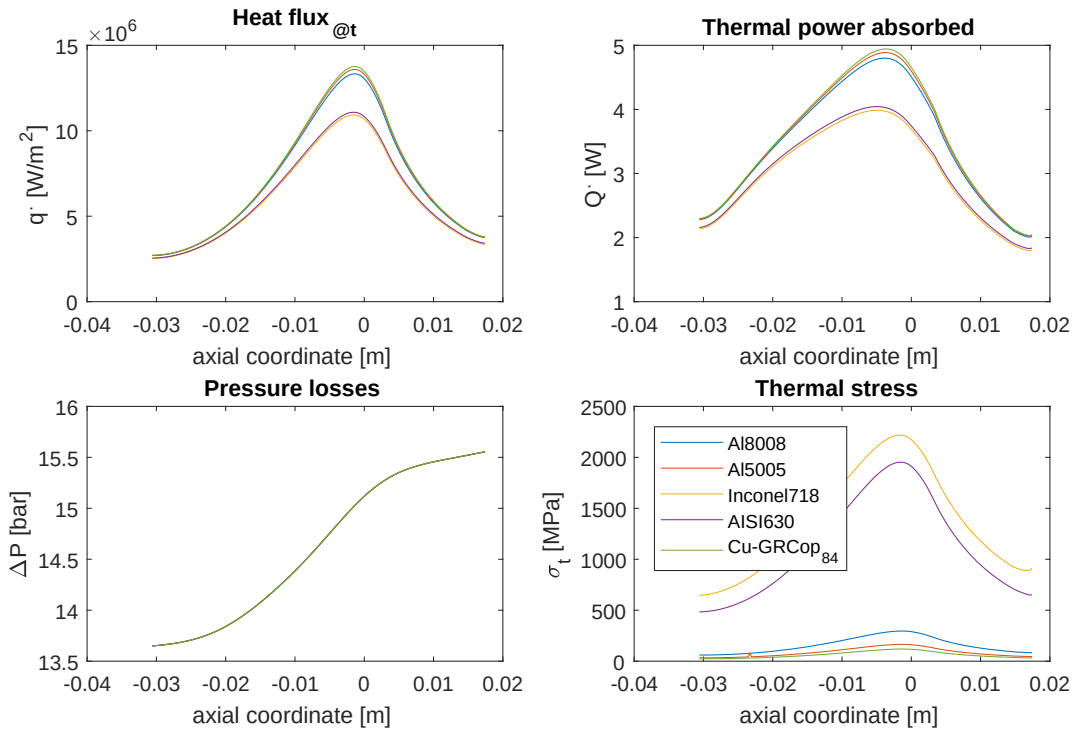

Figure 2.23: Properties of the materials scenario

geometry and operating conditions between the various tests remain unchanged, the differences are minimal and in any case imputable to slightly different coolant temperatures. From the subfigure 3 of figure 2.23 it can be seen that for the pressure the various curves coincide, unless enlargements are made. Further tests have shown that the conduction properties of copper and aluminum 5005 are so high that it also keeps the temperature T_{wg} below the boiling temperature.

Regarding the mechanical strength of the metal, the available data and the predictive formulas used show that the maximum recorded stress tension exceeds the maximum allowable for Inconel 718, AISI 630 and, for a few units, also for aluminium. Copper is the only one that remains within the allowable field. The analysis reconfirms the choice of copper as the reference metal for regenerative applications, wherever possible.

2.5.3 Scenario for different engine size

This study analyzed the influence of the motor size in regenerative cooling, assuming to maintain the number and the geometry of the channels unaltered (AR, w_{ch} cost) and to modify

the operative pressure in chamber and the thrust. The material used for the entire study is stainless steel and the outlet condition at the divergent exit is always of adapted pressure. The configurations studied are the following summarized in the table 2.6.

	P_{cc} [bar]	T_{cc} [K]	$c^\star$ [m/s]	M_m [kg/kmol]	γ	x_{CO_2}	x_{H_2O}
1	6.5	2677.11	1582.2	21.319	1.1891	0.13544	0.71443
2	9	2693.36	1586.0	21.354	1.1898	0.13639	0.71750
3	11.5	2705.05	1588.8	21.379	1.1912	0.13708	0.71973
4	14	2714.07	1590.9	21.399	1.1933	0.13762	0.72145
5	16.5	2721.34	1592.5	21.414	1.1945	0.13805	0.72284
6	19	2727.39	1593.9	21.427	1.2034	0.13841	0.72401

Table 2.6: Combustion data obtained from CEA for different engines size

First of all, the combustion data show that at higher pressures the same mixture burns at higher temperatures producing exhaust with higher molecular mass and γ, further increasing the concentrations of carbon dioxide and water. Also the speed of the sound in the combustion chamber increases.
The scenario generated the following results.

From the figure 2.24 we note that the surfaces produced by the numerical analysis are not complete. In reality it is the post processing that has reduced the field of results where $T_{wcol} > T_b$, a condition that for general hypotheses is not allowed. Let's go into more detail in the results.

As far as heat flux is concerned, it can be seen that dependence with pressure is very marked, while that linked to thrust, and consequently to the coolant mass flow rate, is limited. The reason that justifies this phenomenon is closely connected to the geometry of the nozzle. From the figure 2.25 we deduce that higher operating pressures substantially reduce the size of the nozzle while the increment of the $\dot{m}_p$ generates slightly larger nozzle. The justification for these trends derives from the equations 2.6 and 2.8. By fixing P_{cc}, $c^\star$, T_{cc} and defining the outlet conditions, c_F is also fixed. Higher thrusts imply higher m_p and from equation 2.8 higher throat areas. Instead, once the thrust and the exhaust conditions are fixed, as P_{cc} increases, there is an increase of c_F[‖] and $c^\star$, a consequent reduction of the $\dot{m}_p$ and always from the equation 2.8 a reduction of A_t.

[‖]The dependence of c_F with the pressure P_{cc} is fundamental in the atmosphere while in orbit it is insignificant

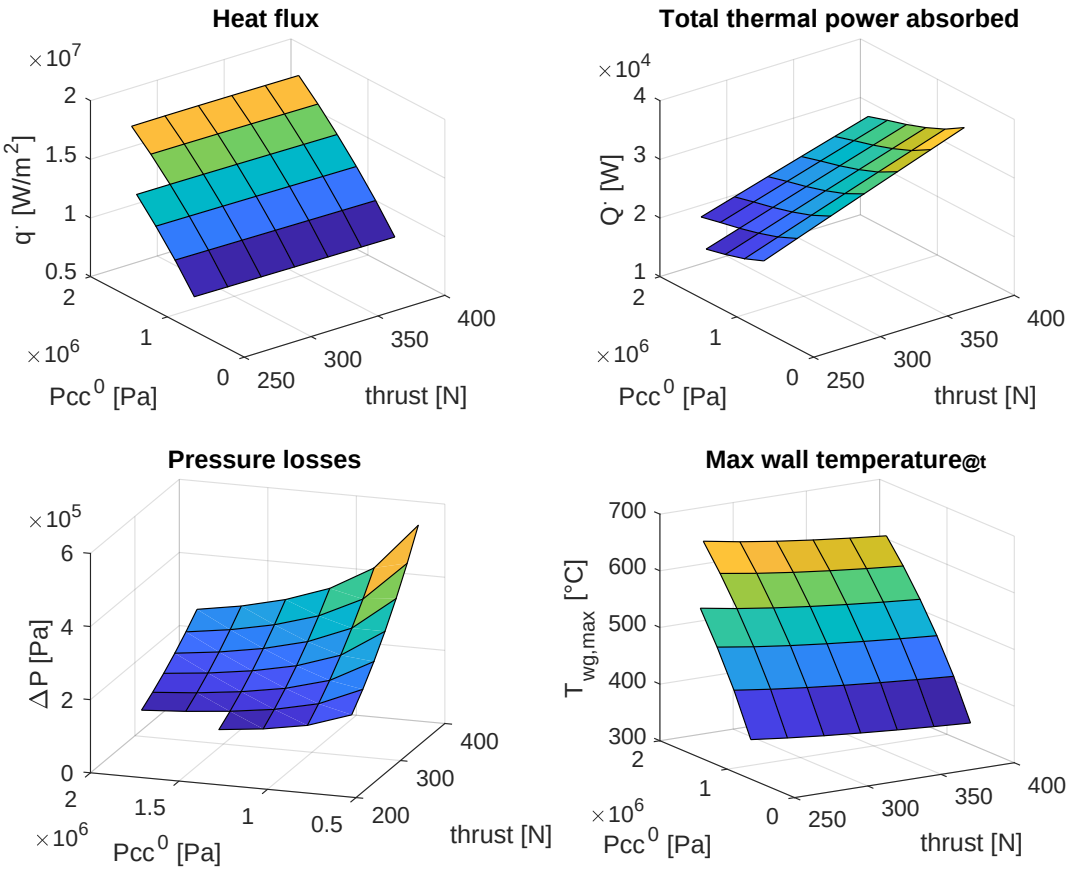

Figure 2.24: Global results from the engine size scenario

Considering the previous ones, the equation 2.35 suggests an increase in the convective coefficient, which in turn determines an increase in the heat flux.

Let's move on to the thermal power absorbed by the flux that is observed to be marked with the thrust, less with the pressure in the combustion chamber. The dependence on the thrust, and therefore with the $\dot{m}_p$, has already been discussed in the 2.5.1 section. Regarding the pressure, it is observed that as it increases, the thermal power transferred decreases progressively. This depends on the P_{cc}-size link. Higher pressures lead to smaller engines, with smaller channel lengths.

Regarding pressure losses, once again the dependence with the mass flow rate has already been discussed, the one with the P_{cc} is always connected to the dimensions and fluid properties ($f(P)$).

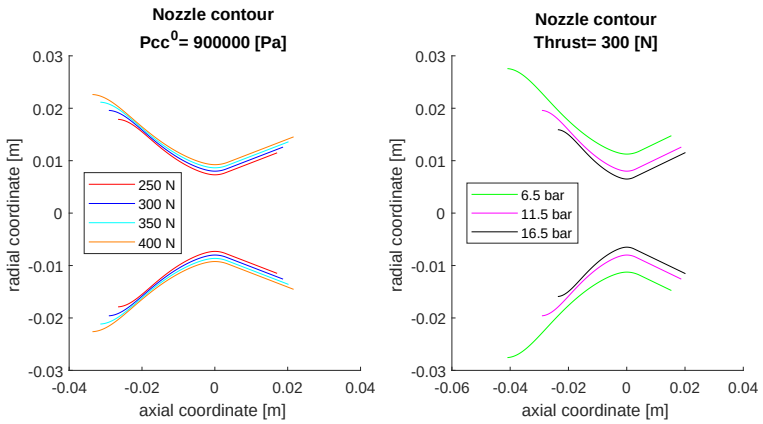

Figure 2.25: Different nozzle geometries for assigned values of P_{cc}&F

Finally, with reference to subfigure 4, it can be deduced that wall temperature depends a lot on the pressure, less with the thrust. Once the pressure is set, higher thrusts require $\dot{m}_p$ and then $\dot{m}_{ox}$ which increases the coolant side transport properties by reducing the wall temperature. Once the thrust is set, higher pressures reduce engine size, increasing heat fluxes and in turns temperatures.

2.5.4 Scenario for different channel geometry

This last scenario investigated the influence of the channel's geometric parameters such as Aspect Ratio and w_{ch} on regenerative cooling performance. This scenario has been studied with the hypothesis of maintaining the same operating conditions, geometry and number of channels for all configurations. To understand the influence of these parameters it is assumed to work with fixed geometry, i.e. $AR, w_{ch} = cost$ and not depend on the axial coordinate.

Single configuration evaluation

The result obtained from the analysis are presented in table 2.7 and in figure 2.26.

Generalization of previous data

The generalization of the study has foreseen to extend the performance evaluation investigating many more intermediate configurations. Basically, the field within which to vary AR and w_{ch} has been fixed and all the possible combinations have been analyzed.

	AR	w_{ch} [mm]	$\dot{Q}_{tot}$ [kW]	ΔT [°C]	$T_{wg,max}$ [°C]	ΔP [bar]
mod 1	0.5	0.75	23.515	46.53	428.94	9.79
mod 2	0.9	0.75	22.896	45.32	477.81	1.89
mod 3	0.5	0.9	23.246	46	450.18	3.67
mod 4	0.9	0.9	22.445	44.43	515.21	0.74

Table 2.7: AR and w_{ch} influences in channel geometry scenario

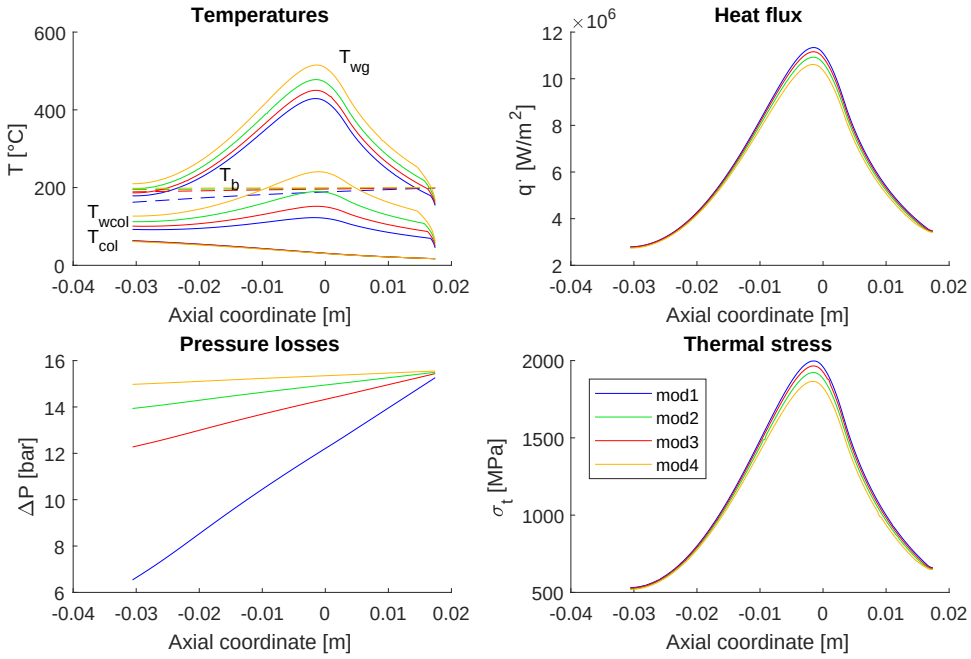

Figure 2.26: Analysis results for different channel geometries

Again, post processing reduced the number of results. In particular, the values excluded from the representation are those related to analyzes in which the convergence has not been optimal due to the continuous passage between the different flow regimes: laminar, transition and turbulent. In any case it is possible to obtain the trend. It should be noted that among the data represented in the various subfigures, there are also ineligible operating configurations due to the high pressure loss which would affect injection into the catalyst. These data, unlike the previous ones, have been obtained without particular problems of convergence. The decision to include the same these data makes it easier to understand trends. (Orientatively by literature the maximum permissible pressure loss in regenerative cooling

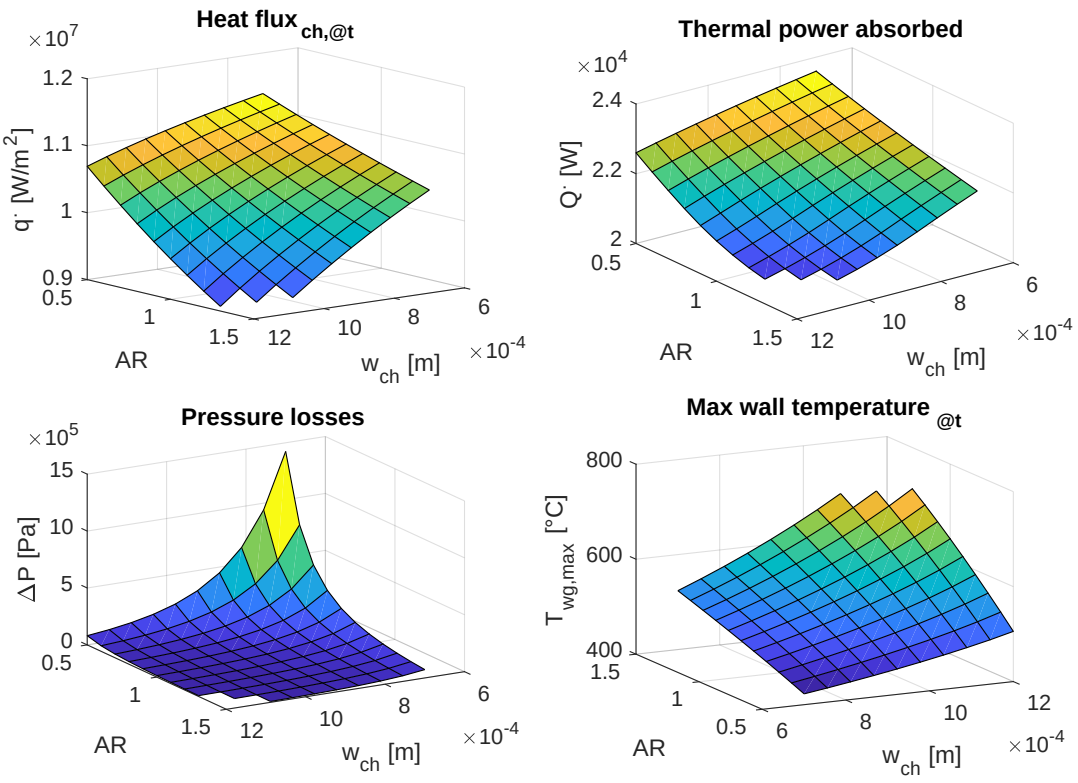

Figure 2.27: Global results from geometry scenario

is between 15-22% P_{in} depending on design requirements).

Observing the figure 2.27 it is immediately noticed that the progressive reduction of the channel section allows to increase the heat flux, the thermal power transferred to the fluid and to reduce the maximum wall temperature $T_{wg,max}$. At the same time there is a more than exponential increase in pressure losses. The relevant aspect on which we want to dwell is that beyond a certain size, the further reduction of the channel does not significantly improve the cooling performance, while the pressure losses worsens substantially, affecting the functioning of the engine or requiring a more performing pressure feeding system.

Other considerations can be deduced from the subfigure 1 of 2.27 and from figure 2.28.

The influence of AR is more consistent for channels with larger w_{ch} amplitudes. Once the width of the channel has been fixed, there is an improvement in the transport properties that increase as the aspect ratio decreases. The influence can be seen to be more than linear. Similar trends have been highlighted in literature[22]. As far as the dependence with w_{ch} is concerned, it is understood that the maximum variation in cooling performance is obtained

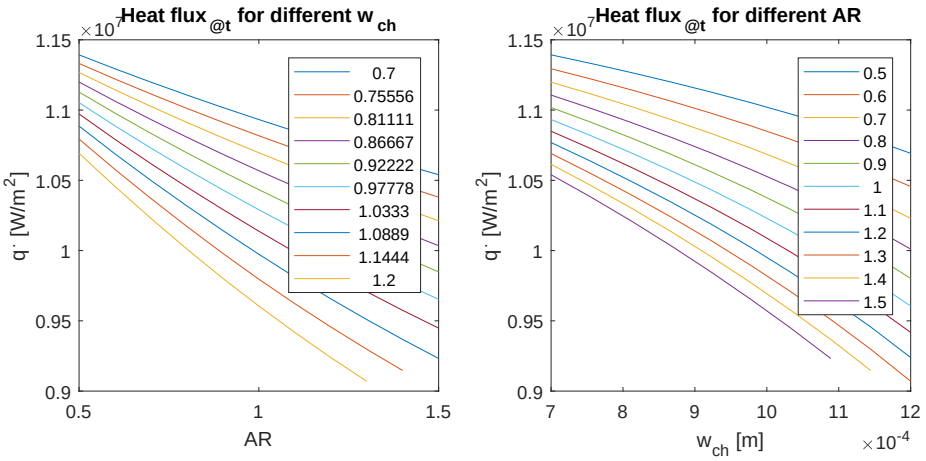

Figure 2.28: Dependencies for $\mathcal{AR}$ and w_{ch}

by high aspect ratios. Specifically, fixed the $\mathcal{AR}$ it is observed that the greater convenience, in terms of transport, is obtained by varying w_{ch} in the part of the field in which it is greater $(1 - 1.2\,[\mathrm{mm}])$. These observations are closely connected with the geometry of the channel responsible for the heat exchange. An analytical expression has been sought which summarized all the exchange on the coolant side with the aim of finding the maximum, but it is very complicated, non-linear with non constant coefficients. Therefore, the numerical approach is the best and the only chance to evaluate the optimum. In figure 2.29a the isolines of the flux and hydraulic diameter have been superimposed with the aim of summarizing the previous observations and having a more global vision.
At the same hydraulic diameter, the thermal flux is maximized for higher AR and lower w_{ch}. From the comparison of the subfigure 2.29a with that 2.29b it is understood that exists a portion of the field in which there is an optimum heat flux value and pressure losses. The last assessment that can be derived from this scenario is the actual existence of a hydraulic diameter or optimal geometry, that allows a good compromise between cooling performance and pressure losses. The identification is always numeric and it is not possible to generalize the result for other operating configurations.

2.5.5 Final motor configuration

The geometries studied are essentially 2, the configuration for axial combustion and the one for swirl combustion.
Let us first consider the axial configuration with conical divergent represented in figure 2.6.

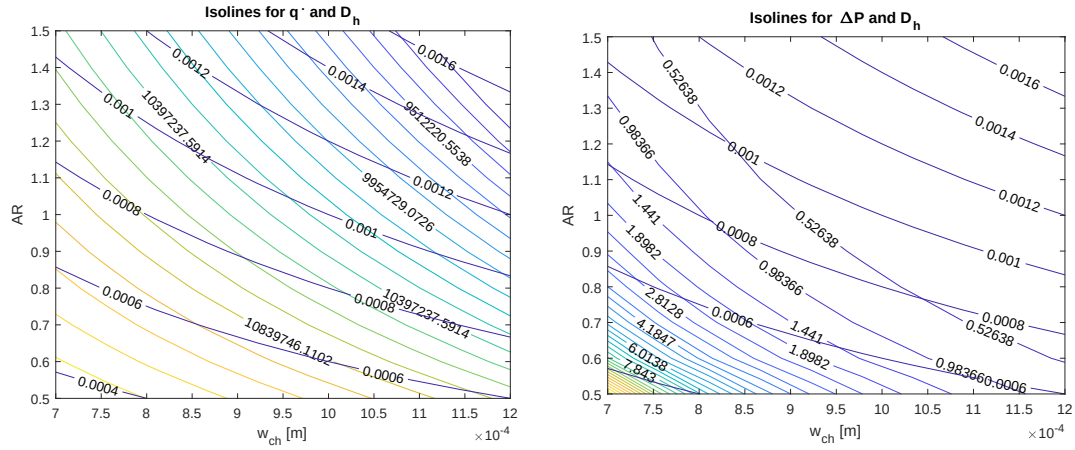

(a) Heat flux and the hydraulic diameter

(b) Pressure losses and the hydraulic diameter

Figure 2.29: Isolines for different properties in channel scenario

In this first configuration has been used stainless steel AISI630 which has properties similar to the material used in $3D$ printing, stainless steel CL20ES. As regard the channel's geometry is the same depicted in figure 2.12 and the number used is 37.
The choice of this number is strictly linked to the results obtained and to the additional geometric constraints imposed. Specifically, this number of channels allows to obtain a good result in terms of cooling/loss of pressure and to create wells inside the case, for the installation of thermocouples. The analysis has provided the follow result resumed in table 2.8.

	$T_{wall,max}$ [°C]	ΔT_{col} [°C]	$T_{col,out}$ [°C]	Q_{tot} [kW]	ΔP [bar]
Axial flow	508.71	44.5	61.5	22.479	2.01

Table 2.8: Result data for axial configuration

The behavior of the gas in the conduit, as said previously, has been described with the isoentropic relations of gasdynamics with the hypothesis that the area is the only agent forcing.

To note that $T_{wa} = T_g$.
From 2.31 figure it's possible to understand several information about fluid and wall temperature. As in literature, the most stressed area is the throat where they are registered highest wall temperature. The second sub figure shows the temperature trends of the coolant and the wall, in a scale that allows to appreciate easily the details. Specifically, it can be observed

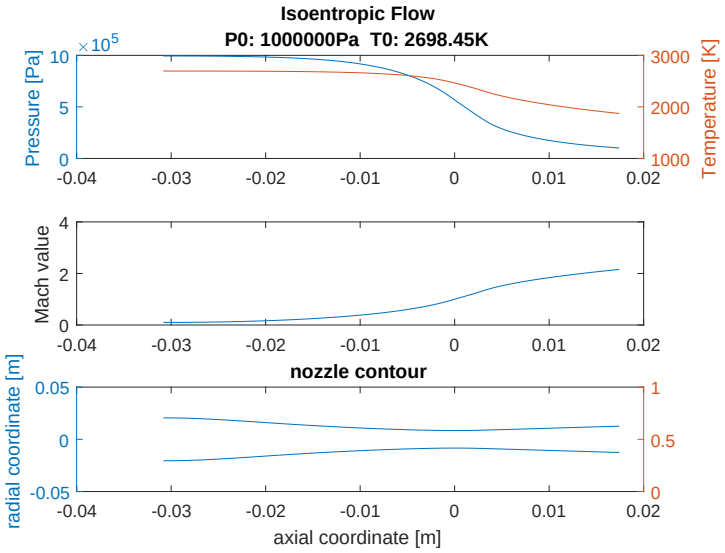

Figure 2.30: Pressure, temperature and Mach number in nozzle (AISI630-Axial)

that the temperature of the coolant side wall ($T_{wc} = T_{wcol}$) is always kept sufficiently far from the boiling temperature at that pressure according to some consideration set out in section 2.4.4.

From the figure 2.32 it is observed that the thermal stresses are surely the most intense ones, those relating to the pressure are in fact only partially visible and would require a further enlargement of the scale. This first sub figure shows that the values reached in the throat area are particularly high and exceed the σ_{UTS} at that temperature. It should be added, that the relation used for the evaluation refers to the elastic field only, for small displacements and for a structure that is substantially constrained in its form. In the project the nozzle is left free to expand so part of the stress is reduced even if is not possible to quantify with analytic formula. However, the value obtained can still be useful for further consideration on the liner's thickness. As regard pressure losses, according to channel's geometry, maximum losses are located near the throat where heat flux is higher (second sub figure) and an higher convective coefficient is required.

For sake of completeness and exclusively for this configuration are reported all the other results obtained, useful for subsequent reflections.

Now let's move on to the swirl configuration.

For this nozzle, as for the previous, are reached the same final Mach, pressure and temperature, even if the evolution in the duct is different due to another area law. The shape consid-

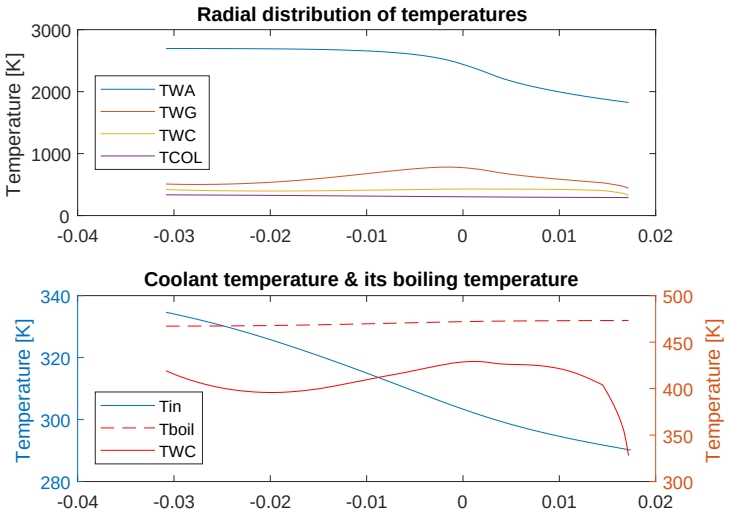

Figure 2.31: Temperatures in nozzle (AISI630-Axial)

ered for this nozzle is the follow depicted in figure 2.37 and the angle α described in figure 2.5 has been set equal to $75[°]$.

About channel's geometry has been used the same as for the axial. This configuration has provided the follow numerical result resumed in table 2.9.

	$T_{wall,max}$ [°C]	ΔT_{col} [°C]	$T_{col,out}$ [°C]	Q_{tot} [kW]	ΔP [bar]
Swirl flow	508.72	33.56	50.56	16.949	1.40

Table 2.9: Result data for swirl configuration

Immediately, by comparing last table with 2.8, it's possible to note that the swirl configuration, although having the same channel geometry (i.e. equal AR & w_{ch} compared to the axial length), leads to a slightly higher wall temperature, allows to reduce pressure losses and limits the heat absorbed by the gas. As regard as the wall temperature is probably affected by approximation while pressure losses and total heat absorber are related. The reduction of the nozzle length, although the geometry is more articulated, has also led to the reduction of the path of the fluid in the channel, limiting both the losses and the absorption of heat. Overall, this configuration seems to be better than the axial because it allows to reduce the power of the pumping/feeding system and at the same time allows to keep the gas warmer. However, as previously anticipated, the *Bartz* equation used is not suitable for describing

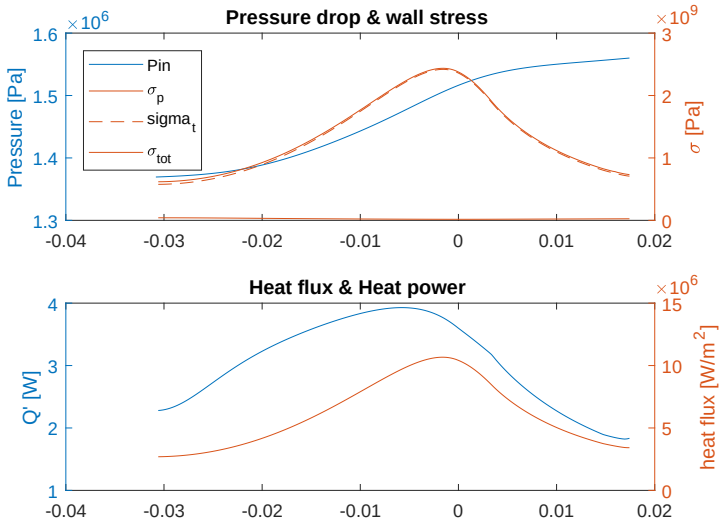

Figure 2.32: Stress, pressure losses and heat transfer (AISI630-Axial)

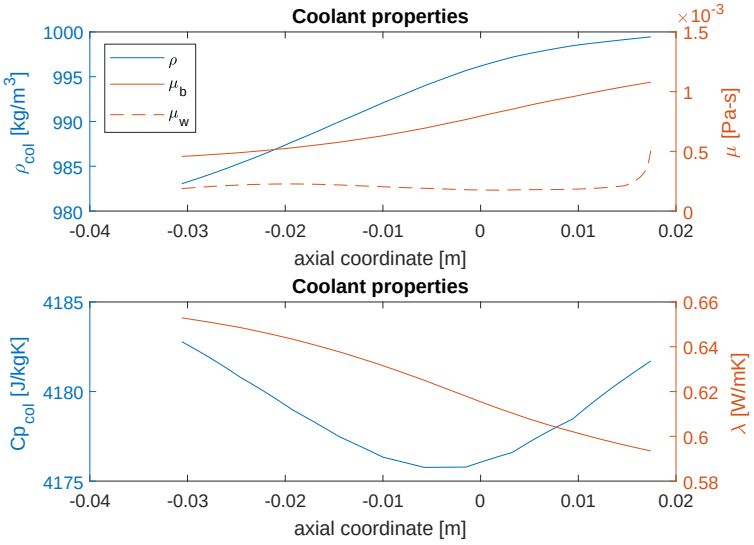

Figure 2.33: Coolant properties for (AISI630-Axial)

swirl flows, although for now it is the best approximation available. In any case, experimental and numerical observations show that the convective coefficient for swirl flows is greater than the axial one, therefore the previous results must be considered as indicative. As for the axial case are given 2 plots with main results (figure 2.38 & 2.39).

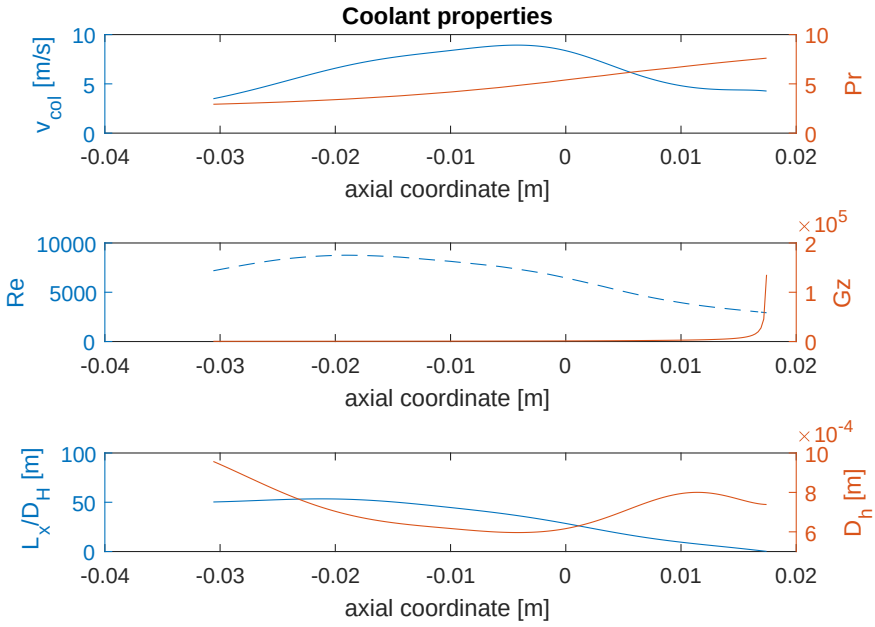

Figure 2.34: Coolant properties and some dimensionless group (AISI630-Axial)

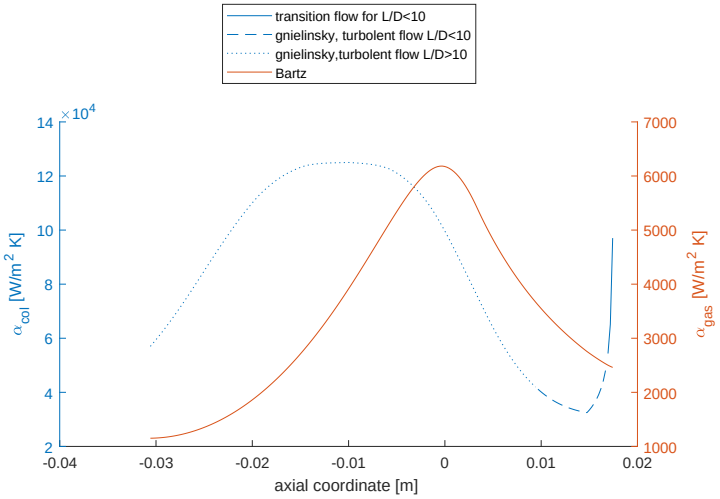

Figure 2.35: Convective coefficients α_{col} (AISI630-Axial)

2.5.6 Final considerations and observations

Globally, the algorithm has good stability and rapid convergence. However, we want to highlight some aspects that emerged in the various scenarios and analyzes.

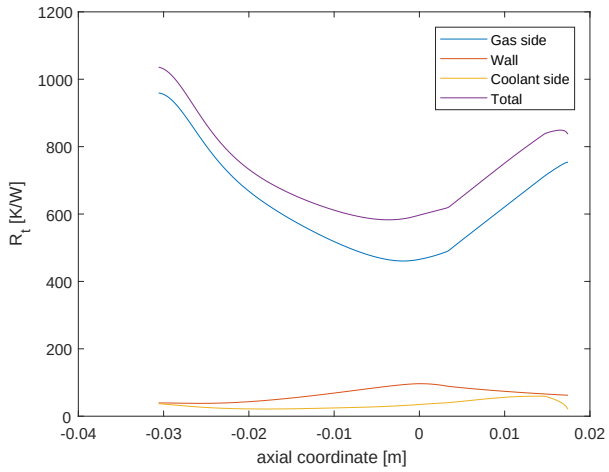

Figure 2.36: Thermal resistances R_{col}, R_{wall}, R_g (AISI630-Axial)

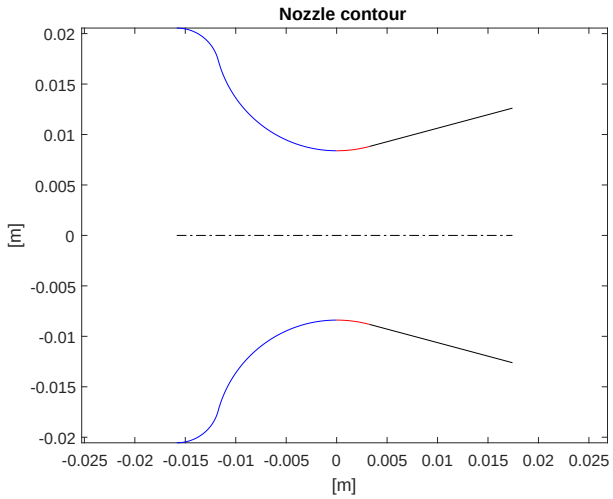

Figure 2.37: Motor geometry (AISI630-Swirl)

First of all, it has been observed that the presence of the thin carbon layer has a significant influence on the heat flux. Although the thickness is minimal, the average conductivity of the soot is very low, indicatively $0.07[W/mK]$, so its thermal resistance is high. After some initial analyzes, it has been decided to exclude the presence of soot because the perturbation that it generated on the results was marked to the point to provide values not compatible with the ranges highlighted in literature [2].
Another aspect that emerged from the analysis concerns the slowing of convergence when

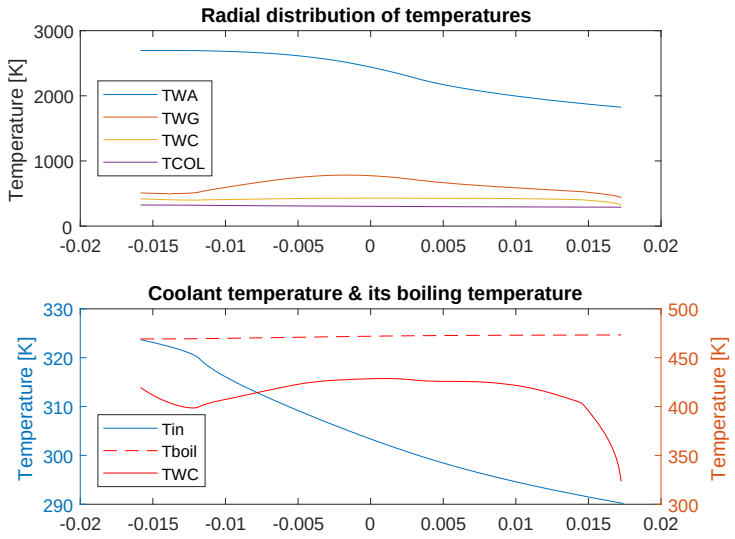

Figure 2.38: Temperature in nozzle (AISI630-Swirl)

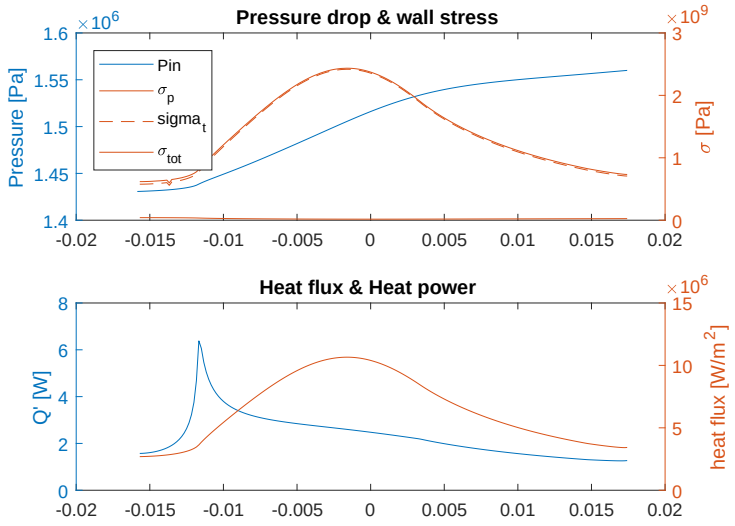

Figure 2.39: Stress, pressure losses and heat transfer (AISI630-Swirl)

the coolant evolves passing from the laminar regime up to the turbulent one. The equation 2.49 turned out to be a non-optimal interpolation between the fields, generating discontinuities that in turn propagated on the other variables. Since the laminar regime remains of little interest for these applications, due to the reduced transport properties, it is sufficient

to make sure to work outside.
Among the various considerations that emerged from the theoretical analysis of the exchange phenomenon, particularly relevant is the development of the thermal and hydraulic boundary layer. In particular, the nature of the phenomenon is such that along the axial coordinate there is a condition of thermal flux and wall temperature profile always variable, moreover, in configurations with variable geometry channels, also the section continues to change. It follows that due to the continuous variability of the geometry and the boundary conditions, a fully developed boundary layer condition is never achieved. Basically it is as if the working point was always inside the entry region (see figures 2.13) and 2.14) and this affects the convective coefficient. It is worth pointing out that the empirical equations used, unless otherwise specified, are valid only for fully developed profiles. It follows that their use has inevitably introduced errors in the calculation of the heat exchange. Although we are aware of this and the empirical equations described in the 2.4.5 section are currently the best approximation for this type of approach. From the subfigure 3 of figure 2.34 it is observed that the ratio $\frac{L_x}{D_h}$ never reaches values higher than 50, rather it is noted to stabilize beyond a certain coordinate. This is due to the variability of $D_h(x)$.
Remaining always on the topic empirical equations, we want to highlight a phenomenon observed in numerical analyzes where the conditions allowed to use Sieder and Tate (2.50). Specifically, it has been found that Sieder and Tate tended to develop a much more intense temperature gradient between wall and coolant bulk than Gnielinsky. This consequence is strongly linked to the $\frac{\mu_{bulk}}{\mu_w}$ group. In particular, by fixing the geometry and the initial temperature condition (T_{wcol}) the properties of the bulk and the Re and Pr groups are also blocked. Therefore, to satisfy a given heat flux, the only degree of freedom of the equation is T_{wcol}. Further analyzes highlight that high $\dot{q}$ generate high differences between $T_{wcol} - T_{col}$ that under certain conditions bring $T_{wcol} > T_b$ to that pressure, reducing μ_w to a good order of magnitude. This effect strongly disturbs the convergence determining a continuous transition condition at the turn of the boiling temperature. To avoid this phenomenon it is essential to change operating fluid and/or geometry. In any case, remembering the hypothesis[20] for the equation 2.50, the use of Sieder and Tate is not recommended for pure water and in any case should be avoided when $T_{wcol} \geq T_b$. For this reason Gnielinsky has been considered more suitable.
Let us now turn to the benefits introduced by the modulation of the channel geometry. The main advantage of variable geometry is to achieve a good compromise between cooling performance and pressure losses. This can be easily understood by comparing the figures 2.26

and 2.32 from which it is noted that the modulation allows to adapt the speed of the coolant in relation to the needs without significantly reducing the convective coefficient. The mathematical analysis and the numerical results confirm that $\Delta P \propto v^2$ while $\alpha_{col} \propto v^{\varpi}$ with $\varpi < 2$.

Remaining further on the modulation of geometry and speed, it is also important to highlight the behavior of the Re number. From the point of view of heat transport and in order to minimize the coolant resistance, among the various options, we are interested in maximizing the Re because $\alpha_{col} \propto Re^{\varsigma}$ with $\varsigma \in [0.5.1]$. Recalling the definition of Re, it is clear that set the working temperature and pressure, the only quantities on which we can act are $\bar{v}$ and D_h. Actually, as noted above, $\bar{v}$ depends on the geometry too. As seen from figure 2.34, hydraulic diameter increases are always accompanied by a reduction in fluid velocity, so it is difficult to have high variations for Re number , especially limiting losses. The only way to increase Re without changing the channel geometry is to reduce the number of channels even if the uniformity of the temperature along the nozzle wall is reduced too.

Further analysis of the channel's geometry concerns the aspect ratio. From the scenario related to the different channel geometries it has emerged that the configurations that allow to obtain higher performances in terms of heat transport are those with high *AR*. This is justified by the increase in the surface of the channel in contact with the fluid. Actually, it is good to specify that the use of high *AR* is mostly convenient if the case of the nozzle is highly conductive. In any case, the choice of *AR* is always a compromise with the other geometric constraints.

Let us now turn to a global evaluation of the trends of physical quantities considered for variations in the thickness t_{cs}. The analyzes show that a reduction in the wall thickness allows, with the same D_h and metal for the case, to increase the convective coefficient on the coolant side, to reduce $T_{wcol} - T_{col}$ and consequently also thermal stress. Despite the nozzle's and the channel's geometry remaining the same, it's observed an increase of Re. This depends on the variation of the thermodynamic properties of the fluid. From a comparison, it emerges that the configuration with minor t_{cs} allows to exchange more heat and, at the same axial coordinate, the coolant is warmer. It is the temperature that raises the number of Re and lowers Pr. In any case, the speed with which Re grows is greater than that with which Pr decreases, therefore altogether α_{col} is more high. A further effect associated with the reduction of t_{cs} is the slight increase of α_g due to wall temperature dependence.

Finally, the numerous analyzes allowed to give a concrete answer to the expectations related to the thermal resistances previously mentioned in 2.4.5. Observing the figure 2.36 it is ob-

served that the gas side thermal resistance is actually the highest, then downwards there is the wall resistance and finally the parallel on coolant side. In order to reduce the thermal gradient on the wall, the thermal resistance should be limited. Possible operation by limiting the thickness and / or modifying the metal of the case. The first operation is certainly the most feasible since t_{cs} has been strongly oversized for the current operational pressure, the second option is limited by the chemical compatibility with the H_2O_2. The gas side resistance is substantially constrained by the geometry and the operating quantities, therefore it is not possible to modify it. Finally the coolant side resistance is observed to depend strongly with the number of Re and less with Pr. Basically the influences are the same as described in all the previous observations.

3
The design process

This chapter will cover all the phases that led to the sizing of the components and the definition of the final prototype. The entire design process has been iteratively carried out, sometimes by progressively adjusting the previous designs and adapting them to new needs, others revising the project completely. In any case, this design phase has allowed us to get in touch with the concrete reality and to clash with the limits of the mechanical processes, materials and available resources. Therefore, the entire design phase has required to interface with many aspects of engineering and more. The final configuration proposed is nothing more than the summary of all this activity.

3.1 Design specifications

3.1.1 Specifications

The operating specifications of the prototype to be implemented have already been presented in the 2.1.1 section. In addition to these requirements, further specifications have been added to the project that strictly relate to construction and assembly. In particular, being a prototype made with non-conventional mechanical processes, it has been requested to:

- ensure complete inspection of the cooling channels inlets and outlets to verify they are not obstructed
- allow the nozzle to be connected to an already existing combustion chamber

- to assemble quickly and easily the various components with laboratory equipment currently available (torque wrenches, wrenches ...)
- allow the installation of the same nozzle with different distribution systems
- ensure the provision of suitable wells for inserting thermocouples with a diameter of 0.5 [mm]
- ensure the chemical and thermal compatibility of materials considering that only the tests will use water as a coolant

From the previous requests it is assumed that the distribution systems can't be integrated with the nozzle but must be made separately and connected to the prototype with some kind of connection that allows to support the operating pressure and to follow the nozzle with thermal dilatations. The second request highlights the need to integrate the current project with the combustion chamber of another project and therefore with different geometries. The need to be able to easily assemble the various components suggests to limit the number of parts, preferring conventional bolted connections where possible and to arrange them in such a way as to guarantee their closure with the available equipment. Finally, the integration of the thermocouple wells must take place at the planning level, trying to disturb the cooling system as little as possible.

3.1.2 Material choice

Regarding the choice of materials, different solutions have been considered trying to satisfy the various design requirements. Regarding the nozzle, the choice of material was made assuming that the prototype test is as close as possible to the final one that will actually operate with H_2O_2 as a coolant. As regards the other components, such as gaskets, the driver that determined the choice of the material is the thermal resistance. Since the prototype that has to be designed is made up of many more parts than the flying one and taking into account that in the precautionary test phase will be used H_2O for cooling, the choice to use gaskets not compatible with H_2O_2 not in no way affects the final design. It should be noted that in the flight model the fluid distribution systems will be integral with the nozzle and printed with it (see figure 5.1). Furthermore, the nozzle will be connected directly to the combustion chamber without the need to use gaskets. For this reason it's possible to understand that the role of the gaskets is fundamental only in the test prototype and this justifies the decision to attribute greater importance to thermal compatibility. As regards the distribution and

connection systems which are indispensable in the test model, it has been decided to use a material similar to that of the nozzle, so as to guarantee the same thermal expansion.
From the previous chapter, in particular from the 2.5 section, important results emerged in relation to the various types of material. The analyzes suggest the use of high conductivity materials such as aluminum or copper, although incompatibility is known, especially for copper. The only series of aluminum for which full compatibility is guaranteed (Class 1) is the 1000 series which however has insufficient mechanical properties for application in this project. It is clear from the literature [18] that even some low-copper 5000 aluminum series are Class 1, while most are Class 2 and 3 therefore not suitable for operating temperatures even if the duration of the contact is very inferior to 4 hours. The 2000 series is strongly discouraged (Class 4). As for the steels there is none that guarantees compatibility Class 1, the best option involves the use of stainless steel even if there is no agreement between the various literature on the maximum allowable temperatures for brief typical contacts of the intended conditions of use. Inconel 718 is also not fully compatible with the H_2O_2.
Therefore, taking into account the previous information, the results emerged from the analyzes in section 2.5, the experience of the laboratory staff and the various mechanical properties of the metals in temperature, has been decided to try to use steel stainless. It should be emphasized that in the laboratory, applications similar to the project under consideration, have never been studied, therefore the experience is limited to the success of the numerous previous experiences. Further hypotheses have been examined regarding the use of more suitable materials, such as copper, by realizing suitable coatings in the channels, but due to the complexity they have been discarded. Specifically, the use of compatible coatings involves the deposition of a material on the surfaces of interest by means of different techniques depending on the substance. The main problems concern the control of the coating thickness, the thermal conductivity and its thermal expansion. The first problem concerns not only the effective measurement of the coating thickness but also its uniformity, the second the guarantee that the coating dilates like the metal and does not fracture exposing the underlying surface.

3.2 Construction process with 3D metal printing

The rapid prototyping process 3D metal printing has made it possible to overturn the mechanical processes, making it possible to obtain products with complexities and geometries never obtained before. Although this technology has been available for decades has not yet

reached its peak, the future will certainly introduce further and numerous innovations. Currently the production process has reached repeatability standards and precision that allow to treat the product as a near-net-shape/net-shape and for this reason, it has been reclassified as addictive manufacturing. The 3D printing initially conceived for the plastics has been studied and applied also for some metallic materials allowing a rapid diffusion in the industrial field. Starting from 2016, this technology began to become more and more widespread also in the aerospace sector thanks to its peculiarities, so much so that the *FAA* started to update the current regulations for use.

From the production point of view, the 3D metal printing uses the laser to weld the various metal layers deposited by a special distributor. Laser control is performed using numerically controlled machines in accordance with the *CAD* project. The quality of the product depends strongly on the size of the metal powder grain and the laser used in the process. Particularly relevant parameters are laser beam size and power. The machines available today allow the creation of objects of different sizes, even if they are still reduced compared to the components that can be obtained with conventional machining.

Despite the great versatility of technology and the high complexity of achievable geometries, there are technological limits that must be considered in the design process. First of all, the component to be created must be rigidly and intimately connected to a cooled base/plate with the dual purpose of ensuring initial blocking-calibration and to dissipate the high heat generated during laser welding. This condition implies that, once the process has been completed, during the removal phase which generally occurs by cutting the connection, it is possible to modify dimensions, finishes and geometric tolerances of the piece. During the design phase, this aspect must be taken into consideration by adding any overthickness and possibly evaluated subsequent machining operations to obtain the desired geometrical/dimensional tolerances and/or finishes. A technological limit, on the other hand, concerns the construction of certain geometries. In particular, the realization of surfaces, with inclinations orientatively lower than 45 [°] with respect to the plane of the support plate, require specific supports which, once again, during the removal could modify the finish and/or geometric/dimensional tolerances of the component. During the design phase, it is necessary to carefully evaluate the possible arrangement of the supports and the over thicknesses. In general it is observed that this measure becomes particularly indispensable for medium-large size objects even if it is good to specify that due to the great variability of the geometries, the evaluations must be done from time to time.

Another technological limit to be considered concerns the emptying of the cavities. One

of the most interesting properties of the 3D metal printing is that of realizing solid, ducts, channels and cavities in thin/thick walls without welding. At the end of the manufacturing process and before the separation with the support plate, the unused powder is removed. The removal takes place through different techniques depending on the fragility and complexity of the component, in any case, always in the design phase, appropriate openings must be provided to facilitate unloading of unused material.

3.3 Final test configuration

3.3.1 Nozzle configuration

The design of the nozzle, like the rest of the flanges, has required a global vision of the project to meet all the previous requirements. Geometric modifications of the nozzle have influenced the flanges and vice versa. According to previous evaluations, the nozzle material is stainless steel CL20ES.
The final configuration is as shown in the figures 3.1 and 3.2.

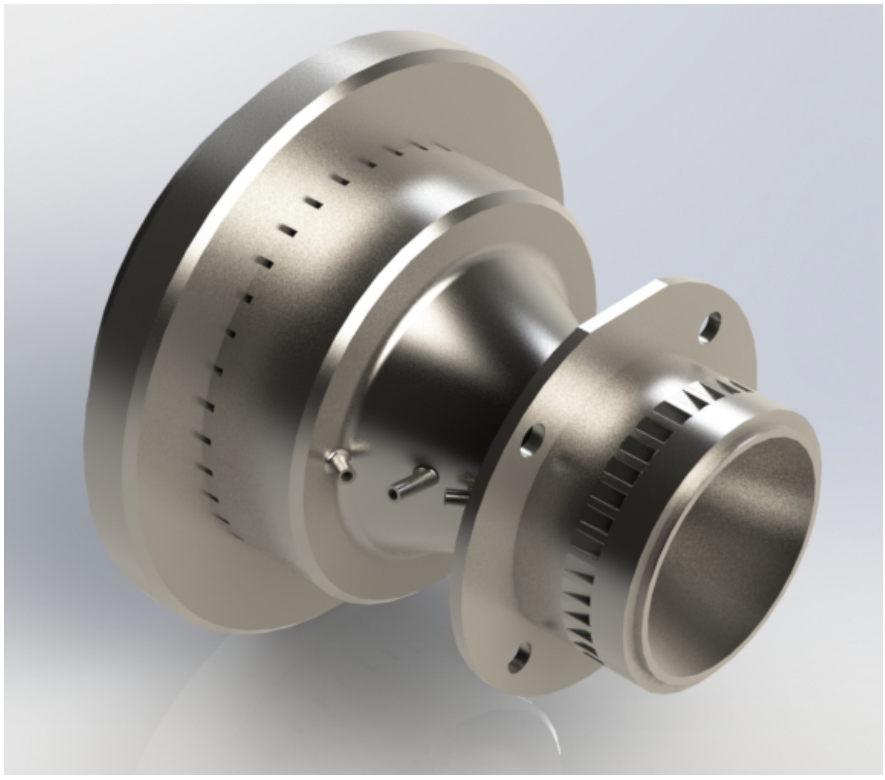

Figure 3.1: Final nozzle configuration

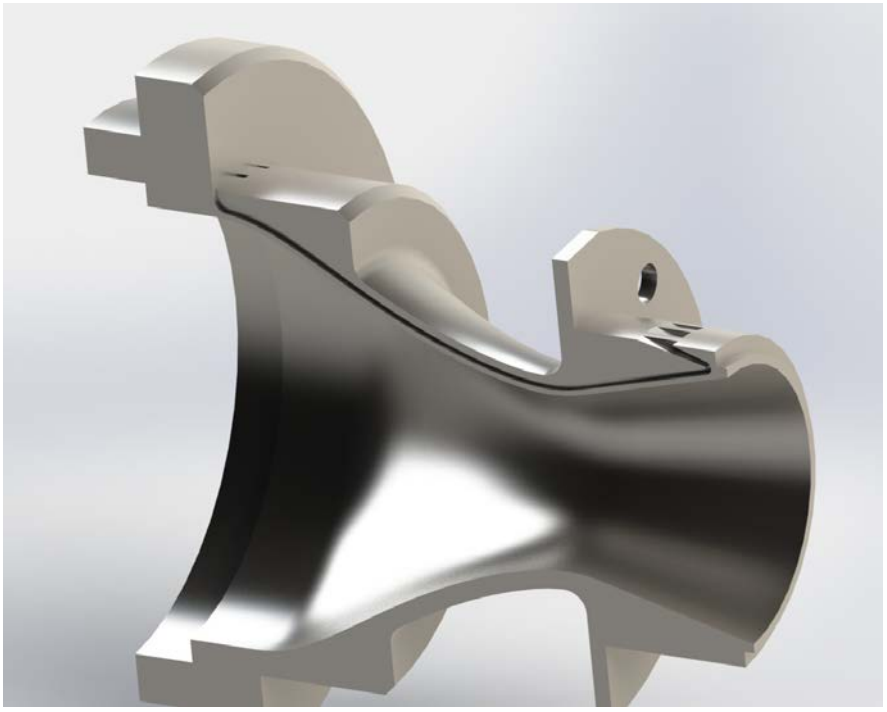

Figure 3.2: A channel inside the nozzle wall

The model consists in 37 variable geometry channels described in figure 2.11. To allow the inspection of the various channels, the distribution system has been removed. One volute has been obtained on the connecting flange and the other on the closing flange, placed at the outlet of the divergent. The integration of the flanges and, in particular, of the hydraulic seals with o-rings, required a substantial change in the channel's geometry with respect to the condition initially simulated in the predictive algorithm.

Specifically, in the output section a fitting has been introduced that allows the coolant to be diverted by 90 [°] (figure 3.3), while at the inlet, the impossibility of arranging differently the seats of the o-rings has required the introduction of an inclined feeding channel that connects to the main one (figure 3.4).

The assembly simplification requirement required a dedicated study of the assembly sequence and the components to be used. For reasons of practicality and safety the flanges, as mentioned before, have been preferred to the clamps, although they have introduced further geometric constraints to guarantee assembly. Specifically, the nozzle geometry has suggested a main direction for the assembly sequence which involves inserting all the components along its axis of symmetry, from the divergent towards the convergent. To facilitate the seating of the flanges and o-rings, cylindrical shoulders supports and mechanical stops have been made.

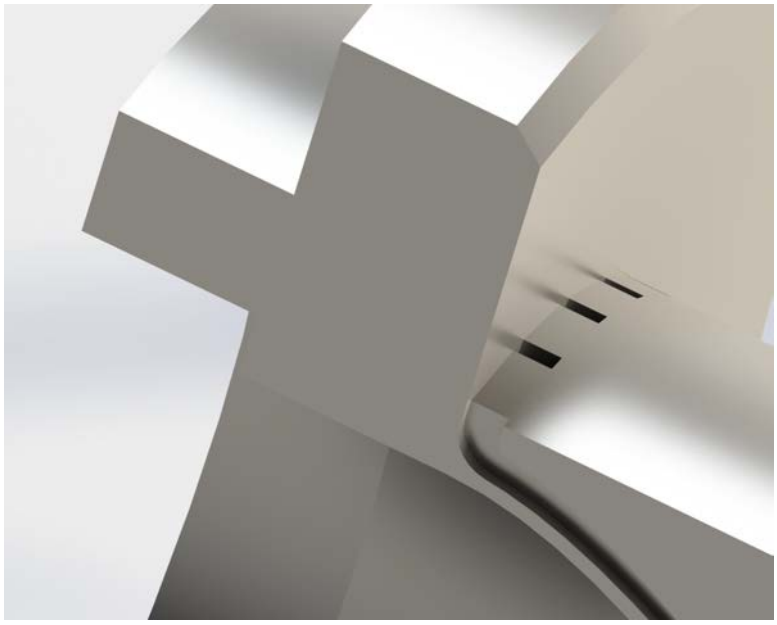

Figure 3.3: Output fitting

Obviously the introduction of these geometries has changed the previous projects to the current one, further complicating the management of the inlet and outlet of the channels. As for the thermocouples, the housing of the wells has been made on one side of the nozzle (see figure 3.1). The wells were obtained inside the channel separation wall and the arrangement was chosen taking into consideration the graphs obtained in the 2.5 section. Finally, recalling the limits of the 3D printing technology described above, the areas in contact with the plate have been added with a overthickness, as well as all the surfaces that must be coupled with the flanges in order to guarantee, where needed, a better coplanarity, cylindricity and surface finish, essential especially for o-rings. These finishing operations are expected to be done with machining.
Some structural checks follow.
The design of the nozzle has also provided for the dedicated structural checks carried out with the package *Patran* ® / *Nastran*®. The analyzes investigated the nozzle behavior under pseudo-operative conditions, i.e. with all pressure loads, acting forces and assuming it all isothermal at maximum temperature. It is good to specify that *Nastran*® allows to perform thermal analysis, however it does not allow to evaluate the actual heat flow between the gas and coolant side because it is a mainly structural solver, while the problem would require a fluid-dynamic/ thermal /structural analysis. The main boundary conditions that the soft-

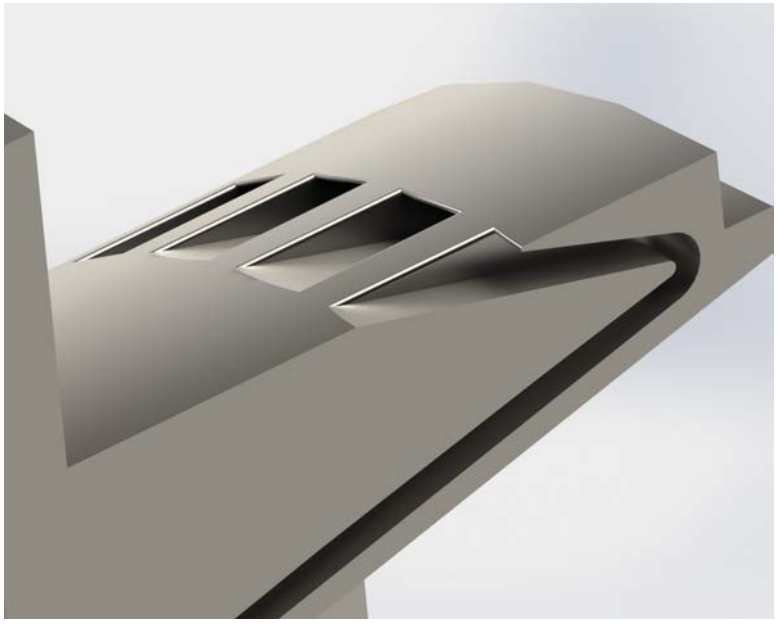

Figure 3.4: Inlet feeding channel

ware is able to handle are temperatures,heat flows and convective coefficients. All these conditions can be described by spatial fields so it would be possible to import the values obtained from the MATLAB® analyzes and insert them in the *FEM*. However, the values obtained in the analyzes are the result of numerous simplifications, including mono-dimensionality. For this reason, their use would considerably spoil the solutions obtained with the *FEM* solver. At present, the knowledge and experience in the *FEM* packages such as Ansys® are not sufficient to simulate the whole complex phenomenon desired, therefore we limit ourselves to the following structural analysis. The hypothesis of working with an isothermal nozzle at maximum temperature strongly underestimates the stress on the liner wall between the channel side and the gas side, but also allows to estimate the other stresses in favor of safety. The low conductivity of the steel generates intense temperature gradients therefore, far from the liner wall, the temperatures are considerably lower than the predictions of considering the isothermal nozzle at maximum temperature.

The structural analysis carried out is a static linear (*Sol* 101) in which all the constraint conditions foreseen by the assembly and the pressure loads characteristic of the operating phase have been applied. For simplicity and in favor of safety, it was assumed to apply a constant pressure when the axial coordinate varies and with a module equal to the maximum expected value. The analysis has been carried out at the maximum temperature foreseen by

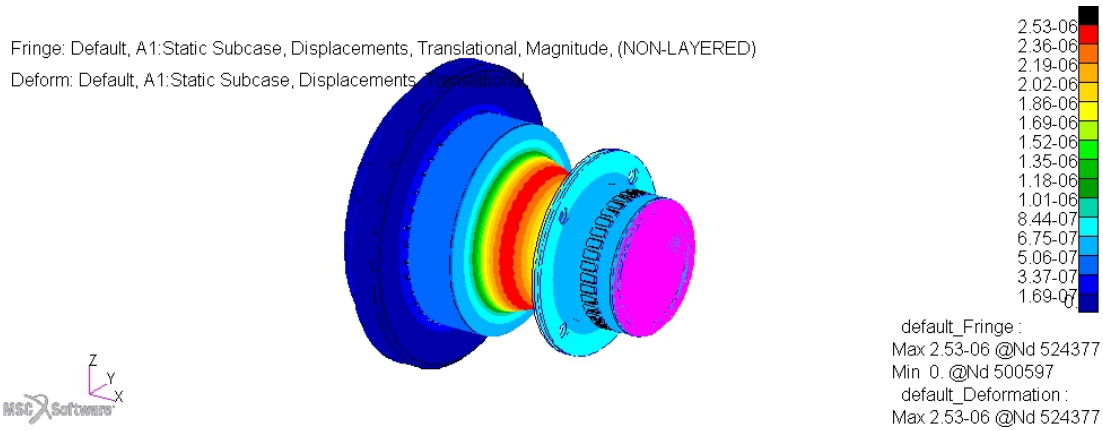

Figure 3.5: Deformations for nozzle at operating condition - 1

the analysis of the 2.5.5 section, taking from the datasheet the properties of the material used at the expected temperature. The average properties of the material used are resumed in the following table 3.1. Interpolations have been made where data are not available.

Material	$\rho[kg/m^3]$	E [GPa]			σ_y [MPa]		
		20[°C]	200[°C]	400 [°C]	20[°C]	200[°C]	300 [°C]
CL20ES	7.8	200	185	170	375	350	300
σ_{UTS} [MPa]		β $[1e^{-6}K^{-1}]$			$\lambda[\frac{W}{mK}]$		
20[°C]	200[°C]	400[°C]	100[°C]	300[°C]	500[°C]	20°C	500°C
650	-	-	10.9	11.1	11.1	15	21

Table 3.1: Physical and mechanical data for CL20ES

In addition to the above mentioned loads, the contribution of the weight of the closing flange connected to the output of the divergent has also been added. The equivalent load modeling was done with a force placed at the flange center of gravity and applied to the nozzle by *MPC* of type *RBE* 2.

As can be seen from the figures 3.5, 3.6, 3.7 the maximum deformations are recorded in the convergent, in the area where the thickness is minimal. In any case, the maximum recorded deformations are negligible, with orders of magnitude equal to $[\mu m]$. The results show that the structure can be considered sufficiently rigid and able to maintain the geometry in operative conditions.

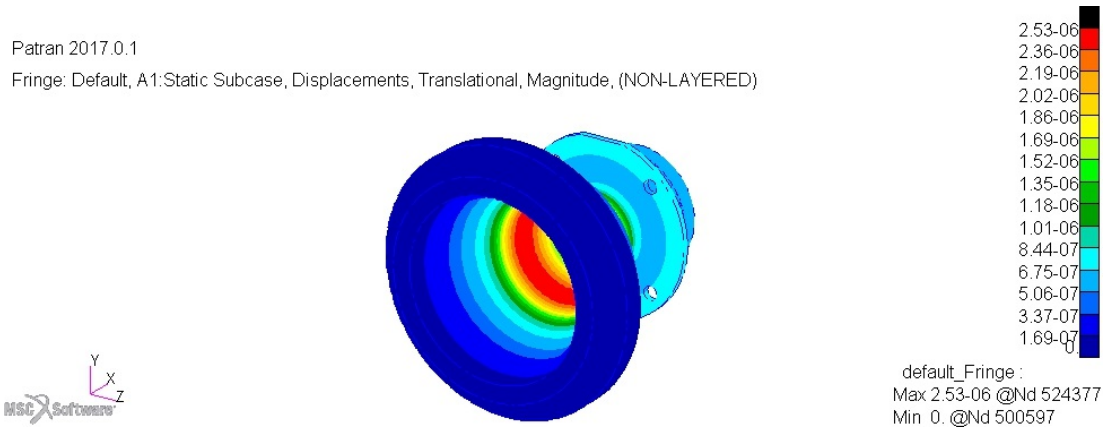

Figure 3.6: Deformations for nozzle at operating contidion - 2

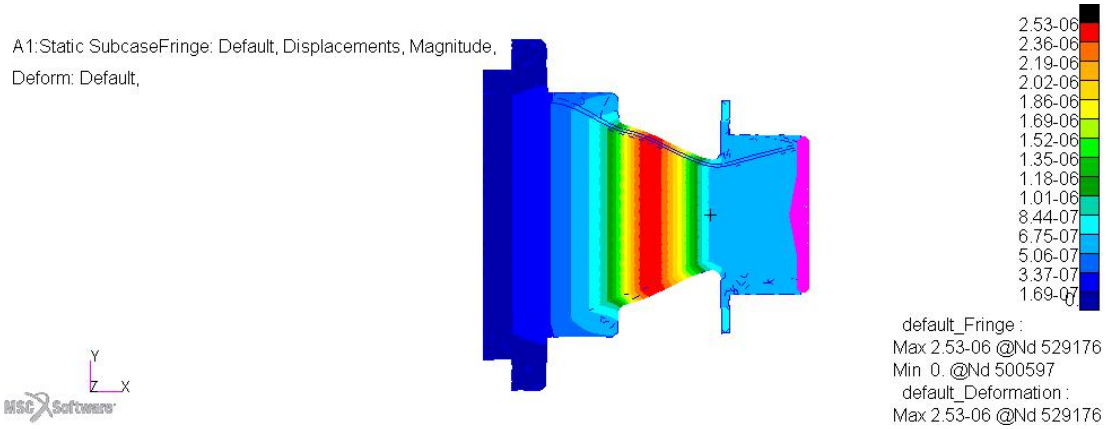

Figure 3.7: Deformations for nozzle at operating condition (section view)

The sectional view of figure 3.7 shows, with a suitable magnification scale, the deformation that affects the convergent area.
Let's move on to the verification of the stress state. The values have been represented with the stress criterion of Von Mises.

The figures 3.8, 3.9 and 3.10 highlight that the area under greater stress is always the convergent where the thickness is minimal. Looking in detail, one notes that the most stressed positions are in correspondence with the channels. This result is in line with expectations. Once again observing the sectional view of figure 3.10, we note that the most stressed area in absolute terms are the upper and lower walls of the channels. In any case, always bearing in mind that thermal gradients have not been considered, the tensions due to all loads are lower than the permissible stresses described in table 3.1, leaving a reasonable margin also for

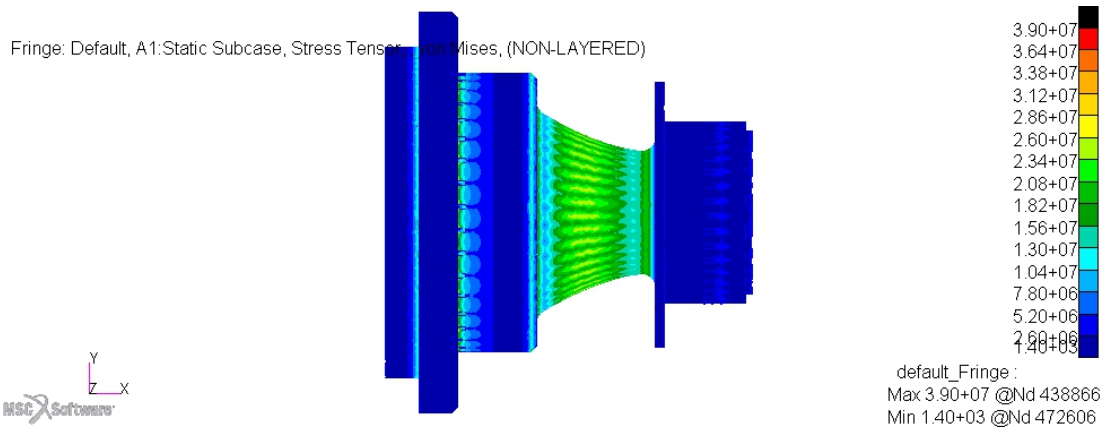

Figure 3.8: Stress tensor for nozzle at operating condition - 1

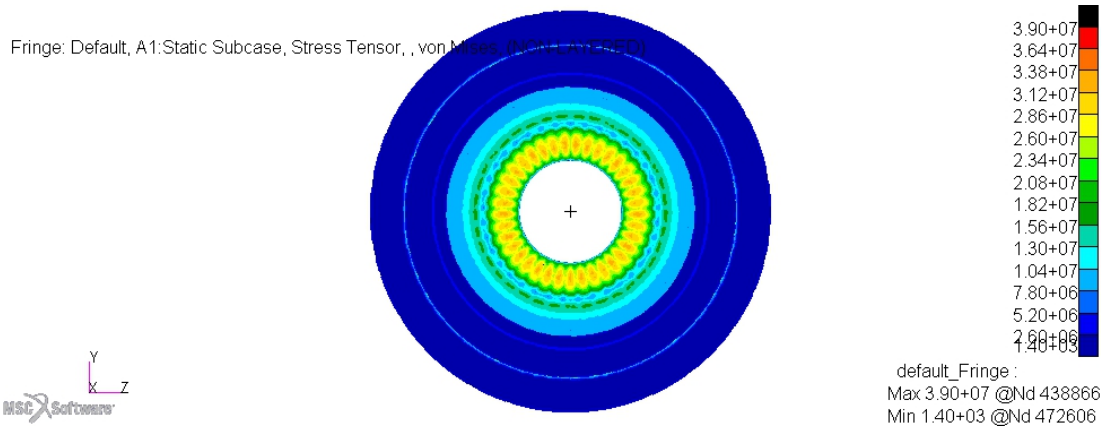

Figure 3.9: Stress tensor for nozzle at operating condition - 2

thermal ones.

3.3.2 Connection flange

The connection flange, like the closing flange, integrates in it the feeding and distribution system, that is a volute to facilitate the channeling of the fluid. The connection flange also allows the nozzle to be connected to the combustion chamber. The preliminary dimensioning of the flanges, and of the relative thicknesses, has been done following the procedures described in appendix 2 (”Rules for bolted flange connection with ring type gasket”) of the *ASME*[5] manual for pressure vessels. The chosen configuration is that of an Integral type flange. The material selected for both flange is stainless steel AISI 630.

In accordance with the diagram in figure 3.11 and the current flange measurements, all

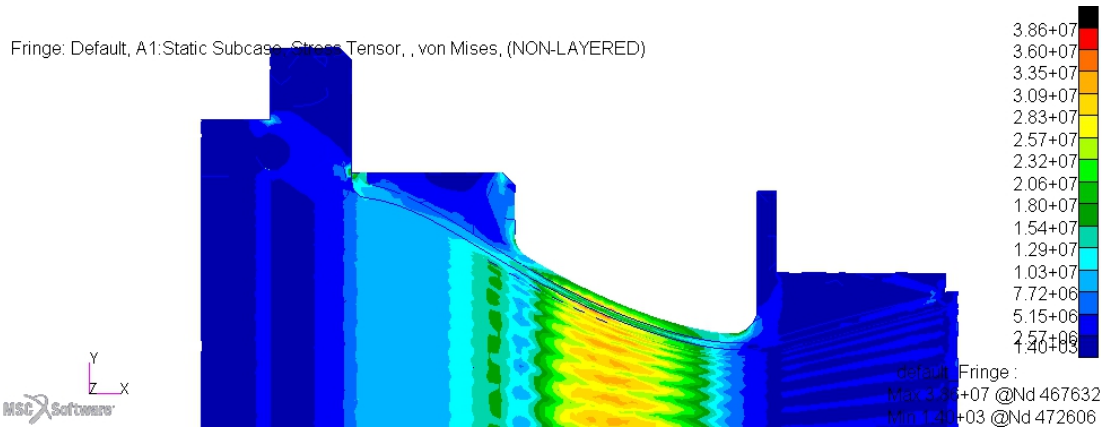

Figure 3.10: Stress tensor for nozzle at operating condition (section view)

stress tests are overcome with ample safety margins. It is worth pointing out that a much less thick flange was sufficient to hold the pressure loads, the preloads due to compression of the graphite packing and tightening moments. The reason that determined the current thickness is once again the housing of the distribution system and the o-ring cavities.

Taking into account that for this flange $g_1 = g_0$,and the ratio $K = A/B$ the F value can be obtained from the figure 2.7 of *ASME* manual and is $F = 0.908920$. For material with Poisson ratio equal to 0.3 the follows equation, as suggested by manual, can be used. The verification procedure can be summarized with the following steps.

$$h_0 = \sqrt{Bg_0} \tag{3.1}$$

$$e = \frac{F}{h_0} \tag{3.2}$$

For the coefficients:

$$T = \frac{k^2(1 + 1.8.55246\log(K)) - 1}{(1.04720 + 1.9448K^2)(K - 1)} \tag{3.3}$$

$$U = \frac{k^2(1 + 1.8.55246\log(K)) - 1}{1.36136(K^2 - 1)(K - 1)} \tag{3.4}$$

$$Y = \frac{1}{K - 1}\left[0.66845 + 5.71690\frac{k^2\log(K)}{K^2 - 1}\right] \tag{3.5}$$

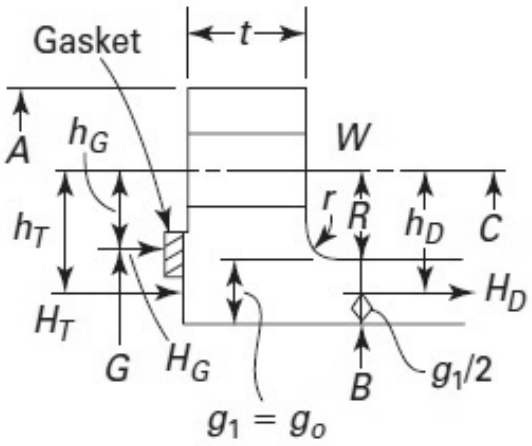

Figure 3.11: Geometric scheme and flange dimensions[5]

$$Z = \frac{K^2 + 1}{K^2 - 1} \tag{3.6}$$

For this kind of flange $\frac{U}{V} h_0 g_0^2$, $L = \frac{te + 1}{T} + \frac{t^3}{d}$ and f value can be evaluated from figure $2 - 7.6$ of *ASME* manual and is equal to $f = 1$. As regards the packing, specific coefficients are available from table $2 - 5.1 \& 2 - 5.2$ of the same manual. For this case $m = 2.5$ and $b_0 = 2.5$ [mm].

$$W_{m1} = 0.785 G^2 P + (2b\pi GmP) \tag{3.7}$$

For bolts spacing has been considered $B_s = \frac{C\pi}{nB}$ and the bolt spacing factor is $B_{sc} = \sqrt{\frac{B_s}{2a+t}}$. For the moments evaluation the following equation can be used.

$$M_0 = B_{sc} W 0.5(C - G) \tag{3.8}$$

Finally for stresses:

$$S_R = \frac{(1.33te + 1)M_0}{(Lt^2 B)} \tag{3.9}$$

$$S_h = \frac{fM_0}{Lg_1^2 B} \tag{3.10}$$

$$S_T = \frac{YM0}{t^2 B} - ZS_R \tag{3.11}$$

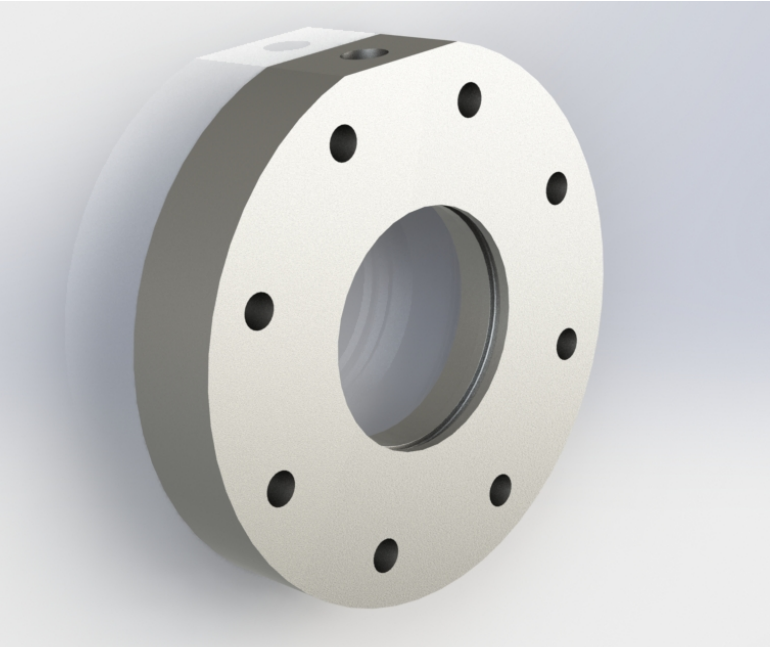

Figure 3.12: Connection flange

The structural verification for the flange is calculated by evaluating the following ratios.

$$S_{Hadm} = \frac{S_H}{1.5\sigma_y} \quad S_{Radm} = \frac{S_R}{\sigma_y} \quad S_{Tadm} = \frac{S_T}{\sigma_y} \tag{3.12}$$

$$S_{HRadm} = \frac{S_H + S_R}{2\sigma_y} \quad S_{HTadm} = \frac{S_H + S_T}{2\sigma_y} \tag{3.13}$$

All quantities must be supplied in the imperial system.
Also the flange, like the nozzle has a certain temperature gradient during operation, even if much less severe. For this reason to hypothesize isotherm at a certain temperature does not involve particular limitations. It is assumed that the flange is made of AISI 630 and operates at a temperature of 150 [° C]. At this temperature the material has a $\sigma_y \approx 500$ [MPa].

The verification is positive if all the coefficients of the equations 3.12 and 3.13 are less than 1. The verification provides the following results.

Given the large safety margins on sizing and considering the simplicity of the component, analyzes with *FEM* can be neglected, even if for completeness they have been carried out equally.

Results of the structural analysis.

P [bar]	A [mm]	B [mm]	C [mm]	G [mm]
20	105	40	85	50
t [mm]	n°bolts	a [mm]	g_0 [mm]	
19.5	8	6	2	

Table 3.2: Input parameters for connecting flange

S_{Hadm}	S_{Radm}	S_{Tadm}	S_{HRadm}	S_{HTadm}
0.2317	0.0133	0.3794	0.1804	0.3635

Table 3.3: Verification factors

It is good to underline that the deformations of figure 3.14 have been represented with an appropriate magnification scale.

Distribution system

The sizing of the distribution system has been made with the aim of keeping the fluid speed inside the volute constant. The equation used for calculating the cross section is the continuity equation described below.

$$A(\theta) = \frac{\dot{m}_{ox}(\theta)}{\rho \bar{v}} \tag{3.14}$$

where θ represents the angle to the plane of the input section. The volute has been evaluated by supposing to divide the incoming flow into two equally distributed flows. The sizing speed has been chosen trying to avoid abrupt variations between the supply channel and the cooling channels and that the dimensions of the volute do not interfere with the hydraulic seals and the bolted connections. For reasons of simplicity in the realization and considering the tools available to the workshop, a volute with a rectangular section with fixed height has been chosen, although the circular one is known to be the optimal one.

Since even the creation of a rectangular volute is not easy without numerical control machines, two configurations have been provided for both flanges, the one with an optimized volute and the simplified one. The second configuration foresees that the volute has a constant section, $A(\theta) = cost$. From the flange section view in figure 3.13 it is possible to see the o-ring slots, the scroll and the feeding system that will be connected to the 1/8 "threaded

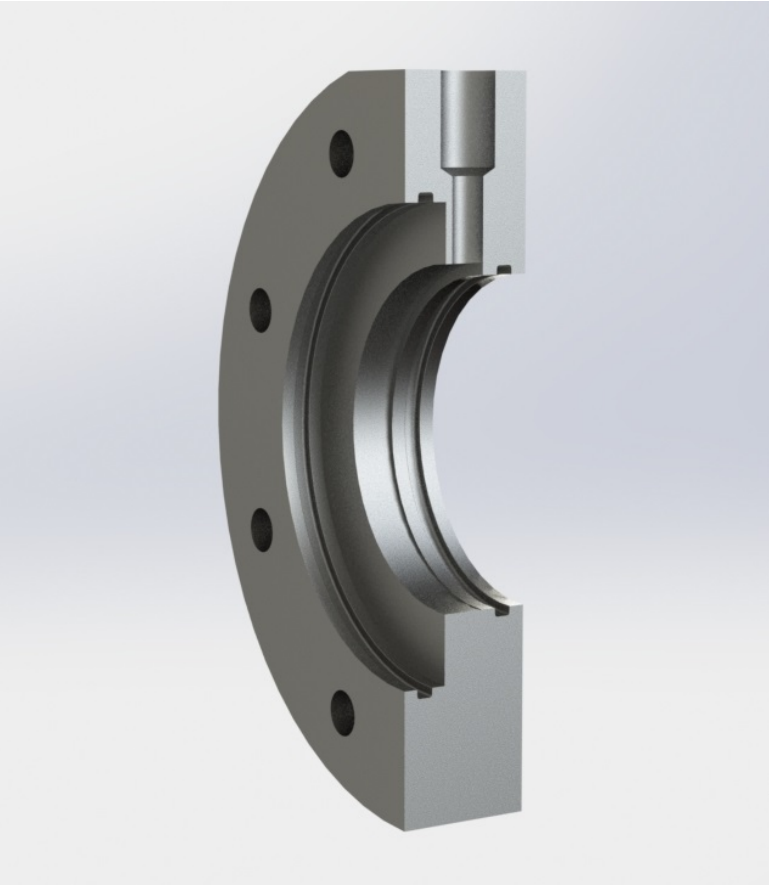

Figure 3.13: Connection flange (section view)

connection.

3.3.3 Closing flange

The closing flange, unlike the previous one, does not provide any connection with other components. The sole purpose is to provide a distribution system for feeding the cooling channels. Basically it is a simple cover that must be connected to the divergent of the nozzle. The choice of material, once again, falls on AISI630 stainless steel in order to maintain the same thermal properties with the nozzle (thermal expansion coefficient β). Also for this flange, as the previous one, two distribution systems have been envisaged, the one at constant fluid speed and the simplified one. For this flange, the sizing results to be simpler than the previous one and the only verification to be carried out is relative to the wall thicknesses to support the pressure of the coolant. Equation 2.16 can be used.

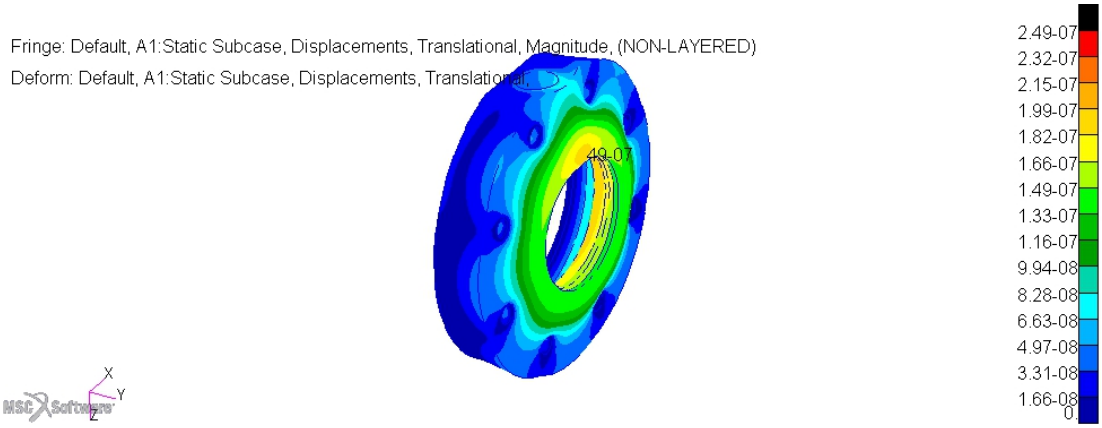

Figure 3.14: Connection flange deformations

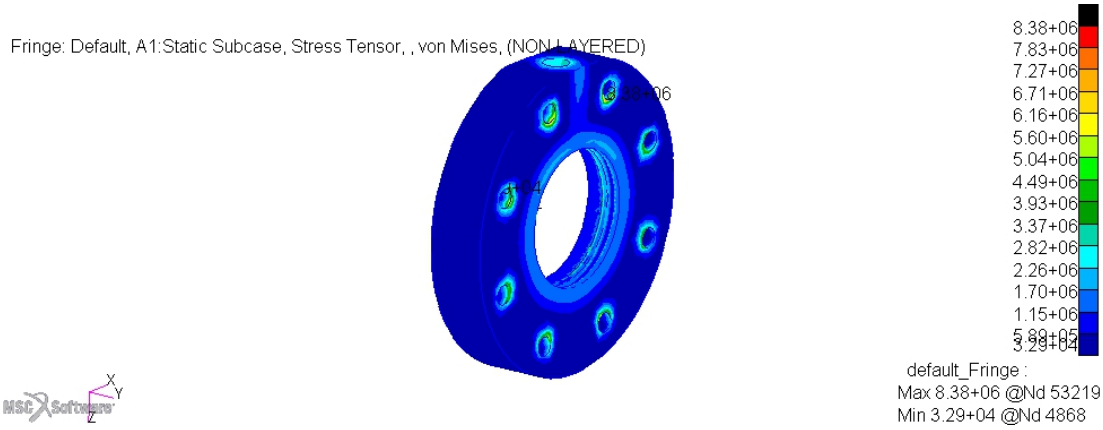

Figure 3.15: Connection flange stress tensor

Finally, the results of the structural verification are provided in figure 3.18 and 3.19, in which the various constraints and pressure loads acting have been applied.

3.3.4 Sealing and gaskets

The design of the gaskets required, for the different needs of chemical and thermal compatibility, to focus separately between the coolant side and the gas side.

Graphite packing

The gas side seal has been made with a carbon packing size of 5 x 5 [mm]. The choice of using this type of gasket was mainly due to the need to support high temperatures for long

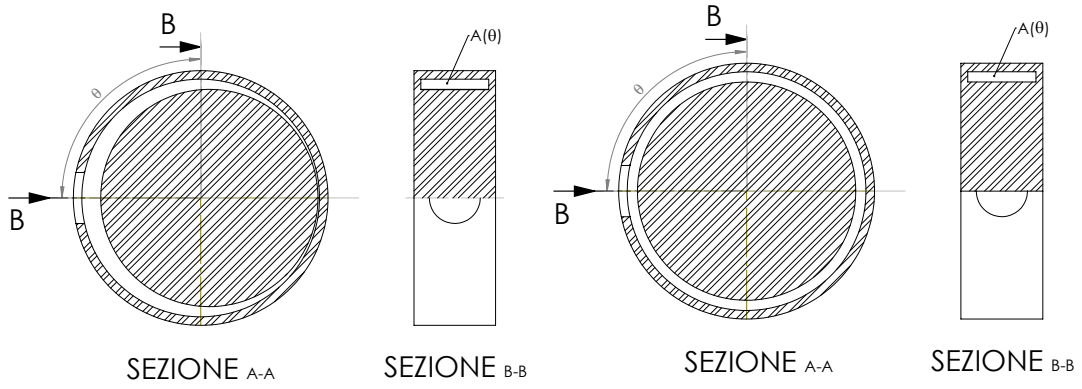

(a) Example of optimized volute definition (b) Example of simplified volute definition

Figure 3.16: Volute definition

times, while also ensuring a certain practicality of installation that did not distort the connection with the combustion chamber, designed for another engine. In particular, considering the geometry of the combustion chamber to which it was necessary to interface, the use of a packing constituted the simplest and most effective way to guarantee the seal. From the chemical point of view the packing also guarantees a good chemical compatibility since the concentration of the aggressive species is sufficiently low. The implementation did not foresee particular difficulties and the housing cavity has been obtained starting from a mechanical stop of the combustion chamber delimited by a specially designed cylindrical mobile insert (see the exploded view of figure 3.22). From a structural point of view it is a carbon braid suitably cut and placed inside of the designed cavity. The seal is ensured by compressing the seal inside the housing by means of the special tab made on the nozzle body. In relation to the previous experiences of the laboratory staff, it is expected to compress the packing up to half its thickness (5 x 2.5 [mm]). It is important to note that in the datasheet of the product there aren't mechanical information such as the Young's module or relating to the yield and compression stress necessary to achieve the desired deformation, for this reason we will proceed experimentally. In any case from the literature it is observed that for this type of gaskets the usual compression values vary between $69 - 279$ [MPa].

O-rings

The design of hydraulic seals, unlike the previous one, was more demanding and required numerous iterations due to the small size involved and the arrangement of the channel feed-

(a) Closing flange (b) Closing flange section view

Figure 3.17: Closing flange final prototype

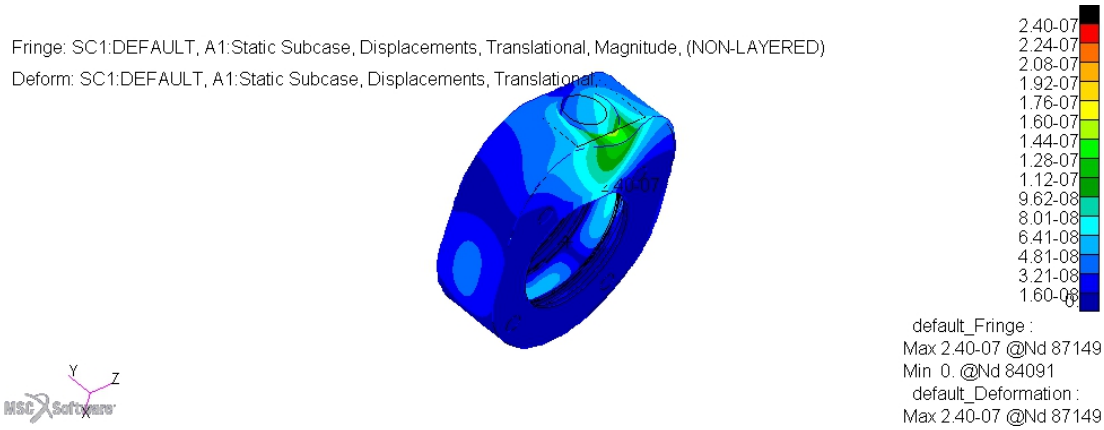

Figure 3.18: Closing flange deformations

ing systems. As for the chemical compatibility, as previously mentioned, the test phase will use water as coolant for this reason the main driver is once again the temperature. From the numerical analyzes of the 2.5.5 section and taking into account the conductivity of the nozzle material, it is expected that the maximum temperatures are indicatively below 250 [°C]. From the 2.3 figure of the Parker ® [25] manual, it is clear that from a thermal point of view the polymer that resists at higher temperatures is the *FFKM* (up to 320 [°C]) . From a chemical point of view, the 2.2.10 section of the manual ensures full compatibility with water and its vapor. Therefore, for the above considerations, the *FFKM* polymer is considered the most suitable for this application.

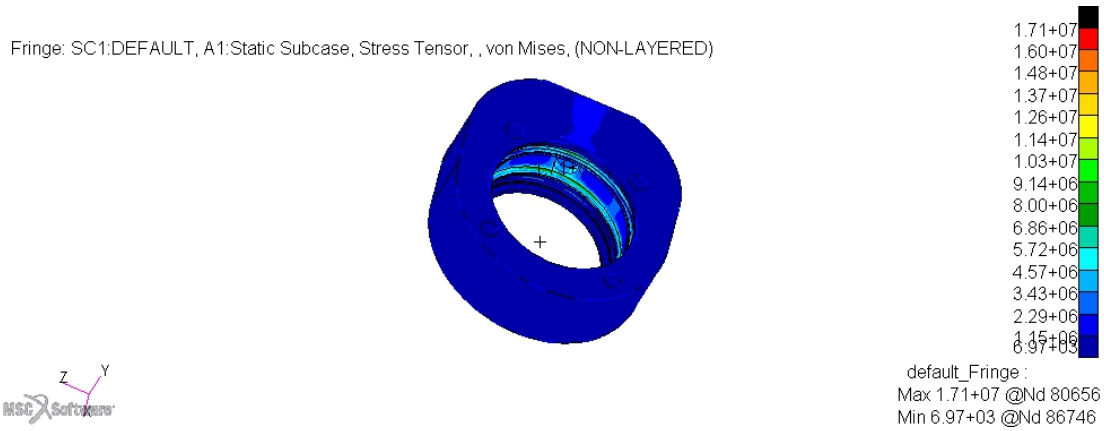

Figure 3.19: Closing flange stress tensor

As for the design, the case in question is static and with a plug groove on cylinder. The reference standard used is the industrial, although aerospace is also available. The choice to use the industrial regulation allows large tolerances and dimensions, however, for this specific case it turns out to be more than suitable, allowing also to find the material more easily, quickly and economically.

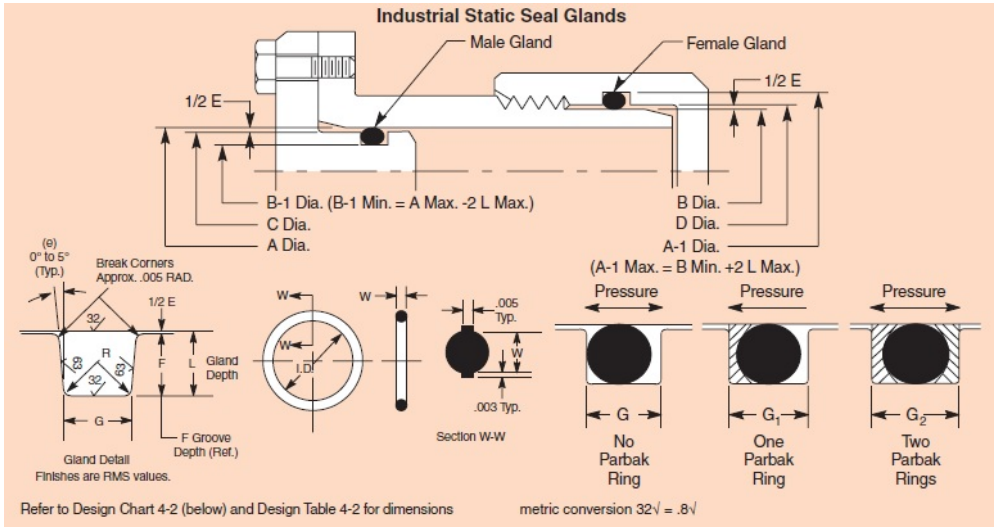

Figure 3.20: O-ring design specification

The current design foresees the realization of the grooves on the flanges therefore we follow the right scheme of the figure 3.20. The o-ring is a commercial component whose dimensions are standard, therefore the design leads to the identification of the most suitable

commercial measure and close to the needs. Only rarely and where strictly necessary, custom-made planning is used. The design of the grooves is done following the procedure defined in section $4.7.2$. For the problem under examination, the reference dimension is marked by the letter B of figure 3.20, using tables provided by the manual we obtain E, D and A_1. The manual also provides some further suggestions for a correct sizing of the groove and the choice of the o-ring. The size of the clearance given by the mechanical coupling is particularly relevant. In order to avoid extrusion, the manual 3.2 figure shows the maximum allowed clearance in relation to the operating pressure and the type of hardness of the o-ring. In the case in question it is sufficient to guarantee a clearance of less than 0.8 [mm]. In general, by mutual agreement with other manuals, a mechanical coupling of $H9$ - $H8$ / $f7$ is sufficient to avoid extrusion. Other advice given by the manual concerns pretensioning, groove filling and compression. The manual suggests that for static applications the correct compression of the o-ring is around $15 - 30\%$, that the groove filling is between $60 - 85\%$ with an optimal value around 75% and that the stretch is between $2 - 5\%$ (if the application is of short duration it can be extended up to 8%, in any case it must never exceed 25% during assembly). In this regard, some useful equations have been used to quantify the previous quantities, observing that the stretching produces a reduction of the section. For stretching the following is used where B is the diameter of the shaft according to figure 3.20, while $\varnothing_{ID}$ is the internal diameter of the o-ring.

$$X = \frac{B - \varnothing_{ID}}{\varnothing_{ID}} 100 \tag{3.15}$$

The section reduction due to stretching is quantified by the following interpolation.

$$\begin{aligned} W_{\%} &= -0.005 + 1.19X - 0.19X^2 - 0.001X^3 + 0.008X^4 \quad && 0 < X < 3\% \\ W_{\%} &= 0.56 + 0.59X - .0046X^2 && 3 < X < 25\% \end{aligned} \tag{3.16}$$

For compression, consider the 3.18, where the 3.17 describes the effective section diameter after stretching.

$$W_{end} = \frac{100 - W_{\%}}{100} W \tag{3.17}$$

$$C_{\Delta gr} = 1 - \frac{A_1 - B}{2\varnothing_{IDeff}} \tag{3.18}$$

Finally, for the filling of the groove, one can evaluate an infinitesimal section and consider

the relationship between the areas.

$$V_{\%} = \frac{(\frac{W_{end}}{2})^2 \pi}{GL} 100 \tag{3.19}$$

Below is the summary table of the o-rings and related grooves. In order to facilitate the retrieval and delivery times, gaskets have been chosen with the same nominal section diameter ($W = 1/16$ [in]) which corresponds to a standard groove width of $G = 0.093$[in].

o-ring	B [mm]	L [mm]	X%	W%	W_{end} [mm]	$C_{\Delta gr}\%$	$V_{\%}$
2-037	66	1.32	4.39	3.06	1.72	23.4	75
2-031	46	1.27	4.14	2.92	1.73	26.4	78
2-024	30	1.25	6.02	3.95	1.71	26.8	78

Table 3.4: O-ring and groove design

Further checks have been made by introducing the clearances due to the tolerances A_1 $H9$, D $H8$ and B $f7$. The presence of the min/max clearance modifies slightly the previous values, remaining always within the allowed intervals. For the sake of completeness, the actual operating values are given considering the coupling clearances.

case	∅	$\varnothing_N$[mm]	tol[μm]	es/ES[μm]	ei/EI[μm]	$\varnothing_m$[mm]	$\varnothing_M$[mm]
	B	66.00	30	-30	-60	65.940	65.970
1	D	66.00	46	46	0	66.000	66.046
	A	68.64	74	74	0	68.640	68.714
	B	46.00	25	-25	-50	45.950	45.975
2	D	46.00	39	39	0	46.000	46.039
	A	48.54	62	62	0	48.540	48.602
	B	30.00	21	-20	-41	29.959	29.980
3	D	30.00	33	33	0	30.000	30.033
	A	32.25	52	52	0	32.500	32.552

Table 3.5: Maximum and minimum dimensions of the coupling

Observe that at working temperature the polymer dilates by increasing $V_{\%}$ and $C_{\Delta gr}$, for this reason it is preferred to leave a certain margin.
As for the grooves, it has been decided to use an opening angle of 1 [°] for the o-rings $2-024$, 2 [°] for the others. The required surface finishes are 0.8 [μm] for the fund and 1.6 [μm]

case	g [mm]		L [mm]	
	min	max	min	max
1	0.030	0.106	1.335	1.385
2	0.025	0.089	1.283	1.326
3	0.020	0.074	1.260	1.297

Table 3.6: Clearances and heights of groove

case	X%		W%		W_{end}[mm]		$C_{\Delta gr}$%		$V_{\%}$	
	min	max	min	max	min	max	min	max	min	max
1	4.30	4.35	3.01	3.13	1.722	1.724	19.52	22.54	71.12	74.06
2	4.03	4.09	2.86	2.97	1.725	1.727	23.18	25.70	74.63	77.33
3	5.88	5.93	3.87	4.07	1.706	1.709	24.08	26.22	74.600	77.09

Table 3.7: Groove parameters according to the clearances

for the hips, according to the manual.
Special arrangements have been made to allow assembly. Specifically for the o-rings $2-037$ $2-031$ chamfers have been made while, for the other, considering the limited mechanical stop, the edge will be chamfered before assembly with fine sandpaper.

3.3.5 Threaded joints

The connections were made exclusively with threaded joints.
As for the combustion chamber, as it was designed for another engine, the sizing of the connection had already been done previously, while for the closing one it has been done ad-hoc.
For both connections, screws with a strength class of 8.8 were chosen according to *EN-ISO* $898-1$. The 8.8 class was considered the most suitable for the project, higher classes are not justified by the stresses present.
For both connections, the UNI $6761:1992$ regulations has been applied to verify the minimum space for keys maneuvering.

Combustion chamber and connection flange

The combustion chamber has been designed to operate with nominal pressures of 80 [bar] and has 8 holes $M6$. Now, since the nozzle operates at a much lower pressure, it has been

decided to protect the system from possible overpressure by using "explosive" bolts that fracture above a certain predetermined load. This function is performed by realizing an appropriate notched groove on the bolt (see figure 3.22 and appendix A). The dimensioning of the notched groove has been made keeping in mind that on the bolts act both pressure and the preload due to the compression of the packing[26]. The compression acting on the packing is quantified with the equation 3.20,

$$H_m = \pi b \varnothing_e \sigma_c \tag{3.20}$$

where b is the thickness of the packing, $\varnothing_e$ the outer diameter and σ_c the pressure corresponding to the deformation of 50 %. The load condition acting on each bolt is therefore given by the sum of the hydrostatic component due to the pressure plus that relative to the gasket. The nozzle area subjected to the action of pressure is quantified with the following equation.

$$A_r = ((0.5\varnothing_e)^2 - r_t^2)\pi \tag{3.21}$$

Now, knowing that the resistance class is 8.8, the first digit indicates the ultimate stress $\sigma_{UTS} = 800$ [MPa] while yield is given by the product of σ_{UTS} for the decimal of the second digit and we have $\sigma_y = 0.8 \cdot 800 = 640$ [MPa]. So the resistant section that must be guaranteed with the groove is given by 3.22.

$$A_{rt} = \frac{F_{rt}}{\sigma_{UTS}} \tag{3.22}$$

Finally, the loads acting on the individual bolts can be quantified by dividing the total loads by the number used, in this case 8. It is considered that the limit pressure is equal to $P_{cr} = 5P_{cc}$ and that $\sigma_c = 130$ [MPa]. To observe that this last value is empirically assumed within the interval provided previously, only experimental tests can confirm or modify this hypothesis. Assuming that the critical pressure is 5 times the operational pressure ensures a sufficiently safe margin in relation to the current nozzle liner thickness dimensions which ensure operation up to about 140 [bar] (see equation 2.16).

$\varnothing_e$[mm]	A_r $[mm^2]$	f_{op} [N]	f_{cr} [N]	f_{gsk} [N]	f_{totcr} [N]	A_{rt} $[mm^2]$
50	2154.71	269.34	1346.78	6381.36	7728.1	9.66

Table 3.8: Explosive bolts parameters

Where $f_{op} = \frac{P_{cc}A_r}{n_{blt}}$, $f_{cr} = \frac{P_{cr}A_r}{n_{blt}}$, $f_{gsk} = \frac{H_m}{n_{blt}}$ e $f_{totcr} = \frac{f_{cr}+f_{gsk}}{n_{blt}}$. It follows that the

core diameter should be approximately 3.5 [mm]. Finally, it is also possible to estimate the necessary tightening torque with the following simplified equation [26].

$$M_f = \frac{f_{totcr} d_n}{5300} \tag{3.23}$$

with $d_n = 6$ [mm] (M 6), we get $M_f = 5.8$ [Nm]. The throat will be made at a distance of 8 [mm] from the head of screw. Finally, considering that the mechanical processes always show a certain tolerance, their influence on the effective breaking pressure has been studied and the results were shown in the figure 3.21.

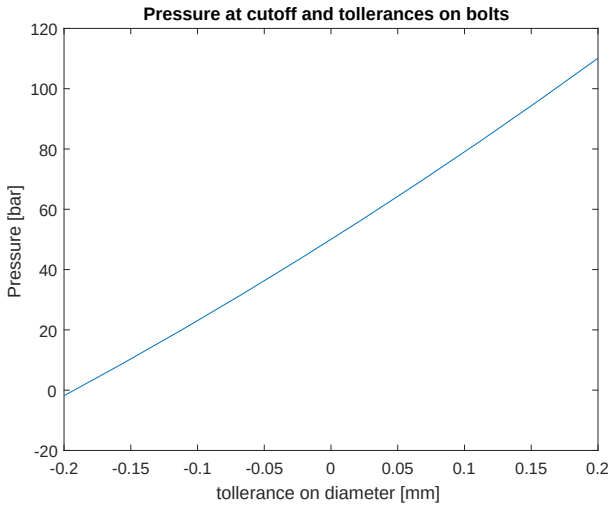

Figure 3.21: Effective critical pressure of fracture

Closing flange

For the closing flange, the threaded connection performs a limited structural function since the only stress that must be sustained is the pressure of the coolant inside the distribution system. From the point of view of the resultant, since the geometry is symmetrical and the pressure load acts normally on the surface, the axial component is zero while the radial component is opposed by the flange thickness and the coupling. The main role of the bolts is therefore to keep the flange in position and to avoid rotation.
Considering the previous, it has been decided to follow a simplified sizing identified in the manual. Specifically, the number of bolts to be used is determined with the following equa-

tion, which also ensures symmetrical tightening.

$$N_{bolts} = \frac{D}{40} + 4 \tag{3.24}$$

where D is the maximum diameter of the conduit to which the flange is connected and N_{bolts} is approximated to the nearest multiple of 4. In this case $D = 30$ [mm] and $N_{bolts} = 4$. Regarding the size of the connection, the screws were chosen $M3$ (class 8.8). From the point of view of the structural resistance the connection is strongly oversized. In this regard, consider the following summary table (3.9). The choice of using a $M3$ bolt mainly depends

d_{core} [mm]	σ_{UTS} [MPa]	F_{max} [N]	$F_{tot,max}$ [N]
2.571	800	4153.21	16612.85

Table 3.9: Connection resistance of the closing flange

on the practicality of use and the equipment available in the laboratory.

3.3.6 Connection joints

The connections to the coolant supply and discharge system have been made with stainless steel threaded fittings. For connection to flanges, a male tube-to-pipe adapter with $1/8$[in] thread and $1/4$[in] connector is used. The choice to use the $1/8 - 1/4$[in] configuration compared to the $1/4 - 1/4$[in] depends solely on the size of the closing flange. The second configuration in fact required a greater thickness of the flange, with consequent modification and extension of the supply channel. Although the $1/4 - 1/4$[in] could be used without complications for the connecting flange, the same connector as the closing flange has been used for ease of retrieval. The gaskets used are completely compatible with the fluid and supplied by the same supplier of the fittings. The installation of the fittings did not introduce particular complexity except the realization of a suitable smoothing on the flange side. The feeding channel of the volute has been made by simple drilling.
With regard to the connections to measuring instruments, power lines and tanks, Let-Lok® tube fittings with double ferrules have been used.

3.3.7 The final prototype

The final prototype represents the summary of all the design choices made. The prototype is summarized in the next images, the first is an exploded view with all the components (figures 3.22), while the second is a sectional view (figures 3.23).

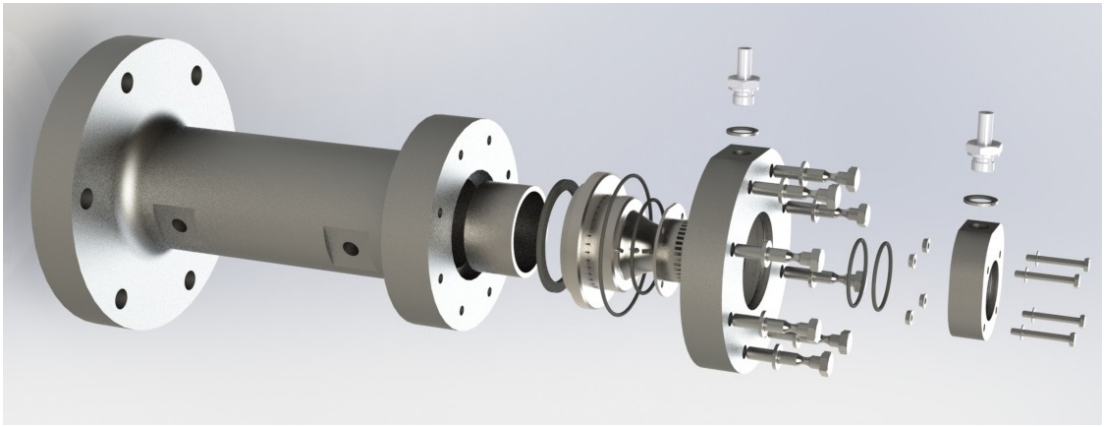

Figure 3.22: Exploded view with all components

To facilitate the understanding of the view and the identification of the various components in the 3.23 section view, different colours have been used which obviously do not correspond to reality. Particularly evident are the o-ring cavities, the tube-to-pipe fittings and the supply-distribution systems. Again from the previous image we can deduce that the flanges used are the optimized ones in which the fluid velocity is kept constant.
Finally, pay attention to some considerations related to the alignment of the nozzle with the flanges.
The nozzle structure is axially symmetric, however the number of channels provided is odd. To guarantee symmetry in the distribution of the fluid it is therefore necessary to align the feeding section of cooling system's channel with that of the supply hole of the volute. For the closing flange this operation is particularly easy as it is sufficient to orient the flattening for the fitting with the one made on the mechanical stop of the flange and then the bolts facilitate centering. For the connection flange, however, this operation is a little more laborious and requires to guarantee the parallelism between the planes of the fittings on the two flanges. It is worth pointing out that in the initial phase of the project a tongue-groove coupling was envisaged, however, the subsequent modifications made it too complicated to integrate, especially for the work required on the flanges. For this reason it was decided to carry out the alignment during assembly, paying attention to the parallelism condition pre-

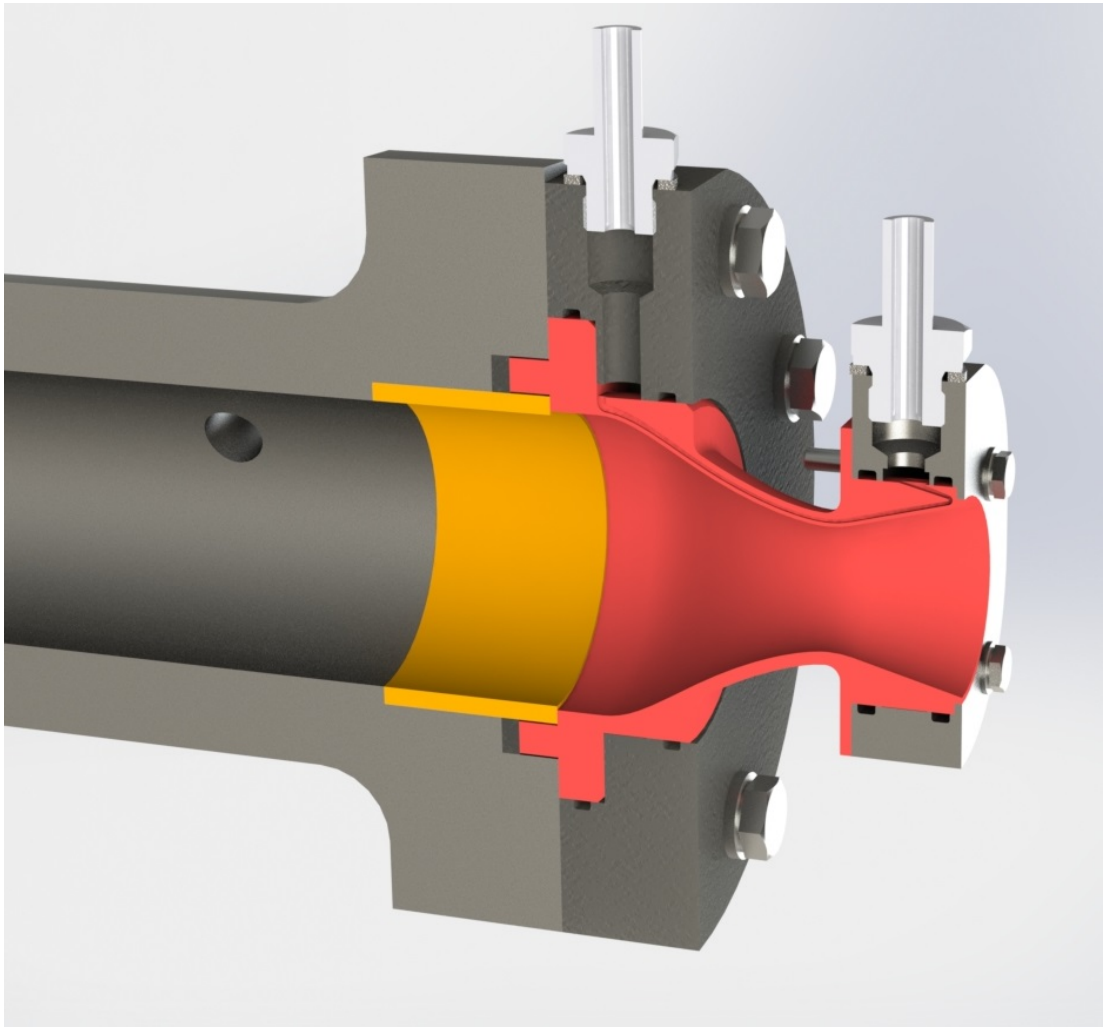

Figure 3.23: Section view of the whole project

viously described.
As far as dimensional tolerances are concerned, we have had to interface with the workshops and related equipment available. Specifically for the work on the flanges the general tolerance is ± 0.05 [mm] even if some dimensions have different specifications. However, we are willing to accept that the distribution volutes, due to the complexity of processing, present greater errors. All the components have been designed with SolidWorks® and the tables are shown in the Appendix A.

4

The prototype and test matrix

In this chapter we will discuss the operational choices for the preparation and implementation of the tests. The aim of the tests is to validate the prototype as a whole, both from a structural and a thermal point of view, with consequent validation of the numerical model and finally, a global assessment of the performances.

4.1 Final prototype

The realization of the main components of the prototype has been entrusted to specialized companies/workshops.
The nozzle has been created by $3D$ metal printing from a company with consolidated experience in the sector. The same has dealt with both the realization and the surface finishing processes to the machine tools, in order to guarantee the foreseen mechanical couplings. This operation made it possible to guarantee the required dimensional and geometric tolerances. At the end of the planned operations the nozzle appears as in figure X.

According to the design requirements described in chapter 3 regarding the inspection of the channels, appropriate checks have been carried out in order to guarantee the absence of obstructions. Initially, for this verification an x-ray radiography of the component was scheduled. However, the same company that took care of the realization, although having the required technology, could not carry out this verification due to the postponed entry into operation of the new installed machine. For this reason, to reduce the time and the

(a) Final nozzle prototype

(b) Final nozzle prototype 2

Figure 4.1: Different view of the nozzle

additional costs, an alternative method less accurate but equally effective has been used, that required to inject pressurized air into the channels.
In this regard, to further investigate the cleanliness of the channels and to be more confident with the $3D$ metal printing technology, further checks have been performed by cutting a dimensionally identical nozzle having the same channel geometry. The nozzle in figure 4.2 is an old version that preceded the final configuration and differs only in the channel feeding system and in the closing flange mechanical stop.

As far as the flanges are concerned, since they have been realized through conventional processes, they have been entrusted to a local trusted workshop. In particular, both configurations described in the previous design chapter were performed in order to evaluate the influences of the distribution system.

4.1.1 Assembling

The assembly of the prototype required the following operations. First of all the parts have been cleaned thoroughly from dust and any burrs, after which the following assembly sequence has been followed.

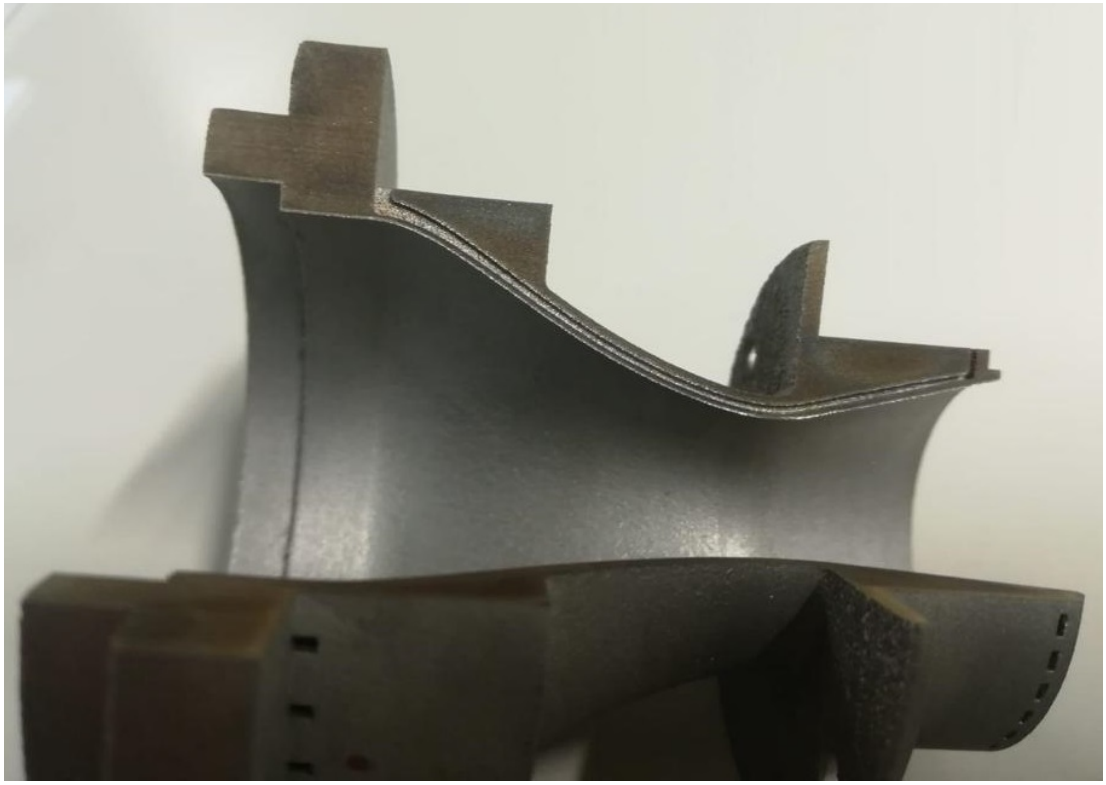

Figure 4.2: Sectional view of the previous nozzle prototype

First of all preliminary operations have been carried out, such as the cutting of the packing and the preparation of the flanges. With regard to the packing, once the exact length has been established, on the advice of the manufacturer's technical sheet, the cut has been performed with a very sharp blade maintaining an inclination of 45 [°]. Particular attention has been placed in the cut in order to avoid fraying. As regards the final assembly of the flanges, the male-to-pipe threaded connection has been screwed into each one with a special gasket.
Once the preliminary operations have been completed, the support cylinder has been inserted into the combustion chamber fixed to the measuring bench and the packing has then been inserted into the appropriate slot, paying particular attention to the arrangement. After this the nozzle was inserted into the combustion chamber slot.
At this point the connecting flange has been inserted. This operation took some time since it had to be ascertained that the o-rings were not pinched and that the leveling for housing the fitting was parallel with that made on the mechanical stop of the closing flange. The M6 bolts were partially screwed into the flange.

We then moved to the closing flange. In this case a preliminary operation was requested on the edge of the mechanical stop positioned at the nozzle outlet. In particular, due to the reduced dimensions of the stop, the bevel to the machine tools has been avoided in favor of a finish with fine sandpaper in order to avoid damage to the o-rings during insertion. Once the finish has been completed, the closing flange has also been inserted, paying particular attention to maintaining the parallelism condition between the leveling of the fitting and that of the mechanical stop. Finally the M3 screws were inserted and tightened with relative rosettes and nuts.
Subsequently, the M6 screws were tightened with a suitable torque wrench, respecting the sequence defined in the manual[5] to guarantee tightening symmetry.
Finally, all the connections to the power supply and measurement system were made using suitable fittings.

4.2 Feeding system

The feeding and pressurization circuit that will be used in the experiment is basically an adaptation of a system already designed and used successfully in many previous experiences. In particular, the configuration that will be used will provide to pressurize all the feeding and bleeding lines with nitrogen while the fuel will be powered by a pump. For safety reasons, instead of using hydrogen peroxide, it has been decided to use water in the regenerative cooling system, for this reason 3 feeding lines have been set up, two for the combustion chamber and one for the cooling system. The simplified scheme of the network is represented in the next image.

In the diagram of figure 4.3, the various lines have been represented with different colours depending on the fluid they convey. Regarding the bleeding there are two lines, one for the oxidant and one for the fuel. This precaution is of fundamental importance in order to increase the general safety standards and especially for hydrogen peroxide.
Nitrogen pressurization is regulated by means of valves, cavitating venturi and suitable pressure regulators. The choice to set up different lines for the main supply and for the purges depends on the degree of flexibility that is to be guaranteed and on the expected operating pressure levels. The implementation of the purging lines foresees two different philosophies according to the fluid conveyed. The first, intended for hydrogen peroxide, provides the sectioning of the circuit by means of valves, while, the second for diesel involves the use of spring loaded check valves. This choice depends mainly on the compatibility of the maneuvering

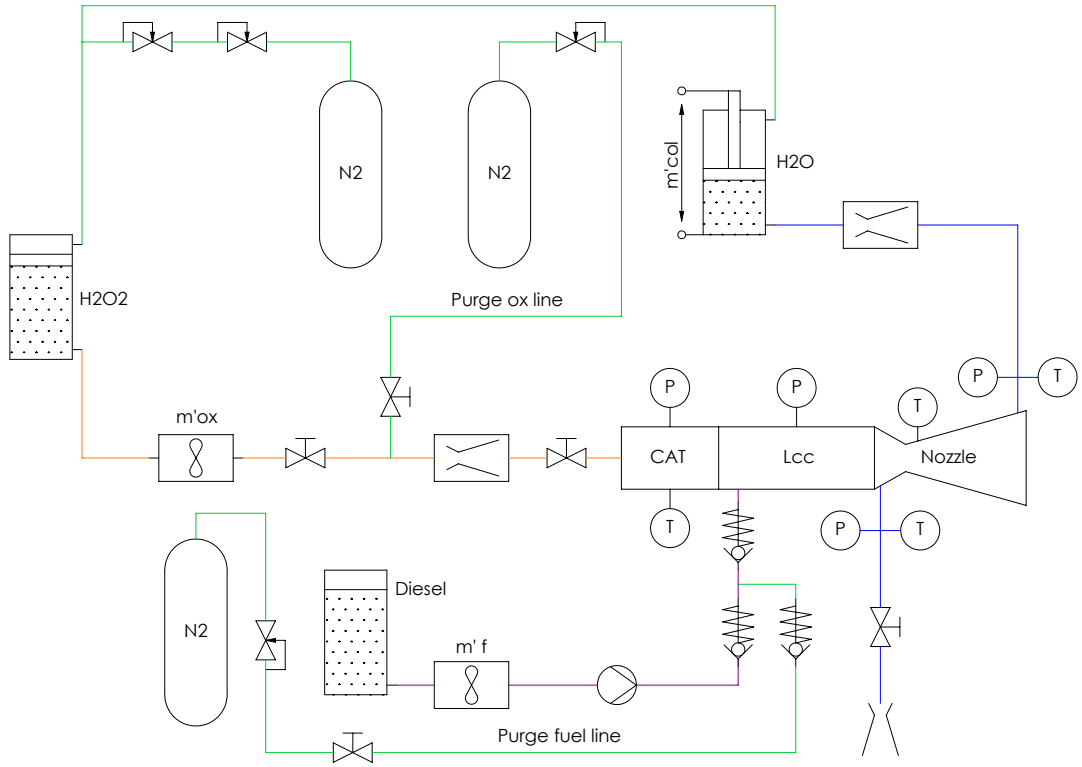

Figure 4.3: Simplified feeding system scheme

devices with the fluid and once again on the degree of security that is to be guaranteed.
The coolant line, on the other hand, provides an adjustment downstream of the regenerative system with a valve and a nozzle. The presence of these components serves not only to maneuver but also to recreate, during the tests, the same pressure conditions that would occur if the coolant outlet was connected to the catalyst input.
As far as the flow measurement is concerned, for the propellants there are two flow meter turbines, while for the coolant, the voltage signal from the linear potentiometer installed on the tank is provided, whose tips are respectively connected with the mobile plate and the tank itself.
In the hydrogen peroxide and coolant supply circuit two cavitating venturi will be also provided in order to stabilize the flow rates from any downstream pressure disturbances.
The whole engine system, consisting of catalyst, combustion chamber and nozzle will be mounted on a special frame bound to guides positioned on the base. The structure is designed to guarantee a degree of freedom along the direction of the thrust and will be con-

strained by load cells at the base for the relative measurement.
Finally, as regards temperature and pressure measurements, they will be carried out with manometers and thermocouples installed as shown in the diagram of figure 4.3. The thermocouples arranged in the appropriate wells made on the nozzle body, will also be added to the previous ones. The data will be collected with a PC data logger connected with appropriate electrical wiring to all the sensors in the circuit.

4.3 Text matrix

The tests that we want to conduct in this experience are the following:

1. Cold static test for verifying hydraulic seals
2. Cold test for evaluating true pressure losses in channels
3. Hot test for evaluating the regenerative cooling system
4. Thrust measurement

One of the advantages of liquid propulsion systems, as outlined above in the introductory chapter, is that it is possible to perform various tests on subsystems separately, thus guaranteeing complete freedom. Specifically, as regard the previous tests, the first two are performed with the engine off and therefore not in operating conditions. The last two instead require the operation of the entire system.

4.3.1 Cold static test

This first test is operationally simple and does not provide for particular procedures or complexities. The purpose of the check is to make sure the gaskets keep. The decision not to involve the combustion chamber and gas-side gaskets in the test also depended solely on the numerous successes found with the configuration adopted. Furthermore, as highlighted in the design phase, the combustion chamber was designed to operate with nominal pressures of 80 [bar] and the thickness of the nozzle liner, for reasons related to the realization with $3D$ printing, was oversized and it is estimated to be able to support comparable pressures, if not greater, than the nominal ones of the installed combustion chamber. As regards the procedure for carrying out this test, it is expected to proceed as follows.
First of all the tank containing the water is pressurized and the regenerative cooling system is fed by opening the maneuvering valve. The delivery valve is kept open for a certain period

of time so that all the channels can be filled and any air bubbles eliminated with the flow of the fluid. Once this feeding phase is terminated, the output valve to the regenerative system is gradually closed and, by means of the pressure gauge placed upstream of the distribution system, it is verified that the pressurization corresponds to the intended operation. The test is considered to be passed if there is no leakage of the refrigerant fluid. It should be noted that this test has the secondary effect of cleaning the channels more thoroughly than the procedure performed prior to assembly the prototype.

4.3.2 Pressure losses test

This second test aims to quantify the actual pressure losses, decoupling other effects related to heat exchange. The preparation required for this test is similar to the previous one, in fact it is a natural continuation.
As far as the operating procedure is concerned, the test will include feeding the regenerative system at a given pressure and varying the coolant flow rate by operating on the outlet valve. All the measures of interest are provided by the pressure and temperature indicators placed upstream and downstream of the regenerative system, while the flow control is performed by reading a linear potentiometer placed on the linear actuator of the line. At the end of the measurements the data will be re-elaborated and compared with the mathematical model realized. The objective is to verify the amount of distributed and localized losses.

4.3.3 Hot tests

This test phase is the most intense and involves studying the behavior of the nozzle from the point of view of heat exchange. The objective of this series of tests is to verify that the performances of the regenerative system are sufficient to ensure the operation of the engine for long periods, to validate the mathematical model used and if possible try to extend its validity.
From the operational point of view, the test is characterized by the following phases.
First of all, the regenerative system is fed, making sure that the outflow is regular and that any air bubbles trapped are purged. The regenerative system is supplied at the nominal pressure and mass flow rates conditions. All the quantities are taken from the instruments mentioned in the previous tests. This pre-feeding phase is of fundamental importance as it will allow to cool the nozzle and avoid intense thermal shocks due to starting.
Once the regenerative system is fully operational, the combustion chamber will be fed, ini-

tially only with hydrogen peroxide, then with the addition of diesel. This procedure is necessary because hydrogen peroxide is also used as an ignition system and at the beginning, when the motor is cold, decomposition takes a little longer. Once the catalytic bed reaches the operating temperature the decomposition becomes immediate. The starting procedure is delicate and care must be taken to avoid excesses in the injection because they could result in accumulations in the combustion chamber. That may give rise to detonations and/or instabilities. In the starting phase the engine will work in a monopropellant configuration and, as noted in the introductory chapter (chapter 2), combustion performances are lower with lower combustion temperatures. This more precautionary working condition will allow less stress on the motor case and to verify its behavior in safety. Although these do not represent the nominal operating conditions, it is possible to also collect a series of measures useful for describing the behavior of the regenerative system. The measurements that will be collected will be the temperature and pressure of the incoming and outgoing coolant, the flow rate of hydrogen peroxide and water and the wall temperatures detected by the thermocouples inserted in the appropriate wells. During the test the purpose of the thermocouples is to provide indications relating to the thermal state of the wall in order to interrupt the execution if certain values, assumed as a reference, are exceeded. This, in turn, allows to protect the nozzle from excessive stress.

Once the ignition has been completed and the combustion stabilized, the test can be started under the nominal conditions envisaged, collecting various measures. The test execution mode will provide to feed the engine under nominal conditions and to gradually change the coolant flow within a certain range. During the test, all the pressure and temperature measurements will be collected by the previously mentioned instruments and to ensure the correct o/f the fuel flow measurement will be added. The variation in the flow rate is of fundamental importance for the calculation of the global exchange coefficient. For statistical reasons, it is advisable to perform as many tests as possible, compatibly with the costs and the nozzle wear status.

Once the data collection phase has been completed, the propellant supply to the engine will be interrupted with the consequent purge of the hydrogen peroxide and diesel lines while the regenerative system will remain active for a certain amount of time.

4.3.4 Thrust measurement

This last test, as you can guess from the title of the section, will concern the measure of thrust. Regarding the layout of the test, the configuration relative to the previous test will remain

unchanged so that the measurements will be carried out in the same session of the hot tests simultaneously with the others related to the regenerative system. In this regard, it is good to clarify some precautions regarding the installation of wiring and connections, in order to disrupt the thrust as little as possible. As previously mentioned, the engine frame leaves a degree of axial freedom for the measurement of thrust by means of a guide system. In order for the measures to be perturbed as little as possible, all the wiring and the various connections must not introduce constraint components in the same direction as the thrust. This will complicate the installation by requiring to arrange the supply lines and the various wiring in a plane orthogonal to that of the thrust. Obviously it will be necessary to find a compromise.

4.4 Estimation of propellants and pressurizing

It is possible to quantify a priori the quantities of propellants and pressurizing gas required in the tests. As far as hydrogen peroxide and diesel are concerned, the estimate of the quantities required is facilitated by the knowledge of the requested mass flow rates under nominal operating conditions. However, the exact duration and the test number are currently unknown. In any case, the estimate can be made as follows.

$$m_{ox,tot} = \dot{m}_{ox} t_b n_{test} \tag{4.1}$$

$$m_{f,tot} = \frac{\dot{m}_p}{1 + \frac{o}{f}} t_b n_{test} \tag{4.2}$$

Regarding pressurization with nitrogen, the estimate can be made by an energy balance, considering an adiabatic expansion, assuming that the gas can be treated with the ideal model and there is no evaporation of the fluid or dissolution of the gas in the propellant[1]. In the event that the various tanks are pressurized at the same pressure, the equation 4.4 can be used, otherwise the 4.5 is used.

$$m_{g_0} c_v T_0 = m_g c_v T_g + m_p c_p T_p + P_p V_p \tag{4.3}$$

Starting from the energy balance described by 4.3, applied to a simple system consisting of a pressurized tank directly connected to that of the propellant, the following estimates are

obtained.

$$m_{g_0} = \frac{p_p V_p}{R_g T_0} \left(\frac{k}{1 - \frac{P_g}{P_0}} \right) \tag{4.4}$$

$$m_{g_0} = \frac{k}{R_g T_0} \frac{\sum_{j=1}^{n} P_j V_j}{1 - \frac{P_g}{P_0}} \tag{4.5}$$

Where 0 refers to the initial state, while the instantaneous conditions in the gas and propellant tank respectively *g* and *p*. R_g is the gas constant used (R/M_m) specific for mass units. The different pressurization in the various tanks is guaranteed by pressure regulators. A punctual energy balance would therefore require to introduce also the losses due to the various devices present on the line, however the goal is to obtain an estimate and not an accurate measurement. In practice, the 4.4 is frequently used, increasing the estimated value of a 5-10% depending on the degree of confidence and the type of application. Note that the 4.5, assuming that the P_j are all the same, leads to 4.4 where V_p is nothing more than the sum of propellant volumes to be ejected .

5 Conclusions

5.1 Conclusions

The entire work carried out has allowed to investigate in depth the regenerative cooling applied to the nozzles of rocket engines.
Specifically, it allowed to study in detail the influences of the numerous parameters involved, determining the cause-effect relationships. In this regard, at the end of the second chapter, a series of analyzes have been carried out in order to deduce the various influences with a subsequent exhaustive discussion of the results obtained within the 2.5 section. Some relationships have been immediately understood and expected, while others have asked to dwell more on further analysis or extending the numerical domain. In any case, the various scenarios proposed have highlighted and reconfirmed the complexity of the physical phenomenon studied in which converge the influences of the fluid dynamic, the transport of heat and the chemical and structural limits of the materials.
The design phase has allowed to develop and, in some cases, to consolidate a series of skills that had not been fully exploited before. In particular, the fact of having to reconcile the abstraction of mathematical models with reality, has required the development of a new way of thinking and approaching in solving problems, always paying attention to simplicity, feasibility and cost. Essentially all the typical requirements of industrial design. This phase also allowed to learn a lot of information about the new processes of addictive manufacturing, which proved to be versatile and particularly interesting for the aerospace sector. From the

point of view of the acquired skills, this design experience has allowed to learn, starting from scratch, the design of the components using *CAD* software and to concretely apply the concepts of technical drawing learned within the course of study.
As regards the various components used, such as gaskets, threaded connections, the need to consider different solutions has allowed to know more in detail the strengths and weaknesses of the various technologies available, also maturing skills to select the most suitable configurations case. This process has therefore allowed to develop a certain sensitivity, of fundamental importance in decision-making processes.
Let's move on to the last phase related to the tests. Unfortunately, it has not been possible to conduct the experimental measures within the project due to the planned deadlines.
Nevertheless, this has allowed to highlight that time is a precious resource that must be taken into account on a par with others. In particular, the flanges processing phase took longer than expected due to previous works accumulated by the workshops, by slipping the test date in a period in which others were planned. Since laboratory equipment is also a limited resource, it has not been possible to set up the laboratory in time for the project to be completed.
In any case, the following predictions are expected from the tests.
As regards the first cold test related to the sealing of the o-rings, this is expected to be verified. In particular, the use of o-rings in similar applications, with these pressure values, is quite common, therefore no particular complexities are expected which may affect the seal. If there are any problems, they will most likely be attributable to assembly phase.
Let's move on to the second pressure loss measurement test.
From the operational point of view there are no particular complexities. With regard to the results obtained, we expect to find a certain difference with respect to the theoretical prediction model, because the measuring instruments are placed in different positions with respect to the mathematical simulation. Specifically, the mathematical model calculates the pressure losses starting from the input section in the volute up to the emission one. In the prototype the pressure indicators are connected to the supply line by means of union cross provided respectively upstream and downstream of the male-to-pipe fittings. It is therefore expected to introduce a correction aimed at reducing pressure loss measures due to the localized reductions at the supply channels. This correction will be carried out always using the tabulated coefficients for sudden reduction or enlargement of the conduit sections. Once this operation has been carried out, the measurements obtained will be compared. Despite this correction, we will again expect a certain difference between the results obtained from the analytical and experimental models. Most likely these differences will be due to an incorrect

measurement of the surface roughness of the channels and / or an inappropriate choice of the coefficients used for the localized losses. The roughness measurement can be performed with a roughness meter even if the exploration of the internal walls of the channels is little, if not, practically inaccessible. In any case, to obtain reliable results many measures should be carried out involving all the walls of the channels. Only in this case there would be an high degree of confidence in the measurement of roughness. Since it is a poorly achievable solution, we will have to settle for some measurements obtained on the sectioned nozzle mentioned previously in the chapter 4. Taking this aspect into account, assuming a certain reference value of the roughness, it will be easier to identify any corrections related to the concentrated loss coefficients.

Now let's move on to the validation of the heat exchange model. This will be the most complex part of the tests due to the large number of measurements and quantities involved. Also in this case substantial differences between the analytical forecasts and the measurements will be expected. Certainly the choice to apply the numerous hypotheses discussed in the 2.2.1 section will influence the results. In particular, it is known that the one-dimensional gas-dynamics describes the phenomena with an accuracy of about 80 % compared to the three-dimensional one and the choice to study the evolution of the gas in *frozen* conditions has a direct impact on the temperatures and therefore again on the results.

Under *frozen* conditions some energy channels are excluded in the evaluation of energy transfer. In the case under examination, the hypothesis of considering the flow chemically and vibrationally *frozen* has allowed to study the gas as calorically perfect and, if on the one hand has allowed to substantially simplify the problem, on the other it underestimates the actual temperatures [10]. In real conditions, during the expansion process, there is a gradual recombination of chemical species and radicals into more stable energy molecules. This exothermic process releases energy that is transferred into translational, rotational and vibrational modes with the consequent result that the final temperature of the gas is on average higher than the *frozen* configuration. Although some corrections have been introduced, among which those relating to the radiative flow, they are expected to be insufficient.

As regards the *Bartz* relationship, in the literature a good approximation for medium and medium-large size motors is shown. However for small motors there are also discrepancies with *CFD* models. It is good to note that no conditions have been identified that limit the use of this empirical equation, therefore it is not known what type of approximation has been introduced. On the basis of the literature it is observed that the major disagreement occurs in the combustion chamber and in the convergent section [23].

To influence the prediction, as already observed in the chapter 2, will also be the accuracy of the data related to the properties of the metal and the coolant used. In addition to the previous approximations there are also the equations used for the estimation of the convective coefficient on the coolant side, which we remember to have been valid under permanent regime conditions. In the case in question, due to the variability of the conduit section and the boundary conditions, the outflow can be considered permanent only within the single element *FEM*.

Finally, if we consider the case in which combustion is not axial but swirl, we will also add to the previous unknowns the estimate of the convective coefficient on the gas side. Most likely, a replacement or corrected equation to *Bartz* will be needed. Taking into account the dynamics of the fluid, it will be expected that the flow of heat transferred in the second case is more intense, however, no empirical predictive models are available.

It is therefore understandable that due to the number of variables involved and the simplifications, it will be difficult to validate the model in its individual parts. The best hypothesis will be to identify, by appropriately varying the flow rate of coolant, the global convective correction coefficients. For this reason, any extensions of validity of the model will be possible only limited and in relation to the predictive accuracy that we are willing to accept.

Finally, as regards the measure of thrust, also in this case we will expect to detect differences with respect to the estimated values. Assuming to adopt all the precautions described in the chapter 4 in order to reduce constraint components along the thrust direction and to correct any uncertainties due to the measuring instruments, the differences that will be expected to be recorded are mainly due to the typical problems encountered in this class of engines. Specifically, it is expected to detect a thrust lower than the theoretical expected due to radial velocity components in the divergent, biphasicity of the flow, chemical kinetics, erosion of the throat, presence of the boundary layer and non-unitary combustion efficiency. Although there are empirical and theoretical relationships capable of providing estimates for the various losses, many requested quantities are not available because they in turn require experimental estimation. From these equation, not shown here, it can be observed only that small engines are more affected by some effects, presenting higher losses of performance due to the non-scalability of some physical phenomena, first of all the boundary layer. Therefore, for reasons of convenience it will be easier to define a global efficiency factor representative of the combustion and expansion efficiency of the entire engine. Recalling that the test will

be in adapted pressure condition,

$$F = \dot{m}_p c_{F,th} c^\star_{th} \eta_{tot} \tag{5.1}$$

where

$$\eta_{tot} = \eta_{c_F} \eta_{c^\star} \tag{5.2}$$

It is worth noting that with the measuring instruments available will not be possible to separate the two contributions making up the overall performance.

5.2 Future work

The natural continuation of this work will involve performing all the tests described in the test matrix of the 4.3 section, respecting the procedures described in the chapter. Data processing will follow by introducing corrections and where possible, to propose validity extensions. Finally, if the previous configuration studied works successfully, we will try to predict the performance for the orbital configuration.

Figure 5.1: Draft of the orbital configuration

References

[1] G. P. Sutton and O. Bilbarz, *Rocket Propulsion Elements*, 8th ed. John Wiley and Sons Inc., 2010.

[2] M. E. Boysan, "Analisys of regenerative cooling in liquid propellant rocket engines," 2008.

[3] P. R. Gradl, "Rapid fabrication techniques for liquid rocket channel wall nozzles," *AIAA-2016-4771*, 2016.

[4] M. Hallquist, "Heat transfer and pressure drop characteristics of smooth tubes at a constant heat flux in the transitional flow regime," 2011.

[5] ASME, *Rules for construction of pressure vessells*, 8th ed., 2010.

[6] Wikipedia. [Online]. Available: https://en.wikipedia.org/wiki/Hydrogen_peroxide

[7] G. Rarata and P. Surmacz, "The safe preparation of htp and concentrated h202 samples," *Transaction of the institute of aviation*, vol. 217, pp. 118–121.

[8] M. J. Turner, *Rocket and Spacecraft Propulsion*, 2nd ed. Springer and Praxis Publishing, 2005.

[9] S. P. Group. Hybrid rockets history. [Online]. Available: http://www.spg-corp.com/News_12.php

[10] R. Humble, G. Henry, and W. Larson, *LSC Space Propulsion Analysis and Design*, 2nd ed. Mcgraw-hill Education - Europe, 2007.

[11] D. Andrews, "Advantages of hydrogen peroxide as a rocket oxidant," *Journal of The British Interplanetary Society*, vol. 43, pp. 319–328, 1990.

[12] M.Ventura and G.Garboden, "A brief history of concentrated hydrogen peroxide uses," *AIAA -99-2739*, 1999.

[13] S. Interox®, *Hydrogen peroxide handling and storage*, 1998.

[14] S. Gordon and B. J.McBride, "Computer program for calculation of complex chemical equilibrium composition and application," *Reference Publication 1311*, vol. 1 Analysis, 1994.

[15] ——, "Computer program for calculation of complex chemical equilibrium composition and application," *Reference Publication 1311*, vol. 2 User manual and description, 1996.

[16] U. technologies. [Online]. Available: http://www.h2o2.com/technical-library/physical-chemical-properties/physical-properties/default.aspx?pid=20&name=Physical-Properties

[17] B. j.McBride, S. Gordon, and M. A.Reno, "Coefficient for calculating thermodynamic and transport properties of individual species," *NASA technical memorandum 4513*, 1993.

[18] Rocketdyne, "Hydrogen peroxide handbook," *Chemical and Material Sciences Department Research Division, Technical Report AFRPL-TR-67-144*, 1967.

[19] D. Huzel and D. Huang, *Design of liquid propellant rocket engines*, 2nd ed., 1971.

[20] C. Bonacina, A. Cavallini, and L. Mattarolo, *Trasmissione del Calore*, 3rd ed. CLEUP-Padova, 1992.

[21] P. S.J., "Design and validation of a micro bi-propellant rocket motor," 2015.

[22] R. Schuff, M. Maier, C. U. Oleg Sindiy, , and S. Fugger, "Integrated modeling and analysis for a lox/methane expander cycle engine: Focusing on regenerative cooling jacket design," *AIAA 2006-4534*, 2006.

[23] *Thermal analysis of liquid rocket engine*.

[24] Q. Wang, F. Wu, M. Zeng, L. Luo, and J. Sun, "Numerical simulation and optimization on heat transfer and fluid flow in cooling channel of liquid rocket engine thrust chamber," *International Journal for Computer-Aided Engineering and software*, 2006.

[25] Parker, *Parker O-Ring Handbook*, 2007.

[26] M. Santi, "Progettazione di un motore liquido a base h202 per applicazioni spaziali," 2015-2016.

Acknowledgements

First of all a heartfelt thanks to the supervisor Prof.Pavarin who gave me the opportunity to realize this study not only from the theoretical but also practical point of view, allowing me to get in touch with all the typical problems of the development of a prototype and therefore of form me more completely.
I also thank the co-supervisors who have provided their time, skills and valuable experience, allowing me to expand specific knowledge of this industrial sector and beyond.
A heartfelt thanks goes to my whole family and in particular to my parents for allowing me to face economically my studies and for the continuous support.
Finally, since we are not alone in equations and numbers, i would like to thank my friends and all those who have remained close to me during these years.

A
AppendixA

Drawing boards.

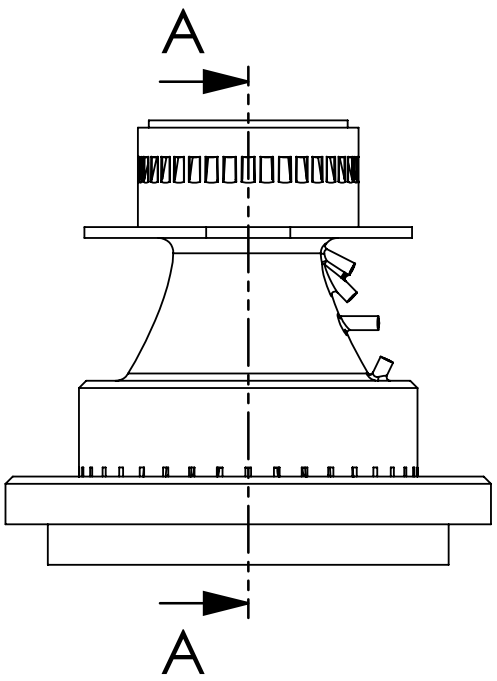

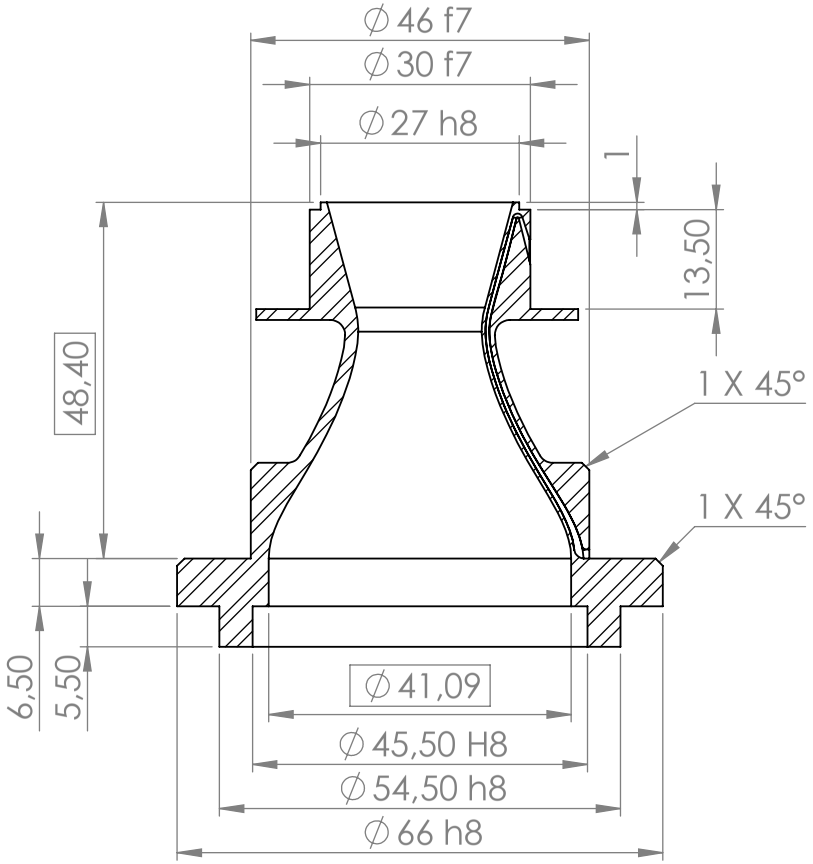

SEZIONE A-A

3					
2					
1					
VERS	CHANGE DESCRIPTION	PROPOSED BY	DATA	SIGN.	CHECKED

DATA 03/02/2019	DRAW BY Matteo Fagherazzi	SCALE 1:1	COMM.
Chamfers without dimension: 0.1 mm X 45° Round without dimension: R=0.2 mm		MATERIAL Stainless steel CL 20ES	
GENERAL TOLERANCE: +/- 0.05 mm		QUANTITY 1	SHEET NUM: 1/1
GENERAL ROUGHNESS: 6.3 micrometers			REPLACE. DRAW:
COMMITTANT Università di Padova		RAW DIMENSIONS	TREATMENT
TITLE Nozzle ver.B		PROGRAM Cooled nozzle	DRAWING NUMBER ugello_prgd_versione B

Università degli Studi di Padova

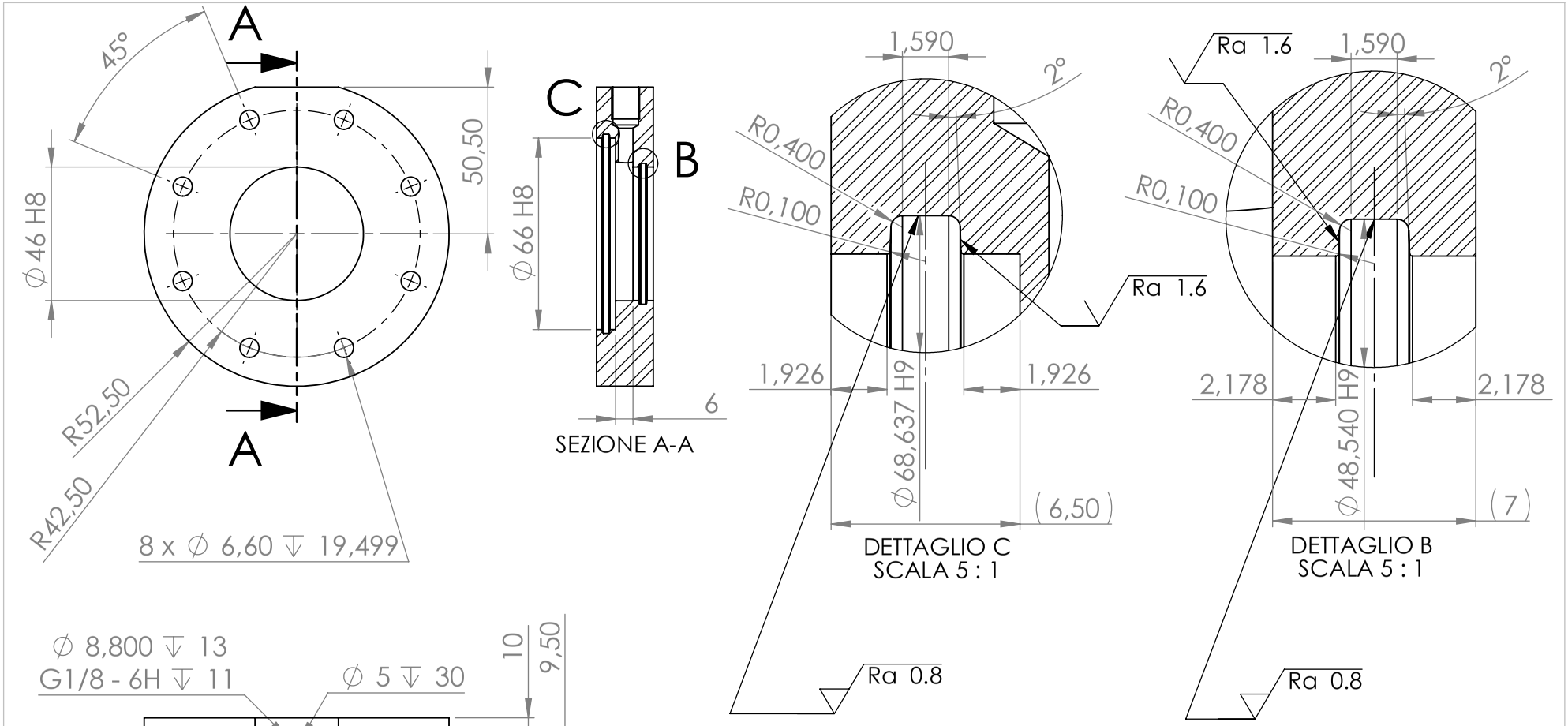

3					
2					
1					
VERS	CHANGE DESCRIPTION	PROPOSED BY	DATA	SIGN.	CHECKED

DATA 03/02/2019	DRAW BY Matteo Fagherazzi	SCALE 1:2	COMM.
Chamfers without dimension: 0.1 mm X 45° Round without dimension: R=0.2 mm		MATERIAL Stainless steel AISI 630	
GENERAL TOLERANCE: +/- 0.05 mm		QUANTITY 1	SHEET NUM: 1/3
GENERAL ROUGHNESS: 6.3 micrometers			REPLACE. DRAW:
COMMITTANT Università di Padova		RAW DIMENSIONS	TREATMENT
TITLE Connection flange		PROGRAM Cooled nozzle	DRAWING NUMBER flangia_attacco

Università degli Studi di Padova

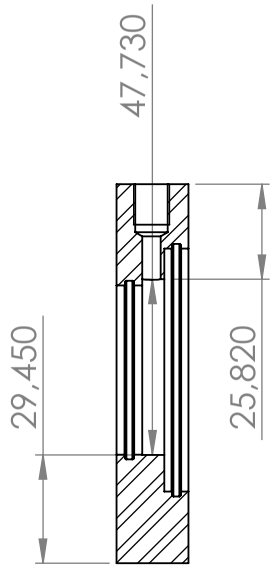

SEZIONE G-G

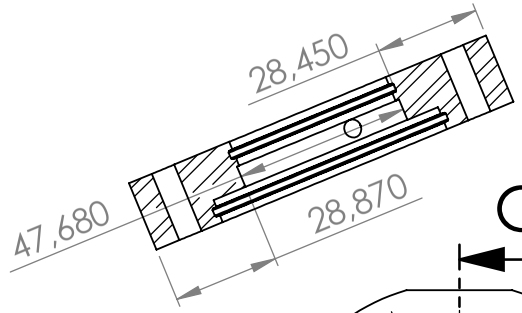

SEZIONE E-E

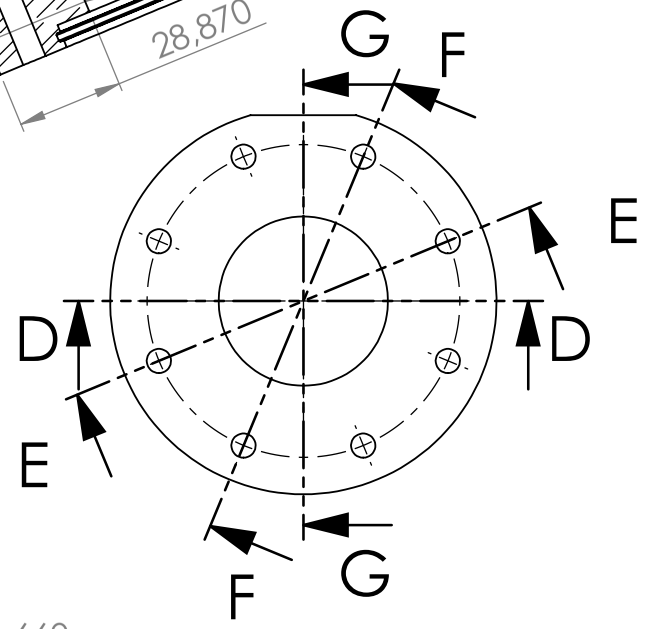

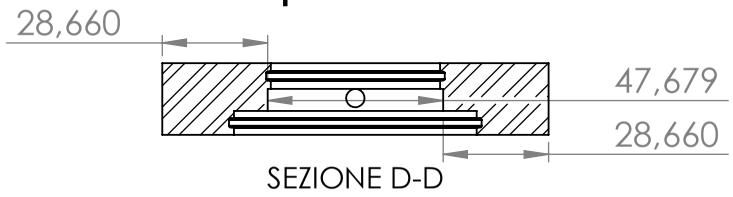

SEZIONE D-D

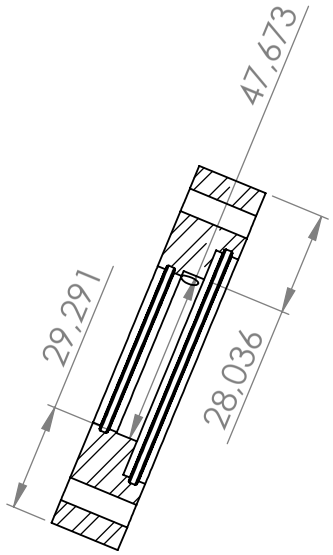

SEZIONE F-F

3					
2					
1					
VERS	CHANGE DESCRIPTION	PROPOSED BY	DATA	SIGN.	CHECKED

DATA 03/02/2019	DRAW BY Matteo Fagherazzi	SCALE 1:2	COMM.
Chamfers without dimension: 0.1 mm X 45° Round without dimension: R=0.2 mm		MATERIAL Stainless steel AISI 630	
GENERAL TOLERANCE: +/- 0.05 mm		QUANTITY 1	SHEET NUM: 2/3
GENERAL ROUGHNESS: 6.3 micrometers			REPLACE. DRAW:
COMMITTANT Università di Padova		RAW DIMENSIONS	TREATMENT
TITLE Connection flange		PROGRAM Cooled nozzle	DRAWING NUMBER flangia_attacco

Università degli Studi di Padova

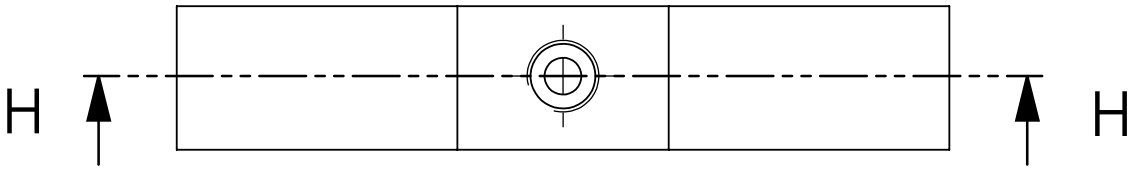

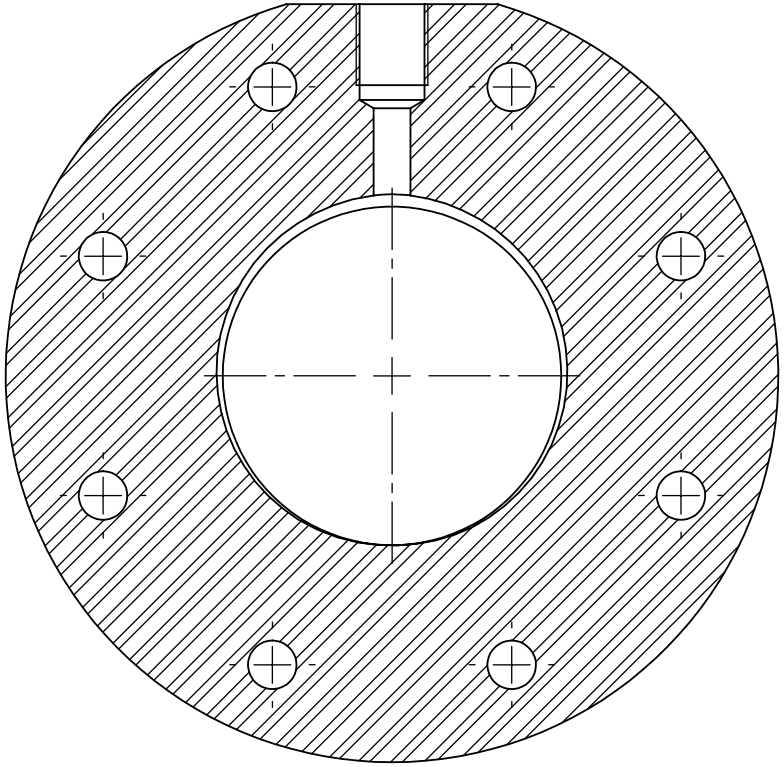

SEZIONE H-H

3					
2					
1					
VERS	CHANGE DESCRIPTION	PROPOSED BY	DATA	SIGN.	CHECKED

DATA 03/02/2019	DRAW BY Matteo Fagherazzi	SCALE 1:1	COMM.
Chamfers without dimension: 0.1 mm X 45° Round without dimension: R=0.2 mm		MATERIAL Stainless steel AISI 630	
GENERAL TOLERANCE: +/- 0.05 mm		QUANTITY 1	SHEET NUM: 3/3
GENERAL ROUGHNESS: 6.3 micrometers			REPLACE. DRAW:
COMMITTANT Università di Padova		RAW DIMENSIONS	TREATMENT
TITLE Connection flange		PROGRAM Cooled nozzle	DRAWING NUMBER flangia_attacco

Università degli Studi di Padova

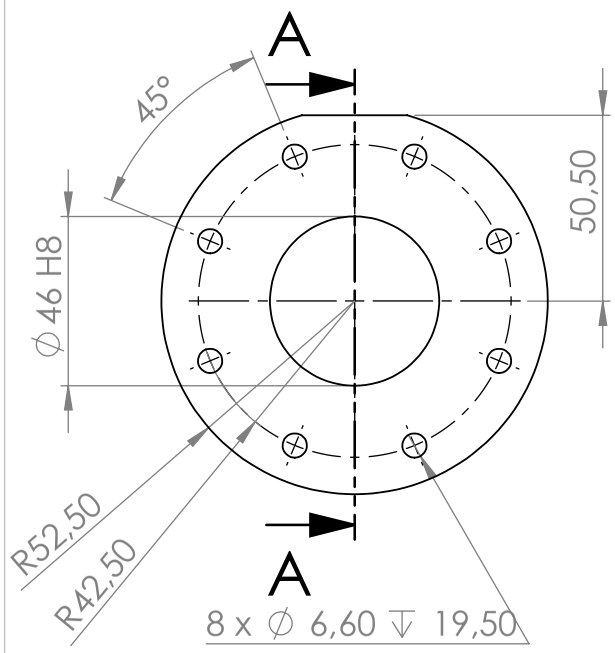

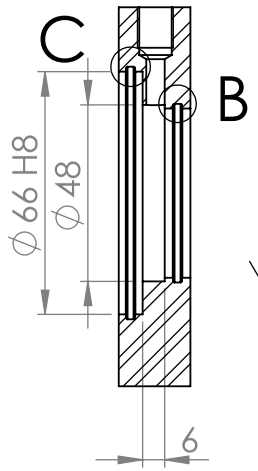

SEZIONE A-A

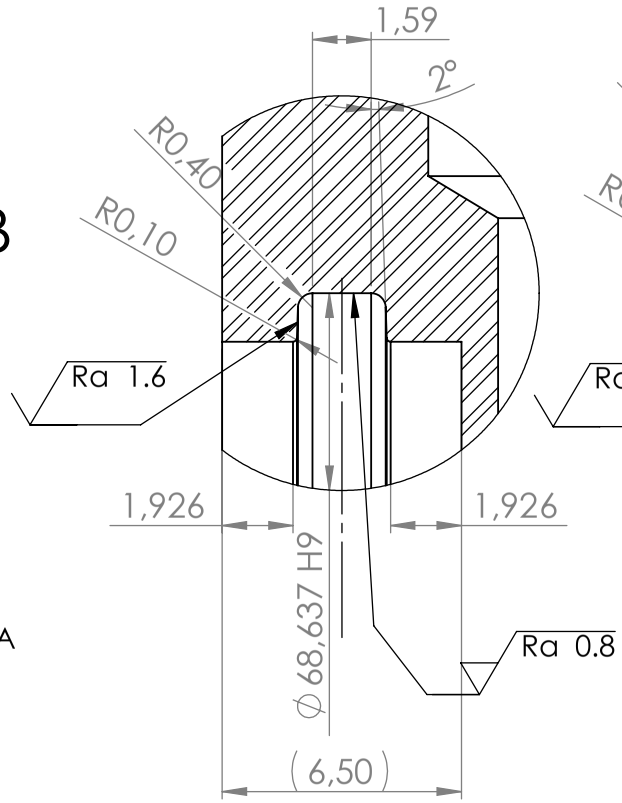

DETTAGLIO C
SCALA 5 : 1

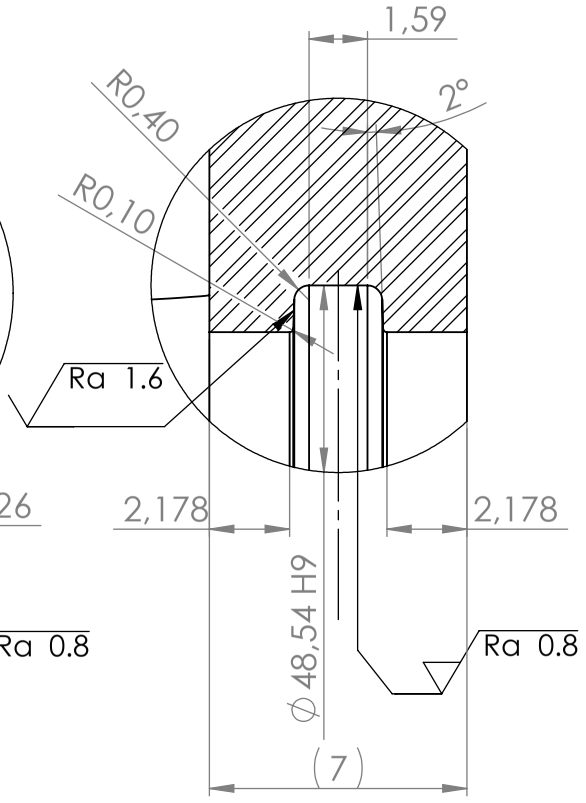

DETTAGLIO B
SCALA 5 : 1

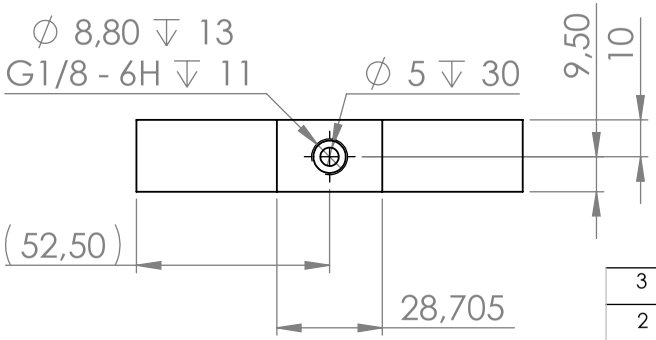

3					
2					
1					
VERS	CHANGE DESCRIPTION	PROPOSED BY	DATA	SIGN.	CHECKED

DATA 03/02/2019	DRAW BY Matteo Fagherazzi	SCALE 1:2	COMM.
Chamfers without dimension: 0.1 mm X 45° Round without dimension: R=0.2 mm		MATERIAL Stainless steel AISI 630	
GENERAL TOLERANCE: +/- 0.05 mm		QUANTITY 1	SHEET NUM: 1/1
GENERAL ROUGHNESS: 6.3 micrometers			REPLACE. DRAW:
COMMITTANT Università di Padova		RAW DIMENSIONS	TREATMENT
TITLE Connection flange (simplified)		PROGRAM Cooled nozzle	DRAWING NUMBER flangia_attacco_semplificata

Università degli Studi di Padova

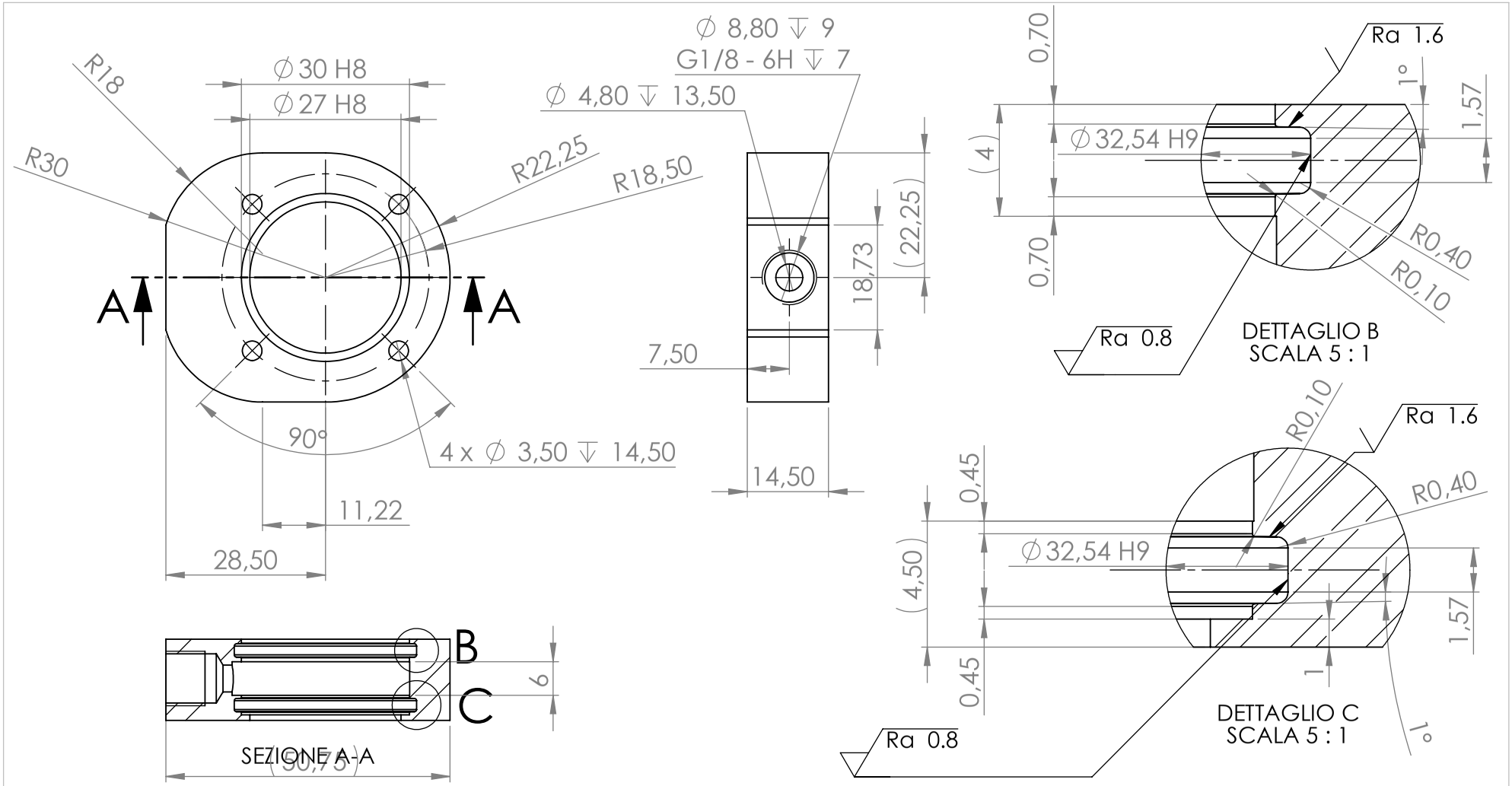

VERS	CHANGE DESCRIPTION	PROPOSED BY	DATA	SIGN.	CHECKED
3					
2					
1					

DATA 03/02/2019	DRAW BY Matteo Fagherazzi	SCALE 1:1	COMM.
Chamfers without dimension: 0.1 mm X 45° Round without dimension: R=0.2 mm		MATERIAL Stainless steel AISI 630	
GENERAL TOLERANCE: +/- 0.05 mm		QUANTITY 1	SHEET NUM: 1/3
GENERAL ROUGHNESS: 6.3 micrometers			REPLACE. DRAW:
COMMITTANT Università di Padova		RAW DIMENSIONS	TREATMENT
TITLE Closing Flange		PROGRAM Cooled Nozzle	DRAWING NUMBER flangia_chiusura

Università degli Studi di Padova

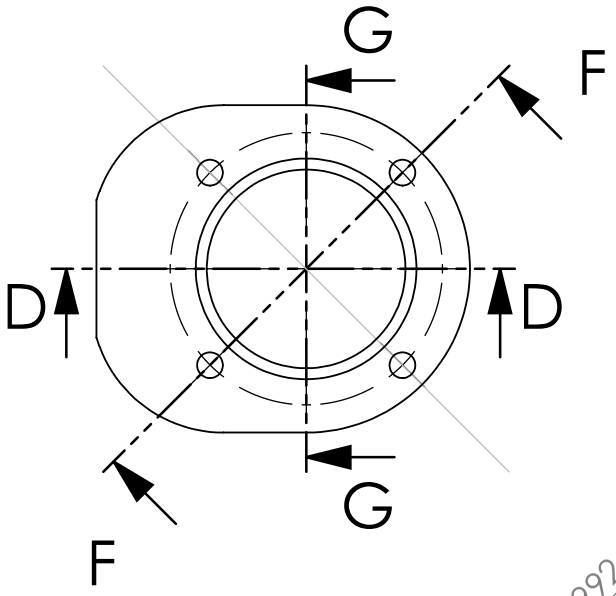

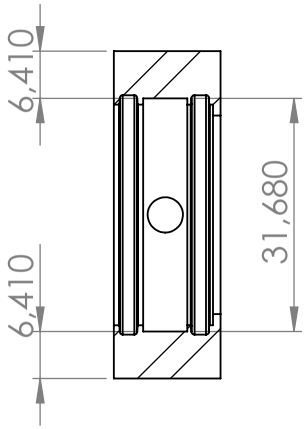

SEZIONE G-G

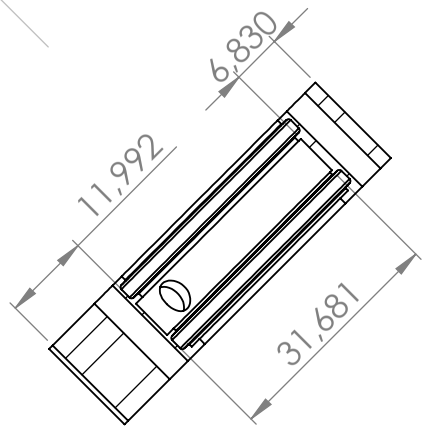

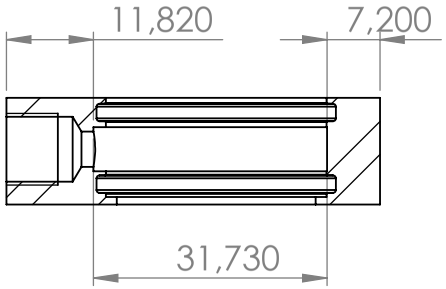

SEZIONE D-D

SEZIONE F-F

3					
2					
1					
VERS	CHANGE DESCRIPTION	PROPOSED BY	DATA	SIGN.	CHECKED

DATA 03/02/2019	DRAW BY Matteo Fagherazzi	SCALE 1:1	COMM.
Chamfers without dimension: 0.1 mm X 45° Round without dimension: R=0.2 mm		MATERIAL Stainless steel AISI 630	
GENERAL TOLERANCE: +/- 0.05 mm		QUANTITY 1	SHEET NUM: 2/3
GENERAL ROUGHNESS: 6.3 micrometers			REPLACE. DRAW:
COMMITTANT Università di Padova		RAW DIMENSIONS	TREATMENT
TITLE Closing Flange		PROGRAM Cooled Nozzle	DRAWING NUMBER flangia_chiusura

Università degli Studi di Padova

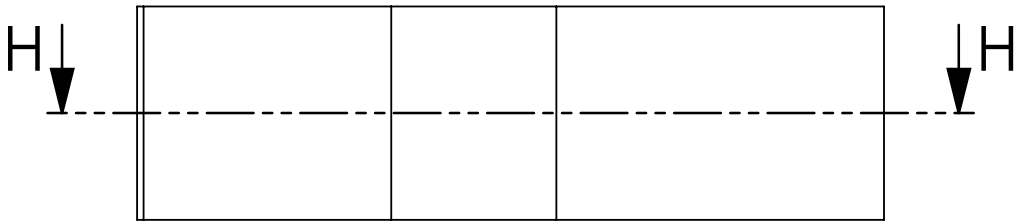

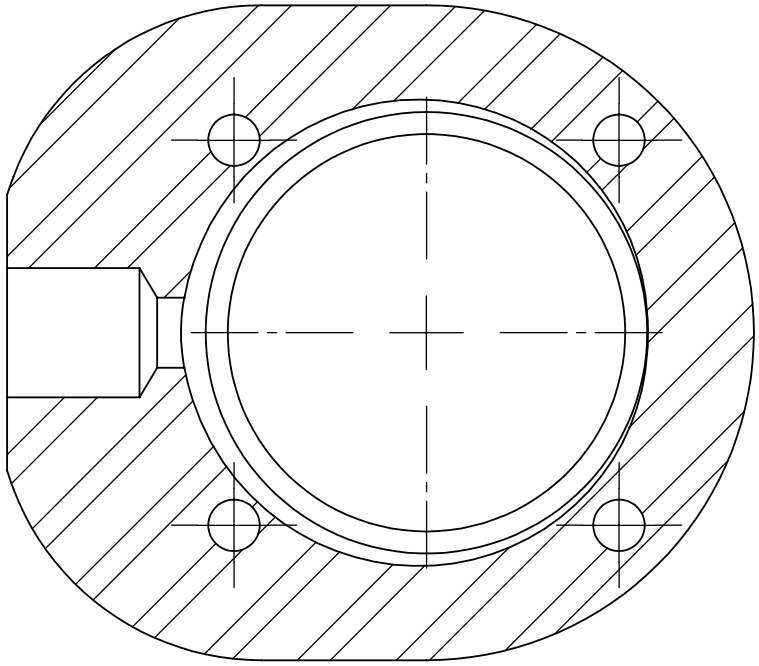

SEZIONE H-H

3					
2					
1					
VERS	CHANGE DESCRIPTION	PROPOSED BY	DATA	SIGN.	CHECKED

DATA 03/02/2019	DRAW BY Matteo Fagherazzi	SCALE 2:1	COMM.
Chamfers without dimension: 0.1 mm X 45° Round without dimension: R=0.2 mm		MATERIAL Stainless steel AISI 630	
GENERAL TOLERANCE: +/- 0.05 mm		QUANTITY 1	SHEET NUM: 3/3
GENERAL ROUGHNESS: 6.3 micrometers			REPLACE. DRAW:
COMMITTANT Università di Padova		RAW DIMENSIONS	TREATMENT
TITLE Closing Flange		PROGRAM Cooled nozzle	DRAWING NUMBER flangia_chiusura

Università degli Studi di Padova

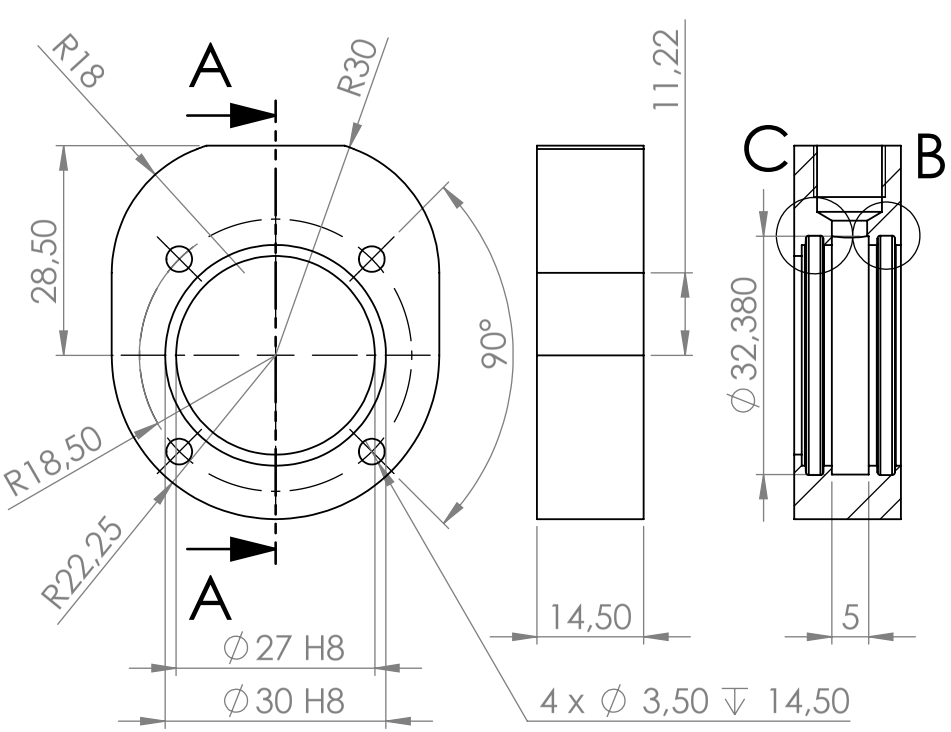

SEZIONE A-A

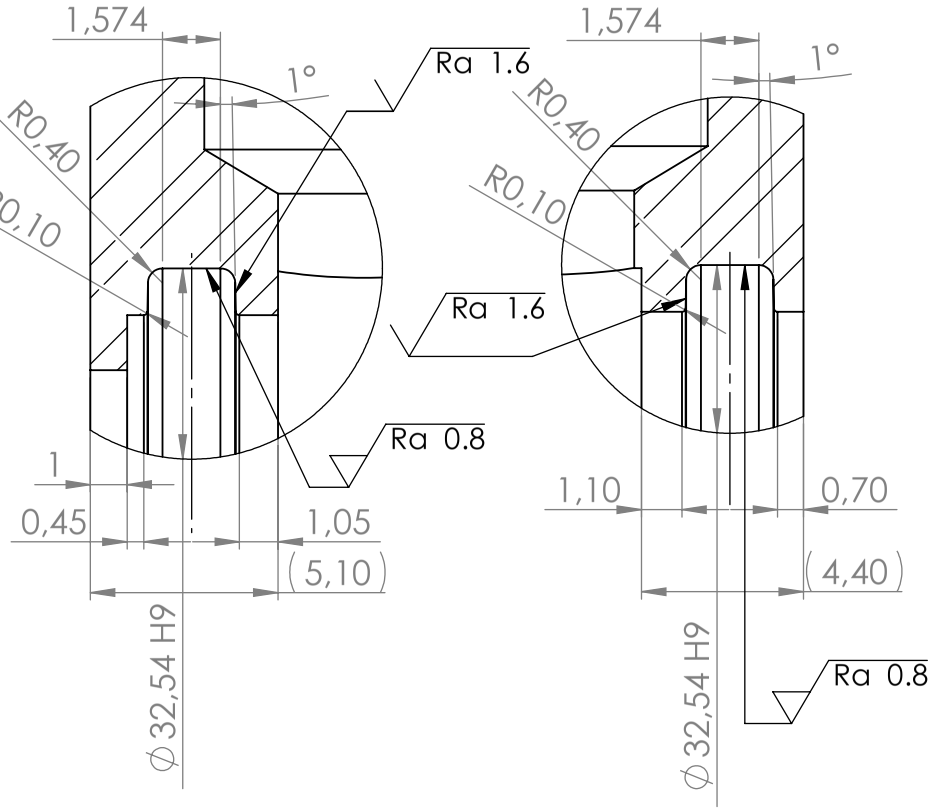

DETTAGLIO C
SCALA 5 : 1

DETTAGLIO B
SCALA 5 : 1

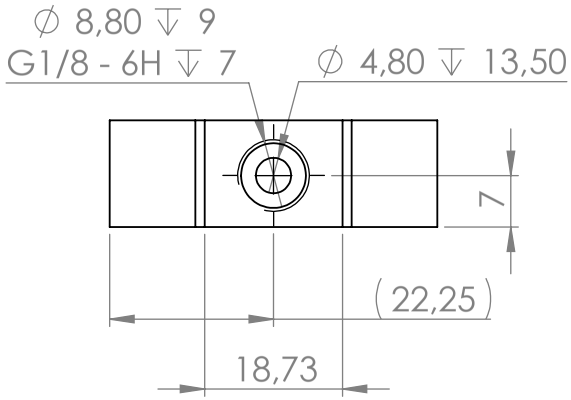

3					
2					
1					
VERS	CHANGE DESCRIPTION	PROPOSED BY	DATA	SIGN.	CHECKED

DATA 03/02/2019	DRAW BY Matteo Fagherazzi	SCALE 1:1	COMM.
Chamfers without dimension: 0.1 mm X 45° Round without dimension: R=0.2 mm		MATERIAL Stainless steel AISI 630	
GENERAL TOLERANCE: +-/ 0.05 mm		QUANTITY 1	SHEET NUM: 1/1
GENERAL ROUGHNESS: 6.3 micrometers			REPLACE. DRAW:
COMMITTANT Università di Padova		RAW DIMENSIONS	TREATMENT
TITLE Closing flange (simplified)		PROGRAM Cooled nozzle	DRAWING NUMBER flangia_chiusurab_ingrand_semp

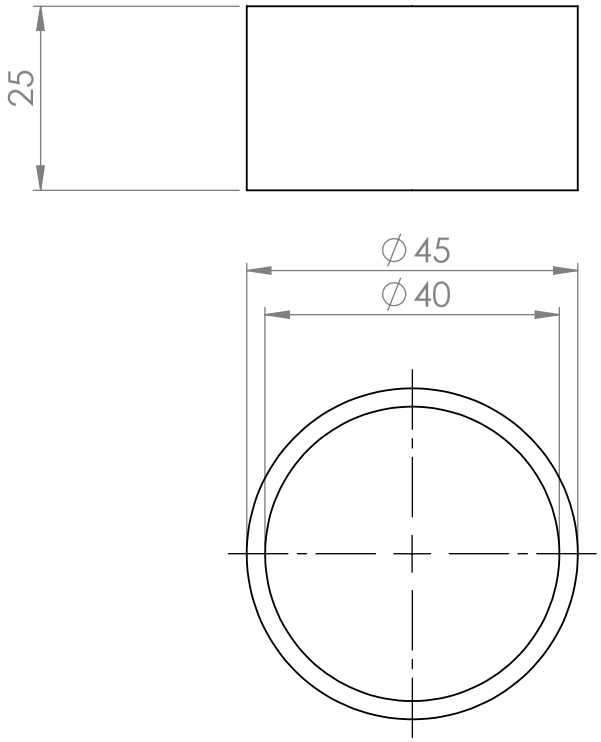

3					
2					
1					
VERS	CHANGE DESCRIPTION	PROPOSED BY	DATA	SIGN.	CHECKED

DATA 03/02/2019	DRAW BY Matteo Fagherazzi	SCALE 1:1	COMM.
Chamfers without dimension: 0.1 mm X 45° Round without dimension: R=0.2 mm		MATERIAL Stainless steel AISI 630	
GENERAL TOLERANCE: +/- 0.05 mm		QUANTITY 1	SHEET NUM: 1/1
GENERAL ROUGHNESS: 6.3 micrometers			REPLACE. DRAW:
COMMITTANT Università di Padova		RAW DIMENSIONS	TREATMENT
TITLE Cylindrical thickness		PROGRAM Cooled nozzle	DRAWING NUMBER spessore_cilindrico

Università degli Studi di Padova

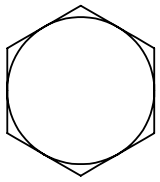

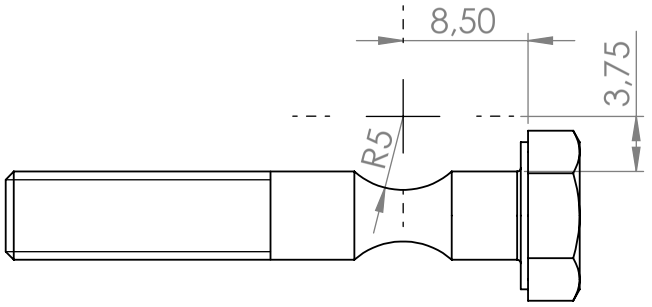

3					
2					
1					
VERS	CHANGE DESCRIPTION	PROPOSED BY	DATA	SIGN.	CHECKED

DATA 03/02/2019	DRAW BY Matteo Fagherazzi	SCALE 2:1	COMM.
Chamfers without dimension: 0.1 mm X 45° Round without dimension: R=0.2 mm		MATERIAL Steel ISO class 8.8	
GENERAL TOLERANCE: +/- 0.05 mm		QUANTITY 1	SHEET NUM: 1/1
GENERAL ROUGHNESS: 6.3 micrometers			REPLACE. DRAW:
COMMITTANT Università di Padova		RAW DIMENSIONS	TREATMENT
TITLE M6 Explosive bolt		PROGRAM Cooled nozzle	DRAWING NUMBER explosive_bolt

Università degli Studi di Padova